5-2008

REAL-TIME RAMAN SPECTROSCOPY AND WIDE-ANGLE X-RAY DIFFRACTION DURING SINGLE-LAYER AND MULTI-LAYER BLOWN FILM EXTRUSION

Giriprasath Gururajan
Clemson University, ggurura@clemson.edu

Follow this and additional works at: https://tigerprints.clemson.edu/all_dissertations

Part of the Chemical Engineering Commons

REAL-TIME RAMAN SPECTROSCOPY AND WIDE-ANGLE X-RAY
DIFFRACTION DURING SINGLE-LAYER AND MULTI-LAYER BLOWN FILM
EXTRUSION

_____

A Dissertation
Presented to
the Graduate School of
Clemson University

_____

In Partial Fulfillment
of the Requirement for the Degree
Doctor of Philosophy
Chemical Engineering

_____

by
Giriprasath Gururajan
May 2008

_____

Accepted by:
Dr. Amod A. Ogale, Committee Chair
Dr. Gary C. Lickfield
Dr. David A. Bruce
Dr. Douglas E. Hirt

ABSTRACT

Properties exhibited by blown films are controlled by the microstructure developed during their processing. Therefore, real-time measurement of microstructure during the blown film extrusion can help in better control and optimization of the process needed to obtain desired properties. The objectives of this research were (i) to conduct real-time microstructural measurements during single-layer and multi-layer blown film extrusion of polypropylene (PP) and low-density polyethylene (LDPE) using real-time Raman spectroscopy; (ii) to conduct real-time wide-angle X-ray diffraction (WAXD) during single-layer blown film extrusion of LDPE to obtain crystallinity and orientation values during the process; and (iii) to investigate the effect of blown film coextrusion on the microstructure of PP/LDPE bilayer films. The potential of real-time Raman spectroscopy as a rapid microstructure monitoring tool for better process control during blown film extrusion is demonstrated.

Real-time polarized Raman spectroscopy was conducted to measure the orientation development during blown film extrusion of low-density polyethylene (LDPE). Polarized Raman spectra were obtained at different locations along the blown film line, starting from the molten state near the die and extending up to the solidified state near nip-rolls. The *trans* C-C symmetrical stretching vibration of PE at 1130 cm^{-1} was analyzed for films possessing uniaxial symmetry. For the given peak, the principal axis of the Raman tensor is coincident with the *c*-axis of the orthorhombic crystal, and was used to obtain second ($\langle P_2(\cos\theta)\rangle$) and fourth ($\langle P_4(\cos\theta)\rangle$) moments of the

orientation distribution function. The orientation parameters (P_2, P_4) were found to increase along the axial distance in the film line even past the frost-line height (FLH). The P_2 values also showed an increasing trend with crystalline evolution during extrusion consistent with past observations that molecular orientation takes place even after the blown film diameter is locked into place. It was also found that the integral ratio (I_{1132}/I_{1064}), obtained from a single, ZZ-backscattered mode, can provide a reasonable estimate of molecular orientation.

Although Raman spectroscopy is a convenient technique, it is not a primary measurement technique to obtain crystallinity and orientation in fibers or films. So for the first time, a real-time wide-angle X-ray diffraction (WAXD) technique was attempted during blown film extrusion. WAXD patterns were obtained at different axial positions in the film line starting from a location near the die up to the nip-roller. The composite X-ray diffraction patterns from the bubble were analyzed and quantified for crystallinity values. From the evolution of (110) and (200) peaks in the WAXD pattern, it was inferred that the crystallization process started near the frost-line height (FLH) and showed a steep increase at lower axial distance near the freeze line and then a gradual increase at higher axial distance in the film line. The differences in the profiles for crystallinity were also evident with changing processing conditions. The crystallinity results obtained using WAXD were found to be consistent with those from simultaneous real-time Raman spectroscopic measurements. Thus, for the first time, real-time WAXD technique was successfully used for measurement of microstructure during the single-layer blown film extrusion of low density polyethylene (LDPE).

Multi-layer blown films are of significant industrial importance to make packaging films with desirable properties through combination of two or more polymers. Therefore, real-time Raman measurements were extended from single-layer blown film extrusion to multi-layer blown film extrusion. Online spectroscopic measurements were carried out to estimate crystalline growth of the individual components of a bicomponent low-density polyethylene (LDPE) and polypropylene (PP) film (LDPE/PP). The 1296–1305 cm^{-1} band, observed predominantly for PE, was only slightly masked by the contribution from the PP layer. In contrast, the 809–841 cm^{-1} band was unique for PP and unaffected by the presence of the PE layer and 1418 cm^{-1} band was unique for PE. These distinct peaks enabled successful deconvolution of the superimposed spectra to enable crystallinity measurements during coextrusion of LDPE/PP films. Such real-time results have not been reported earlier in the literature for multi-layer films.

Finally, real-time Raman spectroscopy results were used to develop an understanding of processing-microstructure relationship for the blown film process. For bilayer films (PP/LDPE), the onset crystallization-time difference for PP and LDPE components was found to be an important parameter, which controls the orientation and morphology of the coextruded films. Although overall molecular orientation within PP and LDPE multiple layers was not affected, single-layer LDPE films displayed some row-nucleation, but not the LDPE layer in coextruded films. Also, there was a slight decrease of crystalline a-axis orientation for coextruded LDPE layer as compared to that for single-layer LDPE films. Thus, as one component of experimental research being conducted at the Center for Advanced Engineering Fibers and Films (CAEFF), this study

was successful in generating real-time experimental results during the film formation that

are critical for validating modeling results being generated in companion studies.

DEDICATION

I dedicate this work to my beloved parents, Mrs. Rakma Gururajan and Mr. Gururajan.

ACKNOWLEDGEMENTS

TABLE OF CONTENTS

LIST OF TABLES

LIST OF FIGURES

List of Figures (Continued)

List of Figures (Continued)

List of Figures (Continued)

List of Figures (Continued)

List of Figures (Continued)

List of Figures (Continued)

CHAPTER ONE

INTRODUCTION

1.1. Raman Spectroscopy

When an incident laser beam encounters molecules in a target film sample, the predominant mode of scattering is elastic scattering or Rayleigh scattering, where the molecule returns to the original ground state from its excited state and the photon is "reemitted" at the incident frequency. It is also possible for the incident photons to interact with the molecules in such a way that energy is either gained or lost so that the scattered photons are shifted in frequency. This inelastic scattering is called Raman scattering, and is illustrated in **Figure 1.1**, where a photon raises the energy of the molecule from the ground state to a non-stationary higher energy level. The energy difference between the incident and scattered photons is shown by the arrows of different lengths. Most molecules return to the initial ground state by emitting a photon of same energy.

However, nominally one in ten million photons returns to a different vibrational energy level that may be higher or lower than that of the initial ground state. Stokes Raman scattering occurs if the excited molecules return to a higher vibrational level and emits a photon of less energy (long wavelength). Anti-stokes Raman scattering occurs if the molecules relax to a lower energy state than the ground state resulting in emission of

high energy photon (short wavelength). The relative intensity of Stokes and anti-Stokes scattered light is proportional to the ratio of the populations in the ground and excited states.
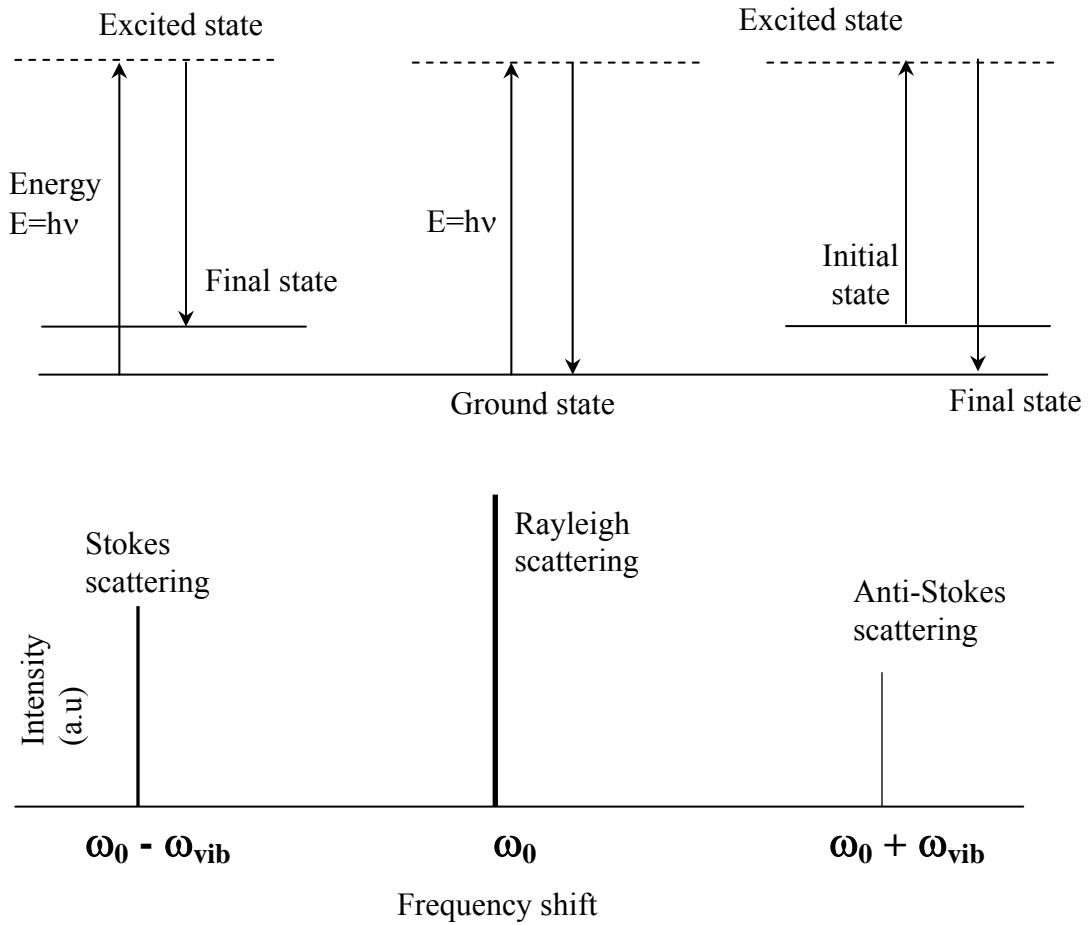
Figure 1.1. Schematic showing the Raman scattering and Rayleigh scattering

The energy difference between the initial and final vibrational levels is the Raman shift represented in wave numbers (cm^{-1}) and is given by the difference [ν= 1/ λ incident - 1/ λ scattered], where λ incident is the wavelength of laser source and λ scattered is the

wavelength of Raman scattered photons. At equilibrium, the number of molecules in the excited state is always lower than the number of molecules in the ground state. Therefore, the intensity of Stokes scattering will be higher than the anti-Stokes scattering.

Since the discovery of Raman scattering effect in the late 1920s, many research articles [1-14], review papers [15-17], books [18-21] and industrial patents [22-24] have been published on the application of Raman spectroscopy for polymers. Typically, the technique is used to determine the polymer type and content [1-3], polymerization reaction kinetics [4, 5], amount of pigment additives [6, 7], amount of degradation [8, 9], change in the morphology of the polymer such as crystallinity and molecular orientation [10-14], etc. A vast majority of research on Raman spectroscopy of polymers [1, 6, 7, 10-14] has involved post-mortem analysis of the polymer product.

The introduction of laser excitation sources in the 1960s and charge-coupled detection devices in the 1990s enabled development of sophisticated Raman instrumentation. This includes fiber-optics coupling that not only increased the signal-to-noise ratio but also reduced the fluorescence effect. Further, data collection times have been reduced to durations as little as a few seconds. Consequently, the technique is proving to be a powerful real-time polymer process monitoring tool.

Conventional manufacturing uses off-line measurements on the processed polymer to empirically modify the process to obtain the desired properties. This trial-and-error procedure is time-consuming and expensive. Therefore, there is a growing demand to characterize materials during its production by using real-time analytical tools.

Techniques such as small-angle light scattering (SALS) [25], birefringence [26, 27], wide-angle X-ray diffraction (WAXD) [28-30] and infrared dichroism (IR) [31] have been applied to polymers as a process monitoring tool in a laboratory environment. Bullwinkel et al. [25] used simultaneous online small angle light scattering (SALS) and infrared temperature measurements to study the microstructure evolution during LLDPE blown film extrusion. They related the change in average scattered intensity of the light to the crystallization process. Nagasawa et al. [26] reported the first online measurements of orientation development during blown film extrusion using birefringence. Additional studies were conducted by Ghaneh-Fard et al. [27] during the film blowing of a linear low-density polyethylene. Real-time microstructural measurement during film casting of isotactic polypropylene is reported by Lamberti et al. [31] using FTIR.

These techniques cited above, however, are not conducive for rapid real-time measurements in industrial environments that involve elevated temperatures, high pressure, and humidity. For instance, SALS and birefringence techniques are very sensitive to the thickness of the polymeric sample, whereas WAXD requires long exposure times, safety precautions, and expensive instrumentation.

The end-use properties of a polymer product depend on the molecular architecture of the polymer and the history of its formation. The molecular architecture is determined by factors such as molecular weight distribution (MWD) and copolymer composition, whereas properties are controlled during extrusion and fabrication by factors such as thermal and strain-rate history. Thus, Raman spectroscopy offers distinct advantages over SALS, WAXD, birefringence, and other spectroscopy (FTIR, NMR) because it is not

affected by moisture in the environment and is very amenable to fiber-optic-coupling using low-cost silica fibers. This feature allows one to analyze remotely situated samples and measurements in difficult environments without need for special sample cells in the process line. The technique requires virtually no sample preparation and is independent of sample size and shape. The implementation of real-time Raman spectroscopy to obtain information about the polymer has been adopted in various petrochemical plants [22] and polymer processing industries [23, 24] to enhance the control of production parameters.

Although the potential of Raman spectroscopy for characterizing polymers has been recognized for a number of years, systematic studies addressing the use of the technique for real-time microstructure development are largely unavailable in the literature. Recently, Paradkar et al. [32] utilized real-time Raman spectroscopy for crystallinity measurements at different points along the fiber spinning line. Their study demonstrated the feasibility of using a Raman spectroscopic technique to monitor the development of crystallinity in melt spun high density polyethylene (HDPE) fibers. The real-time Raman spectra from a single HDPE fiber, obtained as a function of distance from the spinneret, were used to study the effect of process parameters including throughput, quench rate and take-up speed during fiber spinning. In a companion study, real-time Raman spectroscopy measurements during single-layer blown film extrusion process have been conducted [33, 34].

Like any vibrational spectroscopic techniques, Raman spectroscopy is not a primary measurement technique for microstructure. The integral intensities from Raman

spectra are calibrated using primary measurement techniques such as differential scanning calorimetry (DSC), density measurements, or X-ray diffraction [10].

1.2. X-ray diffraction

X-rays are high energy electromagnetic radiation with photon energies in the range of 0.1 keV to 100 keV. Since the wavelength of X-rays is of the same order of the size of atoms, they are ideally suited for probing the structural arrangement of molecules in polymers. An X-ray beam is produced using an X-ray tube or synchrotron radiation. X-rays formed from X-ray tubes are of low energy (10 keV), while X-rays produced using synchrotron source are very powerful requiring sophisticated instrumentation. The energy of an X-ray photon is given by $E = hc/\lambda$, where h is Planck's constant, c the speed of light and λ is the wavelength of the X-ray beam (1.54 Å for CuKα source).

When X-ray photons interact with electrons in atoms of the materials, some photons will be scattered with the same energy as the incident X-ray photon (elastic scattering) and a few photons will have less energy than the incident X-ray photon (inelastic scattering) due to absorbance by the material. The elastic scattering is called the Thompson scattering, while inelastic scattering is called Compton scattering.

The scattering of an X-ray beam from a sample is based on satisfaction of Bragg's law. An incident X-ray beam interacts with the atoms that are arranged in a lattice planes (**Figure 1.2a**) and are scattered inphase or out-of-phase with the incident beam to form constructive and destructive interference, respectively. For a given set of lattice planes with an inter-planar distance of d, the diffraction occurs due to in-phase and constructive interference is given by

$$2d \sin \theta = n \lambda$$

where λ is the wavelength of the incident X-ray beam, n is an integer and θ is the scattering angle. **Figure 1.2b** displays the transmittance of X-ray beam through the sample. The scattered X-ray beam is captured using a photographic plate or an intensity detector.

X-ray diffraction is one of the standard techniques to analyze the crystalline structure of polymers. There are numerous research publications [35-38] on the application of X-ray diffraction technique to study the amorphous and semi-crystalline polymers and its blends. The technique is carried out as wide-angle X-ray diffraction (WAXD) or small-angle X-ray diffraction (SAXD) on fibers and films. To investigate the fraction of crystallinity in the material, orientational order and interplanar spacing (d) affected due to processing and blending with other materials, wide-angle X-ray scattering is used. Microstructural parameters such as long period (L) and crystalline thickness (L_c) are obtained using SAXS to detect any long range order (> 50 Å).

Incident X-ray   Scattered X-ray

Lattice plane   θ   θ

A   θ   C   d

B

X-ray detector

Transmitted Beam

Sample

2θ

Incident X-ray
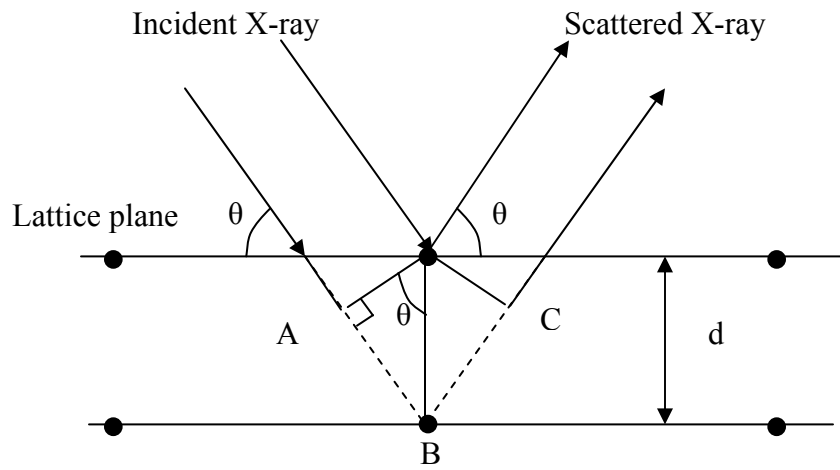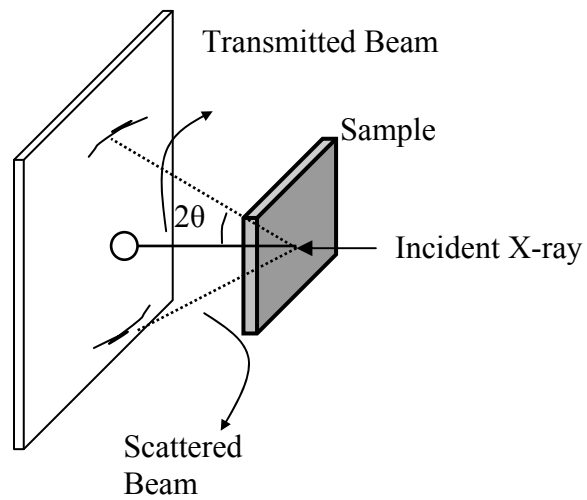
Scattered
Beam

Figure 1.2 a) X-ray scattering obeying Bragg's law, b) X-ray diffraction by

transmittance of X-ray beam through the sample.

1.3. Blown Film Extrusion

Blown film extrusion is one of the major processes used to produce films [39], ranging from simple mono-layer films for bags and membranes to very complex multi-layer structures used in specialized applications such as food and medical packaging. A typical blown film line is as shown in **Figure 1.3.** It consists of three units: an extruder, a die, and a take-up unit. The extruder does the job of melting the polymer and pumping it through a die. The extruder screw is driven by a motor whose speed can be adjusted to obtain the desired flow rate through the die. The molten extrudate exiting the annular die is blown as a bubble by expanding in the transverse direction (TD) by air passing through the center of the die and also pulled longitudinally in the machine direction (MD) by rollers. The bubble so formed is simultaneously cooled using quench-air that circulates along the periphery of the bubble. The solidified film is then collapsed and flattened by nip rolls and wound using the rollers in the take-up unit.

Besides the melt temperature, there are three important processing parameters that can be controlled during the blown film extrusion. The blow-up ratio (BUR) is the ratio of the final bubble diameter to the die diameter, and ranges from 1.5 to 4. This transverse expansion of the bubble is primarily controlled by the inflation air pressure on the volume of the bubble. The quench air around the bubble cools the molten bubble and locks further expansion of the bubble after a certain distance above the die, which is defined as the frost-line height (FLH).   The rate at which the bubble is stretched in the longitudinal
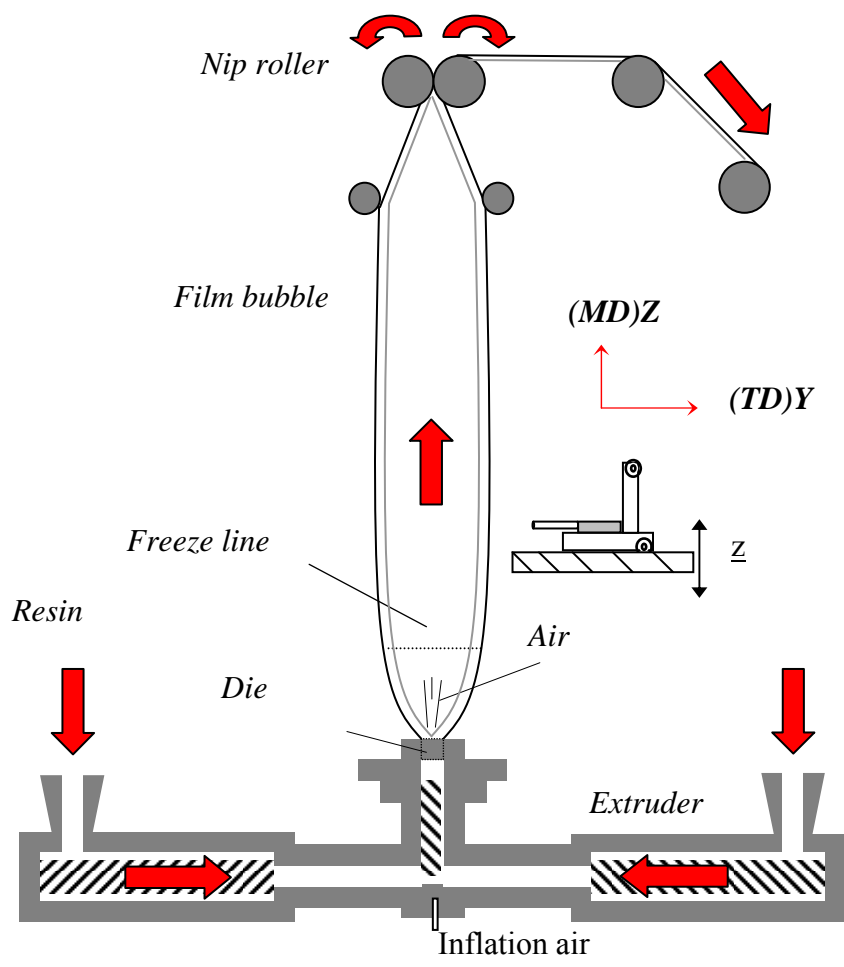
Figure 1.3 A schematic of a bilayer blown film extrusion process

(machine) direction is defined by the take-up ratio (TUR), i.e., the ratio of the velocity of the take-up roller (V_f) to the velocity of the extrudate at the exit of the die (V_0).

Figure 1.4 illustrates the influence of various factors on properties of single-layer blown films. There are other factors such as number of layers, adhesion between layers, and viscosity ratio that influence if two or more polymers are coextruded. Since the microstructure of the film plays a dominant role in influencing the mechanical, thermal and physical properties of the films, it is important to study the microstructure development during the process and relate with process and the property of blown film. Also, the mission of the Center for Advanced Engineering Fibers and Films (CAEFF), the mission is to generate experimental data during film formation in order to integrate with the molecular and continuum level modeling efforts of the process.

Raw Material Properties	Processing Conditions	Equipment
Molecular Weight MW distribution Density Branching Additives	Single/Coextrusion Melt Temp. FLH BUR TUR	Die Size Die Gap Air Ring Internal Bubble -Cooling

Crystallinity & Orientation

Impact Strength Shrinkage Barrier Properties	Optics Modulus Sealability	Tear Strength Tensile Strength Surface Tension

Figure 1.4 A flow-diagram of factors controlling blown film properties

1.3.1. Single-layer Blown Film Extrusion

Single-layer blown film extrusion involves continuous extrusion of a pure or blended resin through an annular die to form films with thicknesses typically in the range of 25 to 250 μm. **Figure 1.5** displays a schematic of a single-layer blown film die. The annular die has a spiral-head mandrel in order to obtain good melt distribution and uniform pressure drop so that there is minimum thickness variation in the film. Historically, it was the first continuous process used to make polyethylene films [40]. It is

still a predominant process to make films involving high commodity resins. Thermoplastic resins such as polyethylene (LLDPE, LDPE, and HDPE) and polypropylene (PP) are either extruded in its virgin state or blended with other resins to form films using this process. Since single-layer blown films represent the largest market for films, with a worldwide consumption of 30 million tons a year [40], a significant amount of research is still being carried out on this process both from experimental [41-45] and modeling [46-51] perspectives.
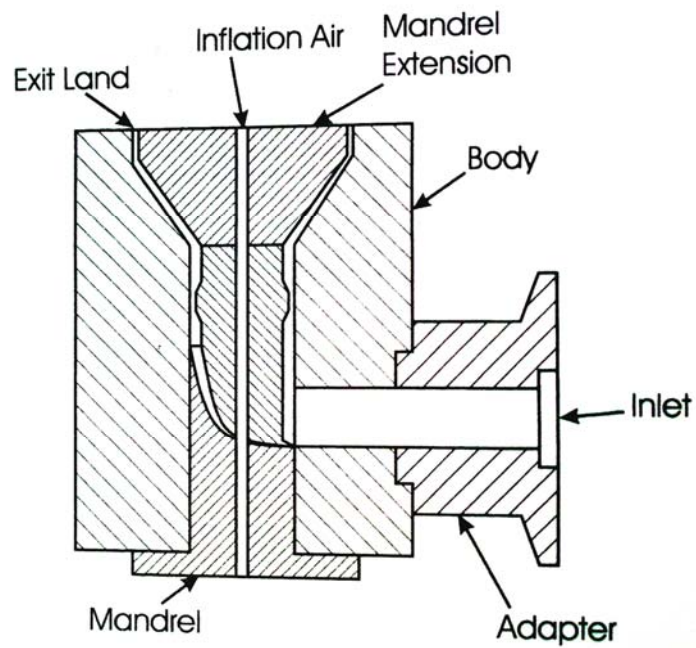
Figure 1.5 Single-layer blown film die [39] (Reproduced with permission from Hanser Publishers)

The dynamics of film blowing process are more complex than those for the fiber spinning operation as it involves biaxial stretching of the films. Bubble kinematics and

temperature are often measured for correlation to mechanical properties of the final film [34, 52]. The velocity and bubble diameter profiles are typically obtained using video tracer and image analysis techniques and are used to solve the momentum equations [52] to obtain strain-rates in the bubble. The stress experienced by the bubble during film blowing is proportional to the strain-rates.

The deformation rate equations were first derived by Pearson and Petrie [49]. They developed a simple isothermal viscous blown film model based on the assumption of a Newtonian melt during the process. The deformation rate tensor for the bubble is written as:

$$\|d\| = \begin{Vmatrix} d_{11} & 0 & 0 \\ 0 & d_{22} & 0 \\ 0 & 0 & d_{33} \end{Vmatrix}$$

where d_{11}, d_{22} and d_{33} are the strain rate or deformation rate in the machine direction (MD), transverse direction (TD) and the normal direction (ND) and are expressed as

$$d_{22} = \frac{QCos\theta}{2\pi rh}\left[\frac{1}{r}\frac{dr}{dz}\right] = 2\frac{v_z}{r}\left(\frac{dr}{dz}\right)$$

$$d_{11} = \frac{QCos\theta}{2\pi rh}\left[\frac{1}{h}\frac{dh}{dz}\right] = \frac{2}{h}\left(\frac{dh}{dz}\right)v_z$$

$$d_{33} = -\frac{QCos\theta}{2\pi rh}\left[\frac{1}{h}\frac{dh}{dz} + \frac{1}{r}\frac{dr}{dz}\right] = 2\frac{dv_z}{dz}$$

where

v= the velocity of the bubble,

z= the axial distance,

r= the variable radius of the bubble,

θ= the variable angle made by the bubble with the z-axis,

h= the thickness variation of the bubble.

Q=the volumetric flow from the extruder.

At CAEFF, Srinivas et al. [34, 53, 54] conducted detailed online kinematics measurements during single-layer blown film extrusion of polyolefins. **Figure 1.6** presents the variation of strain rates with change in BUR from 0.4 to 2.0, while the take-up ratio is kept constant at 3.5. The strain-rates along the TD (e_2) shift from negative to positive values (biaxial distribution), while the strain-rates along the machine direction (e_1) does not show significant variation. As compared to a BUR of 0.4, the larger bubble diameters at BURs of 1.5 and 2.0 result in thinner films, causing an increase in stresses along the transverse direction. The wide variation possible in processing conditions can lead to variations in microstructure of the film, and thence to its properties.
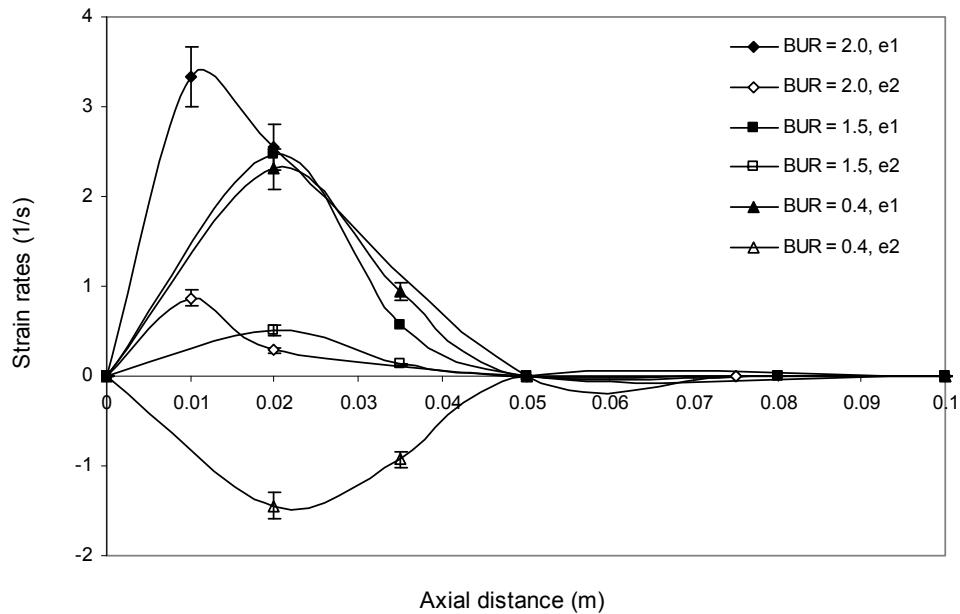
Figure 1.6 Machine direction (e_1) and transverse direction strain rates (e_2) in the bubble for BURs of 0.4, 1.5 and 2.0 and a TUR of 3.5 [34] (Reproduced with permission from Dr. Cherukupalli, Clemson University, 2005)

1.3.2. Multi-layer Blown Film Extrusion

Multi-layer blown film coextrusion involves simultaneous extrusion of several layers or resins through a single block of concentric annular rings to produce a single integral film. This is an economical way of continuously processing two or more polymers to obtain multi-functional packaging films that would otherwise be unattainable using a single polymer [55]. **Figure 1.7** displays the drawing of a multi-layer blown film die. Molten polymers from the extruders are side-fed to the annular spiral mandrel die to

form films of A/B/A structure. Five-layer blown film extrusion is common in industry, but as many as 11 layers have been coextruded [56]. Typically blown film coextrusion is carried out to form multifunctional films and high-performance barrier films.

Table 1.1 lists commercially important polymers used in coextruded films and their applications. The intrinsic properties of the component polymers determine the mechanical and barrier properties of the composite films. However, interactions between the individual layers, which are dependent upon miscibility of the polymer and processing conditions, are also important. Although single-layer blown film extrusion is still a dominant process to make packaging films, more film converters are opting for multi-layer blown films (7 million tons per annum) [40] in order to meet growing demand for multifunctionality for food, electronic and agricultural packaging applications. Therefore, further research needs to be carried out to understand the multi-layer blown film process and also to investigate the effect of coextruding two different polymers, so that process/product improvement can be achieved.
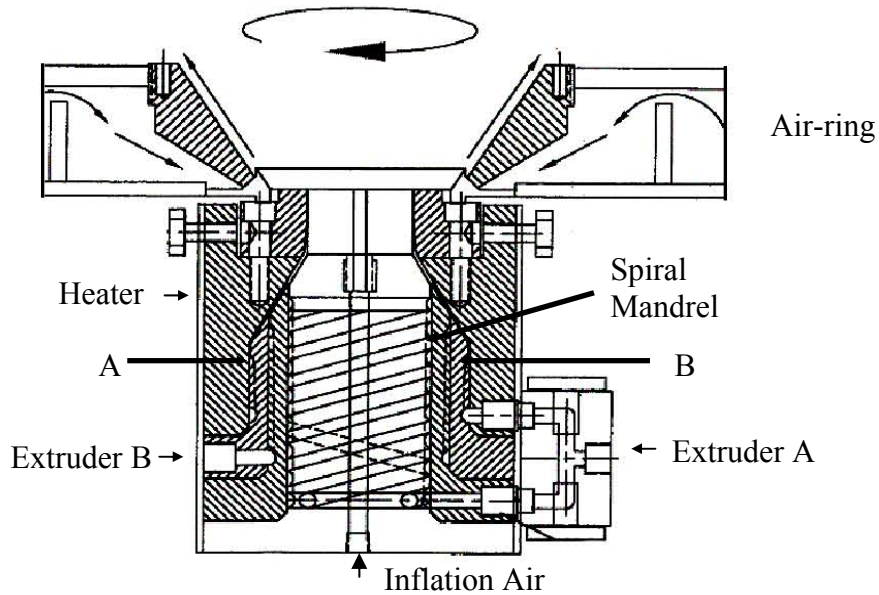
Figure 1.7 Multi-layer blown film die to form three layer (A/B/A) films

(Reproduced with permission from Wayne Machine & Die Company, NJ)

FUNCTIONALITY	POLYMERS	APPLICATIONS
OXYGEN BARRIER	PP, EVOH, PA, LCP	Food packaging for long shelf life
RIGIDITY AND ELASTICITY	HDPE, PP, LDPE	Stretch films, industrial bags
HEAT SEALABILITY	EVA, IONOMER, LDPE	Shrink wrap films, medical packaging films

Table 1.1. Multi-layer blown films and their functionality for various

applications [40].

1.3.3. Cooling Air System During Blown Film Extrusion

The air cooling system is an important aspect of blown film extrusion process. Air from a blower is directed through the air ring mounted on the top of the die to uniformly cool the periphery of the molten bubble exiting the die. The aerodynamics of cooling operation not only affect the heat transfer from the bubble [57, 58], but also influence the stability of the bubble, process-throughput, thickness uniformity in the bubble, and therefore the physical and mechanical properties of the processed films.

Two types of air rings are typically used in commercial processes: single-lip and dual-lip air ring as shown in **Figure 1.8a and b,** respectively. For single-lip air ring, as shown in **Figure 1.8a**, high flow rate of air through a single orifice causes turbulence close to the bubble surface which results in an unstable bubble. On the other hand, for dual-lip air ring system (**Figure 1.8b**), there are two orifices that control the flow of air to the bubble. First, the air flow is partially directed through the lower orifice to generate a laminar flow, while large volume of the air flows through the upper lip without creating turbulence.

Although most of the lab-scale blown film systems use single orifice air ring, dual-lip air rings are important in manufacturing processes because they offer both stability and high production rates. It is reported [57] that in the case of blown film extrusion with single-lip air ring arrangement, the bubble is quenched immediately after the polymer melt exists the die. This causes lower deformation and stretching of the molecular chains in the bubble from single-lip as compared to dual-lip air ring
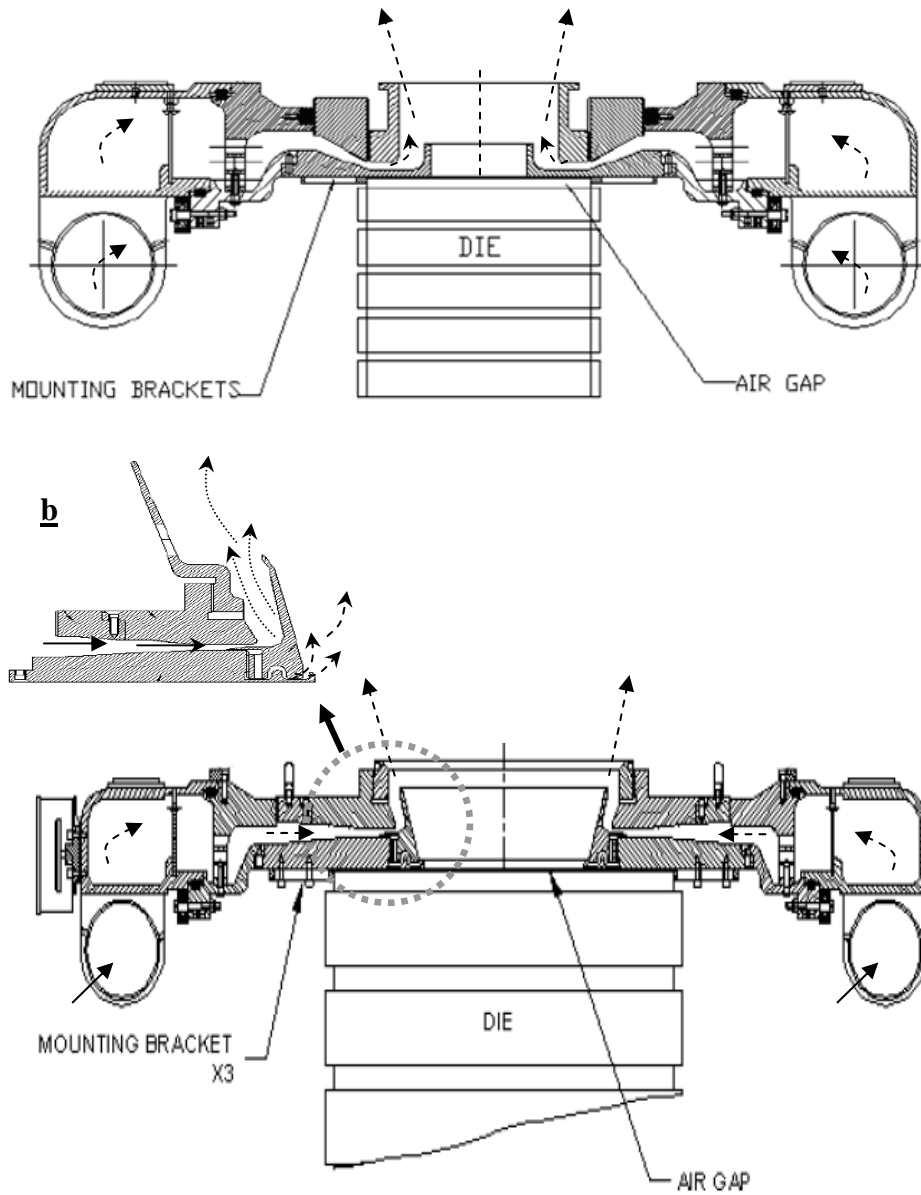
Figure 1.8 Schematic diagram of air-cooling system in blown film line a) single-lip air ring b) dual-lip air ring (inset shows the air-flow through orifice in dual lip air ring) (Reproduced with permission from Future Designs Inc.)

arrangement, where most of the cooling occurs after significant stretching of the molecular chains has taken place in the region from the die to the upper lip. These differences in heat-transfer in the two air-ring arrangements influence the final film properties and so is an important aspect that needs to be investigated.

An infrared pyrometer, a non-contact sensor, is typically used for measurement of surface temperature of a material during fabrication. The selection of the temperature sensor is based on the infrared absorption band of the polymer used in the process. For polymers such as polyethylene, polypropylene, vinyls and nylons, transmittance values approaches zero (at high thickness) near 3.43 μm and so they show high emissivity of $\approx$ 0.96. For polyester (PET) and fluorocarbon, 7.92 μm wavelength should be used. Since the spectral filter allows only certain wavelength range suitable for the polymer of interest, the measurement is not affected by moisture or other influences in the environment.

Most of the studies [57, 58] reported on dual-lip air ring system for blown film extrusion have dealt with the aerodynamics of cooling rather than the changes taking place in the bubble. The process dynamics and the crystallinity evolution in film blowing operation using dual-lip air ring arrangement need to be explored.

1.4. Polymer Structure

Semi-crystalline polymers are modeled as having two-phases: a crystalline phase and an amorphous phase. **Figure 1.9** shows the schematic of semi-crystalline structure [59] in polymers where the crystalline regions consist of chains with appropriate conformations arranged in a crystal lattice, while the amorphous regions consist of a group of random chains with thermodynamically unfavorable conformations and defects. A stack of regularly folded polymeric chains form lamellae. The crystalline and amorphous region is connected by a group of tie molecules and is called the interlamellar region. Although the amount of crystallinity in a polymer is primarily determined by its chemical structure that allows the chains to arrange itself in a crystal lattice, processing conditions also play an important role in determining the mass fraction of the crystals, size, size distribution and the orientation of the chains (crystalline and amorphous).
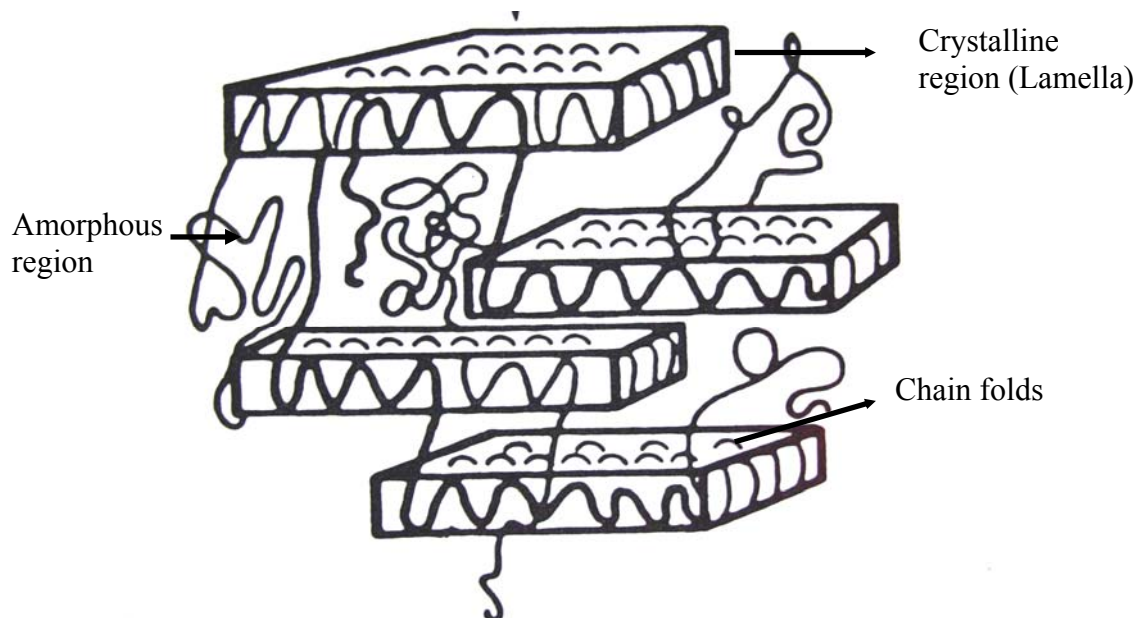
Figure 1.9 Schematic representation of semi-crystalline structure [59]
(Reproduced with permission from Springer Publishers Inc.)

When crystallized from the melt, lamellae are arranged in different forms that represent the bulk morphology of the material. Under quiescent condition (without flow and pressure), spherullitic structures are formed as shown in **Figure 1.10**, where the lamellae grow radially in all directions from a central nucleus. The size of the spherullites is typically in the range of 10-100 μm in diameter.

On the other hand, if the polymeric melt is subjected to elongational flow or shear, the crystals are arranged to form shish-kebab or row-nucleated structure. Here the extended high-molecular-weight chains or fibrils act as nuclei and are arranged parallel to the stretching direction. Secondary nucleation occurs on the surface of these rows of fibrils forming folded-chain lamellar crystals that are perpendicular to the stretching direction. **Figure 1.11** shows the schematic representation of row-nucleated structure characterized by rows of extended chain fibrils from which lamella grow perpendicularly. This type of morphology is an important aspect of stress-induced crystallization [60-62] during blown film process.
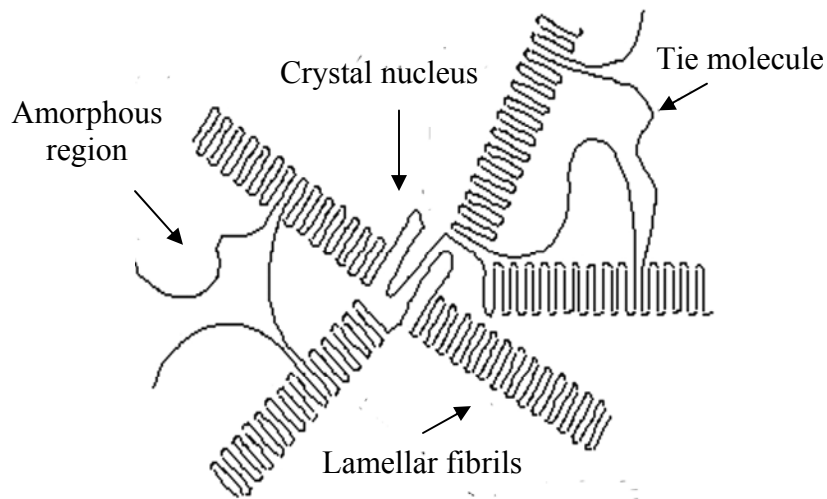
Figure 1.10 Schematic diagram of spherulitic structure of polymer [62]

23
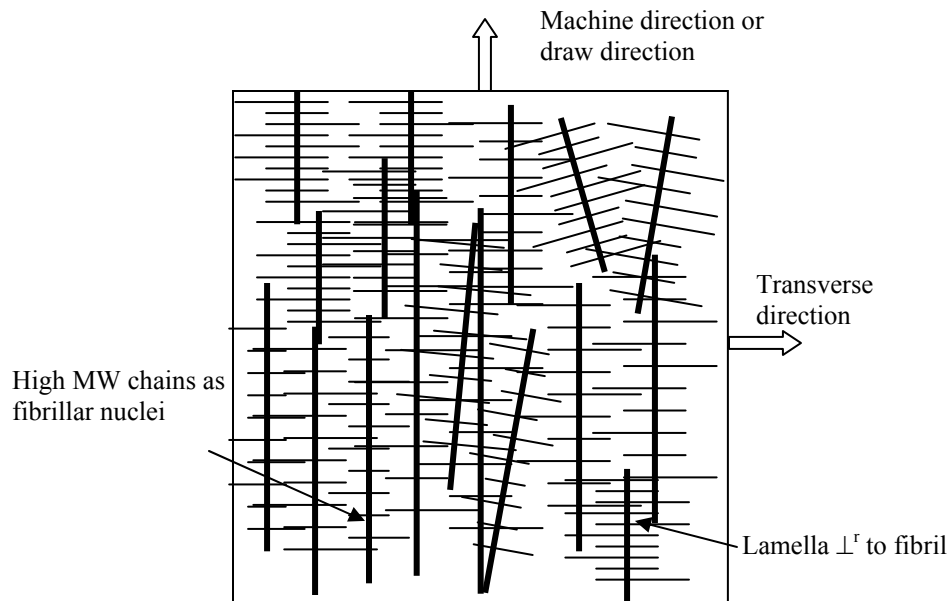
Figure 1.11 Schematic diagram of row-nucleated structure of polymer

1.4.1. Polypropylene

Polypropylene is produced from propylene monomer (CH_2=CH-CH_3) by Ziegler-Natta or metallocene catalysis polymerization. Depending on the arrangement of the methyl groups of propylene repeat unit, three different tacticities (atactic, isotactic and syndiotactic) are possible. Of the three types, isotactic polypropylene, where the methyl groups are in the same side of the chains is produced in high volume.

Polypropylene exhibits polymorphism with monoclinic (α-form), hexagonal (β-form), orthorhombic (γ-form) and a mesomorphic form (smectic). The α-form shown in

Figure 1.12 is the most stable form where the unit cell has dimensions of a=0.665 nm, b=2.096 nm, c=0.650 nm and angle β = 99.3°. The unit cell has four chains in the $3C_1$ helical conformation with c-axis corresponding to the chain axis. The a and b axes are the growing directions of the lamella. The β and γ type of crystal structure are formed only under specific conditions [63-65] i.e., high shear or high pressure or in the presence of β-nucleating agents.
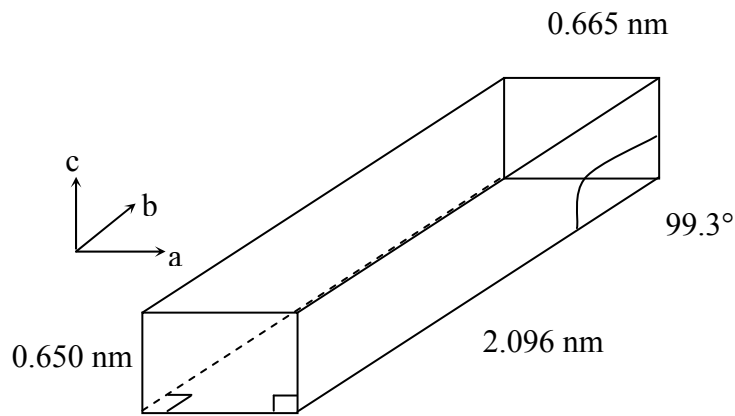
Figure 1.12 The monoclinic unit cell (α) of polypropylene (PP)

Two different arrangements of crystalline regions are possible in PP depending on the processing condition used. One is the spherullitic morphology (**Figure 1.10**) formed under quiescent crystallization condition or when the melt was subjected to very low strain and slow cooling so that relaxation of chains occurs. Second is the shish-kebab morphology [66] that is formed when the melt is subjected to shear or elongational forces. The shish-kebab morphology shown in **Figure 1.13** consists of a group of

extended chain fibrils called "the shish" and lamella called "the kebabs" growing perpendicular to the shish.

The crystallinity of polypropylene is typically in mid-range compared to LDPE and HDPE at 50-60 wt %, while its density is typically in the range of 0.90-0.91 g/cc. The melting point of polypropylene is relatively higher than many other polyolefins, at $\approx 160°C$. Thus, it offers excellent strength, heat resistance and processability and is being used in diverse applications such as films, auto-parts, and textiles.
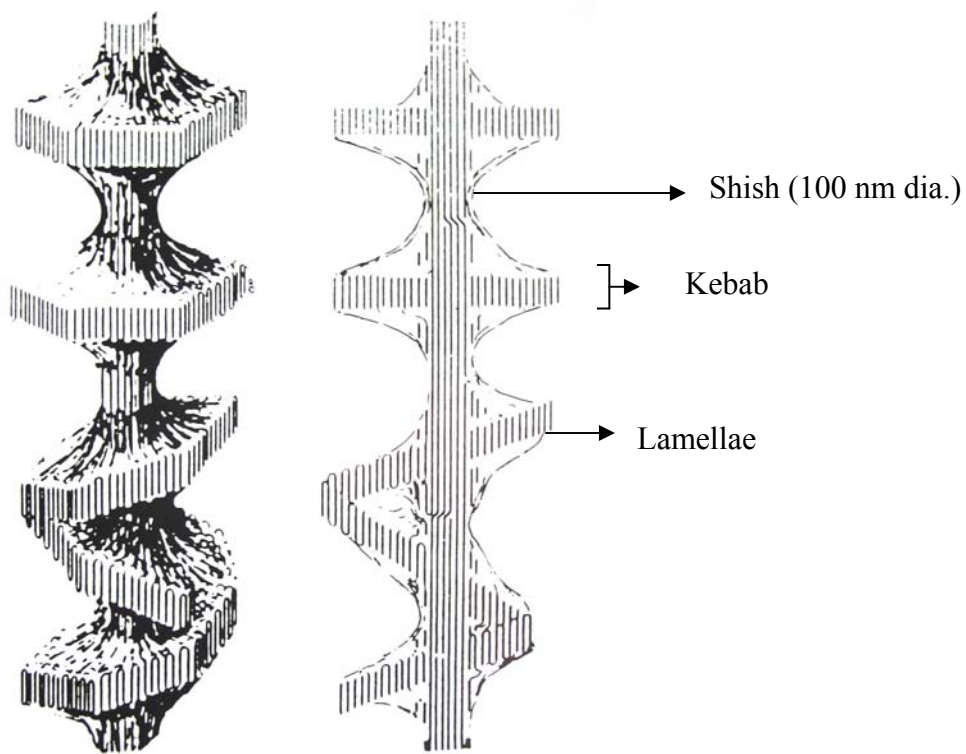
Figure 1.13 Schematic diagram of shish-kebab structure [66]

(Reproduced with permission from John Wiley & Sons Inc.)

1.4.1.1. Crystallinity of Polypropylene from Raman Spectroscopy

A typical Raman spectrum of polypropylene film is displayed in **Figure 1.14**. The peaks of interest are highlighted with the rectangular box. The band assignment [67] for different vibration modes is shown in **Table 1.2**. The 809 cm^{-1} and 841 cm^{-1} represents the helical conformation of the chains present in crystalline region and the isomeric defect phase, respectively. These two bands arise from the non-helical conformation at 830 cm^{-1} present in melt or amorphous phase.

Nielsen et al. [11] reported that the intensity sum of bands at 809 cm^{-1}, 830 cm^{-1}, and 841 cm^{-1} ($I_{809} + I_{830} + I_{841}$) is independent of chain conformation or crystallinity. Therefore, the total integral intensity under 809-841 cm^{-1} band is invariant of the state of the polymer and therefore can be used as an internal reference standard. The crystallinity values of polypropylene (PP) were calculated by dividing the integral intensity of 809 cm^{-1} peak (helical chain conformation) by the total integral intensity under 809-841 cm^{-1} band as described by Nielson et al. [11].

$$X_c = I_{809} / (I_{809} + I_{830} + I_{841})$$

The 830 cm^{-1} peak of the Raman spectrum was found to be very weak and does not significantly contribute for the crystallinity values. The final crystallinity values calculated from Nielsen's method [11] also correlated to DSC results as $X_{c, Raman} = 0.9 \, X_{c, DSC}$.
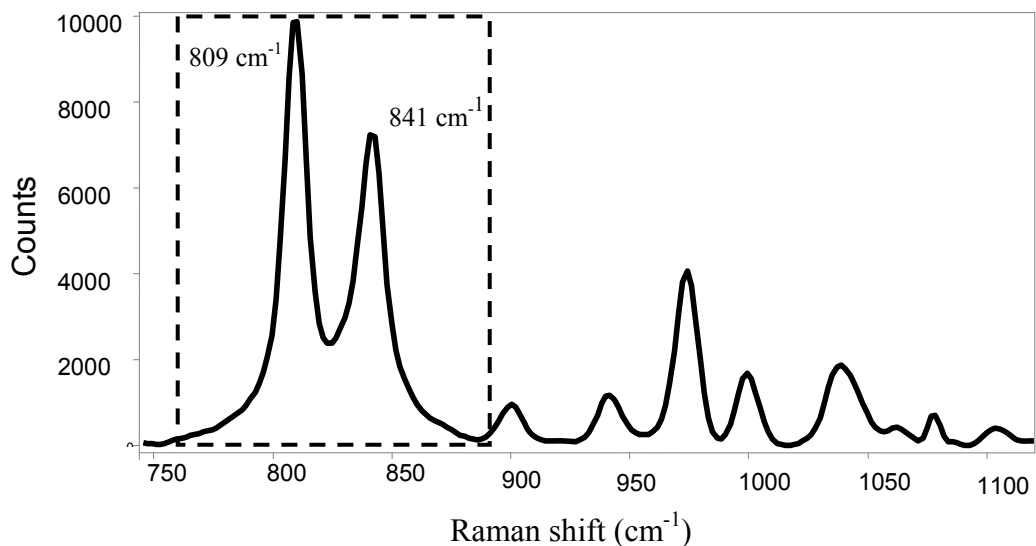
Figure 1.14 Raman spectrum of isotactic polypropylene film

Table 1.2 Assignments of the Raman bands of isotactic polypropylene [67]

Wavenumber (cm^{-1})	Vibrational band
809	r (CH_2) , ν (C-C)
841	r (CH_2)
972	r (CH_3) , ν (C-C)
998	r (CH_3)
1151	ν(C-C) , δ(CH)
1168	r (CH3) , ν(C-C) , ω(C-C)
1220	ν(C-C) , ω(CH) , τ(CH2)
1435	δ(CH_2)
1458	δ(CH_2)

ν = stretching, r = rocking, τ = twisting, ω = wagging,

δ = bending (s = symmetric, as = asymmetric)

1.4.1.2. X-ray diffraction of Polypropylene

Figure 1.15 displays a wide-angle X-ray diffractogram from a single-layer polypropylene film. The pattern consists of dark amorphous regions overlaid with the crystalline arcs and rings corresponding to different diffraction planes of the crystals. The distribution and the thickness of the arcs in the pattern correspond to orientation of a specific plane and crystal sizes respectively. The arcs of interest for polypropylene are (110), (040) and (130) that are observed at diffraction angles of 14.5°, 17° and 18°, respectively.
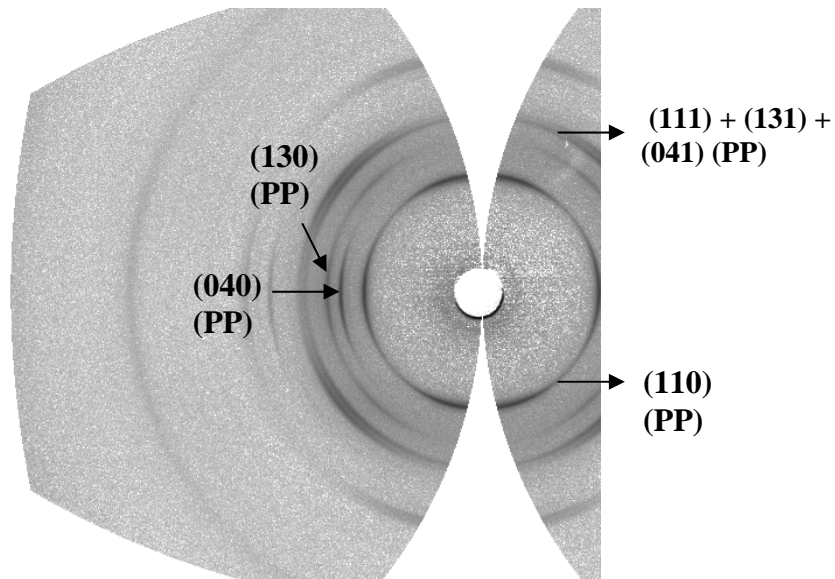
Figure 1.15 X-ray diffraction pattern of a polypropylene film with arcs of interest

Figure 1.16 displays the 2θ-intensity spectrum from the WAXD pattern of PP film with its characteristic crystalline peaks and amorphous halo. The 2θ-intensity spectrum of the WAXD pattern is obtained after appropriate background subtraction and Fraser's corrections. To calculate crystallinity using the 2θ-intensity spectrum, the integral area under the crystalline peaks (I_c) and amorphous regions (I_a) are estimated and the crystalline fraction is determined using the ratio of the crystalline peaks and the total integral area i.e., $X_c=I_c/(I_c+I_a)$. This determination of crystallinity is achieved by deconvolution of the peaks by integrated intensity from the WAXD spectrum.
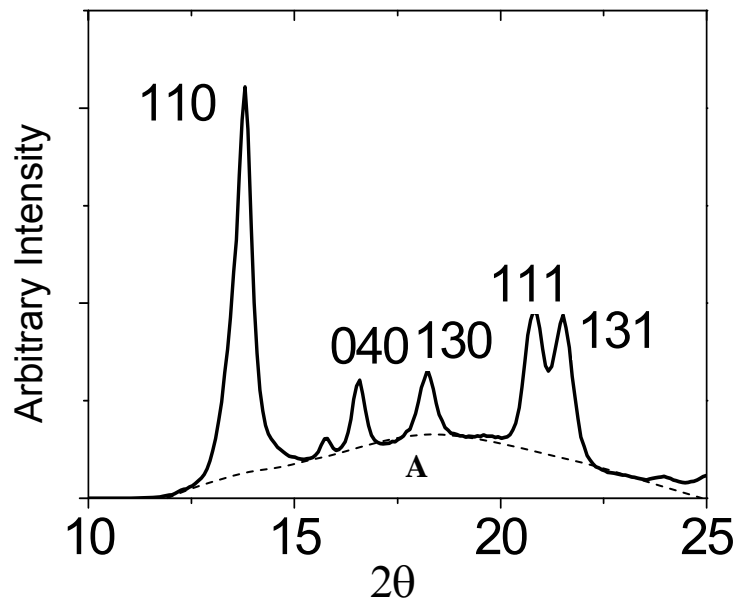
Figure 1.16 Normalized intensity spectrum from WAXD pattern of PP blown film

In polymers, the crystals have preferential orientation that depends on the processing conditions used. The WAXD patterns show circular patterns if there is random orientation in the sample while the patterns display demarcated arcs either at the meridian or the equator if there is preferrential orientation in the sample. The arcs in film or fiber samples are quantified for orientation values along different crystallographic axes using the Hermans' orientation factors, defined for a uniaxial orientation assumption as [35]:

$$f = 0.5 \ (3 <\cos^2 \varphi> - 1)$$

where $<\cos^2 \varphi>$ is the average value of the cosine squared of the angle φ between the film machine direction and a crystallographic axis. The orientation factor f is zero for a random orientation, and 1.0 and -0.5 for a perfectly oriented sample parallel and perpendicular to the machine direction, respectively.

For isotactic polypropylene, as there is no reflection associated with (001) planes (c-axis) [35] in the α phase, the f_c is calculated from the diffraction intensities from (110) and (040) planes based on the unit cell geometry [68] :

$$<\cos^2\Phi_c> = 1 - 1.099 <\cos^2\Phi_{110}> - 0.901 <\cos^2\Phi_{040}>$$

where $<\cos^2\Phi_{110}>$ and $<\cos^2\Phi_{040}>$ were obtained from azimuthal intensity measurements on the (040) and (110) reflections, respectively. The value of f_b can be computed from the

intensity distribution in the (040) reflection, while $f_{a'}$, describing the orientation of a non-principal crystallographic axis (a') defined perpendicular to the b- and c-axes, can be estimated using the equation: $f_a + f_b + f_c=0$ (with $f_{a'}$ substituted for f_a). The principal a-axis for i-PP monoclinic crystal makes an angle of 99.3° to the c-axis as was shown in **Figure 1.12**.

1.4.2. Polyethylene

Polyethylene is a polymer consisting of long chains of ethylene ($-CH_2-CH_2-$) as repeat unit. Polyethylene can be produced by polymerization of ethylene using either free-radical polymerization, anionic polymerization, or cationic polymerization on a single-site catalyst. Each of these methods results in different types of polyethylene: LDPE, LLDPE, HDPE and UHMWDPE [69].

Low-density polyethylene (LDPE) is produced by high-pressure ($\approx$3000 bar) free-radical polymerization. The high degree of branches with long molecular chains gives LDPE excellent flow properties making it easier to process compared to other polyethylenes [69].

The crystal structure in polyethylene is orthorhombic with two chains per unit cell. The unit-cell dimensions [69] are a=0.741 nm, b=0.495 nm and c=0.255 nm. **Figure 1.17** displays the unit cell of a polyethylene crystal with two repeat unit passes of zig-zag chains. The dominant arrangement of the crystals of PE is the row-nucleated structure as shown in **Figure 1.18,** which occurs when the polymer is crystallized from the melt under

stress. The Keller-Machin model has been widely used to explain the morphology of polyethylene blown films [70, 71] and fibers [28]

Front view   **Top view**
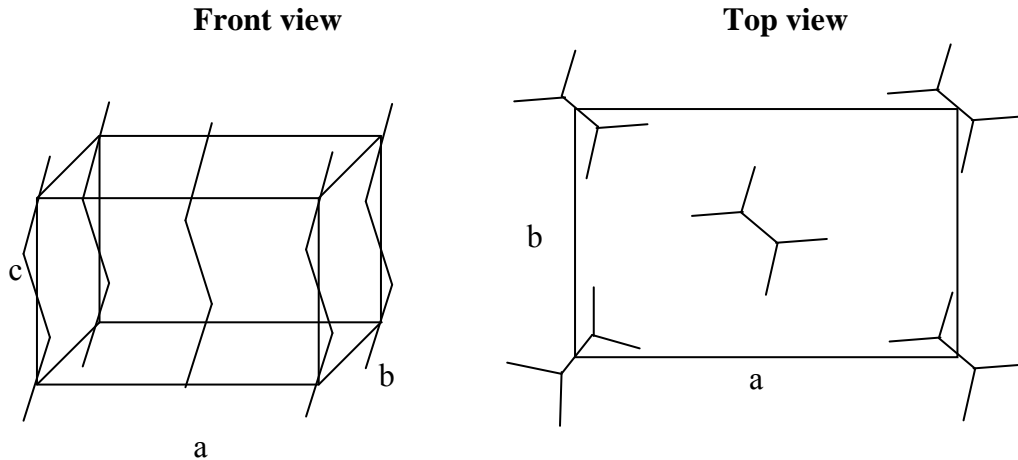
Figure 1.17 Polyethylene orthorhombic unit cell

At low stress, twisted lamellae are formed with b-axis perpendicular to MD, while a-axis is partially oriented in the MD (Keller-Machin Type I morphology). At high stress, untwisted lamellae grow radially outward from the high MW fibrils with c-axis oriented in the MD (Keller-Machin Type II morphology) and b-axis perpendicular to MD. **Figure 1.18** shows the row-nucleated crystalline structure of polyethylene grown at low and high stress of the melt. The extent of row-nucleation depends on the applied stress from the processing condition. At very low stress, lamellae are disordered and the row-nucleated

structure is less distinct while at intermediate and high stresses, a perfect row-nucleated structure is formed.

The density of LDPE ranges from 0.910 to 0.925 g/cm^3 and its crystallinity is typically less than 40 wt %. This results in excellent transparency, good sealability, low tensile strength and high ductility of the films. LDPE is used in high-volume film applications such as industrial plastic bags and film wrap.
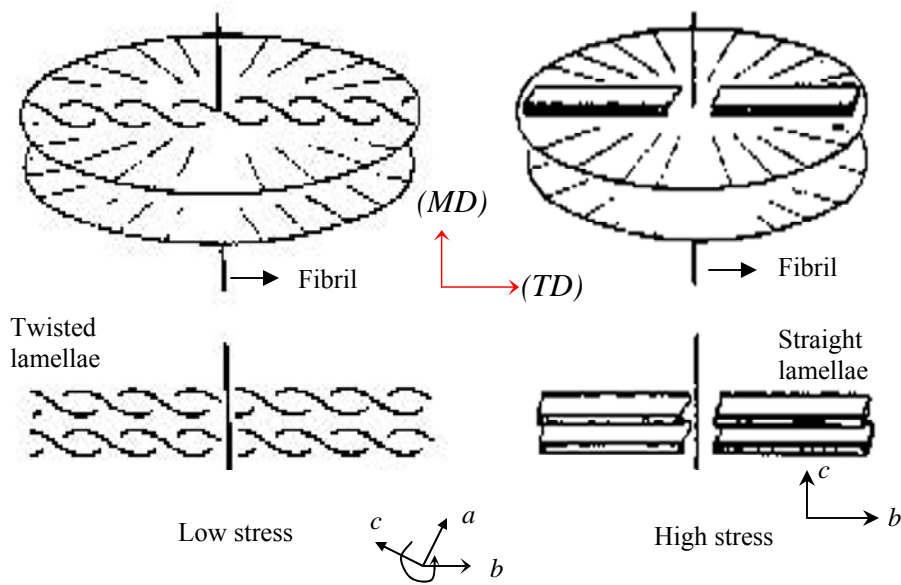
Figure 1.18 Keller-Machin Type row-nucleated structure of polyethylene [28]

(Reproduced with permission from John Wiley & Sons Inc.)

1.4.2.1. Crystallinity of Polyethylene from Raman Spectroscopy

Figure 1.19 presents a typical Raman spectrum of a polyethylene film in the 1000-1500 cm^{-1} region [10]. The band assignment for different vibrational modes [72] in the spectral range of interest is shown in **Table 1.3.** The spectrum consists of information about the three phases in polyethylene: an orthorhombic crystalline phase (α_c), a melt like amorphous phase (α_a) and an intermediate disordered phase of anisotropic nature (α_b), where chains are oriented without any lateral order [10, 73]. Their contents are determined from the integral intensities of the characteristic bands, the weight of the orthorhombic crystalline component being proportional to that at CH$_2$ wagging band at 1418 cm^{-1}.

To determine the crystalline content, the integral intensity of the 1418 cm^{-1} band is normalized using a standard reference band [10]. The CH$_2$ twisting region near 1300 cm^{-1}, which is invariant with the state of the polymer, was used as a reference band. The calculated integral intensity ratio of the final film samples I$_{1418/1300}$ were calibrated to crystallinity values based on primary measurement techniques, such as DSC and WAXS, according to the procedure of Strobl and Hagedorn [10].
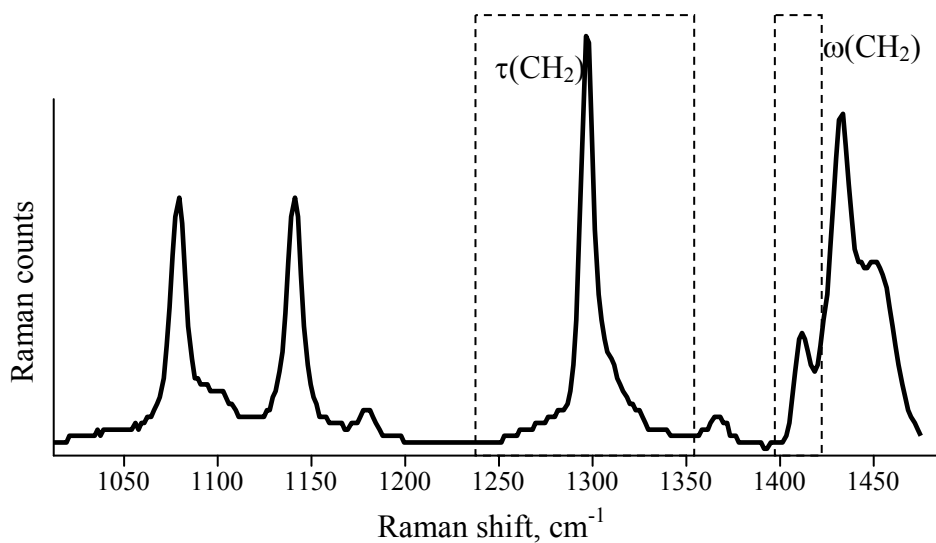
Figure 1.19 Raman spectrum of a polyethylene film

Table 1.3: Assignments of the Raman bands of polyethylene [72]

Wavenumber (cm^{-1})	Vibrational band
1060	ν_s (C-C)
1080	ν_s (C-C)
1130	ν_{as} (C-C)
1170	$r(CH_2)$
1296	$\tau(CH_2)$
1310	$\tau(CH_2)$
1370	$\omega(CH_2)$
1418	$\omega(CH_2)$
1440	$\delta(CH_2)$
1460	$2Xr(CH_2)$

ν = stretching, r = rocking, τ = twisting, ω = wagging, δ = bending (s = symmetric, as = asymmetric)

1.4.2.2. X-ray diffraction of Polyethylene

Figure 1.20 presents the WAXD pattern for single-layer PE blown film. The prominent crystallographic planes of interest in polyethylene are the (110), (200) and (020) peaks at diffraction angles of 21.6°, 23.8° and 36.2°, respectively. The two intense peaks at (110) and (200) shown in the intensity spectrum (**Figure 1.21**) are used to calculate the orthorhombic crystalline content [35].

The $<\cos^2 \varphi>$ values from the azimuthal intensity distributions of (200) and (020) are used to calculate Herman's orientation parameters: f_a and f_b, respectively. For the orthorhombic cell, the value of f_c could be obtained using the equation:

$$f_a + f_b + f_c = 0$$
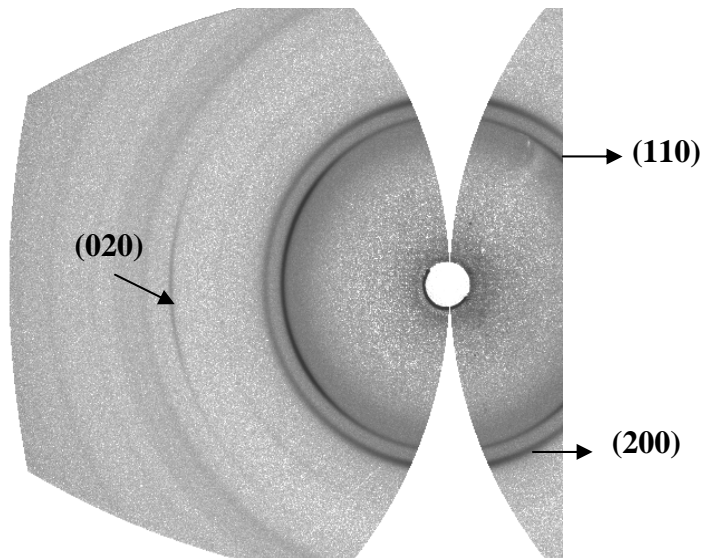
Figure 1.20 X-ray diffraction pattern of single-layer LDPE film
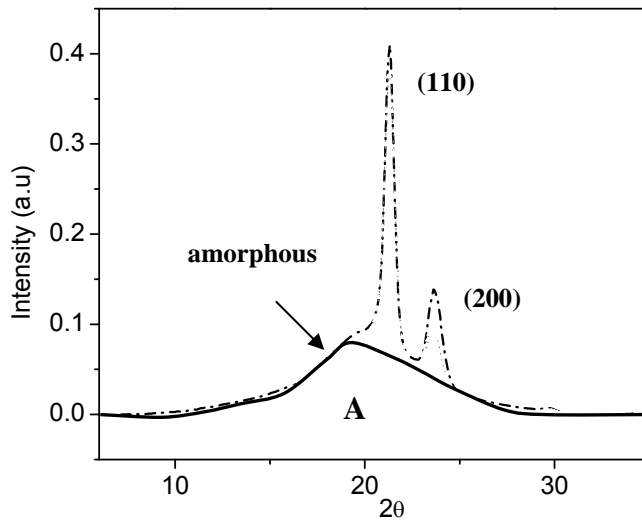
Figure 1.21 Normalized intensity spectrum from WAXD pattern of LDPE blown film

1.5. Real-Time Measurements during Blown Film Extrusion

As discussed earlier, Raman spectroscopy is a portable and much simpler technique as compared to other techniques for real-time microstructural measurements. It may provide a practical platform for large-scale and high speed industrial film fabrication settings, typically as tall as 15 m with line-speeds as high as 60 m/min [39]. In the

following sub-sections, the application of Raman spectroscopy for real-time microstructural measurements during film blowing operation is presented.

1.5.1.   Single-layer Blown Film Extrusion

1.5.1.1. Real-Time Raman Spectroscopy

Studies conducted by Srinivas et al. [34] presented the first real-time Raman measurements along the blown film line. Real-time Raman spectra along the axial distance are displayed in **Figures 1.22**, for one set of processing conditions. The spectrum at the die exit is that for a melt, and consists of three broad bands at 1080, 1305, and 1440 cm^{-1}, all for the amorphous melt. As the polymer melt cools down, the crystallization causes the intensity of C-C stretching vibrations at 1060 and 1130 cm^{-1} to increase at the expense of an amorphous peak at 1080 cm^{-1}. Also, the broad amorphous – CH$_2$ twisting vibration at 1300 cm^{-1} splits into a narrow crystalline band at 1296 cm^{-1} and a broad amorphous band at 1305 cm^{-1}. Finally, the –CH$_2$ bending vibration (1440 cm^{-1}) in the amorphous region is transformed into three bands (1418, 1440, and 1460 cm^{-1}), of which the –CH$_2$ wagging vibration at 1418 cm^{-1} is used to estimate the orthorhombic crystalline content of PE [10].

Figure 1.22 also shows that as the polymer travels from a location below the frost line to that above, the intensity of 1418 cm^{-1} peak steadily increases as a consequence of

crystallization. As the melt is subjected to an under-cooling, nucleation occurs followed by crystallization. Ultimately, these processes slow down as the bubble temperature decreases to ambient. Thus, real-time Raman spectroscopy enabled measurement of phase transformation during the film process.
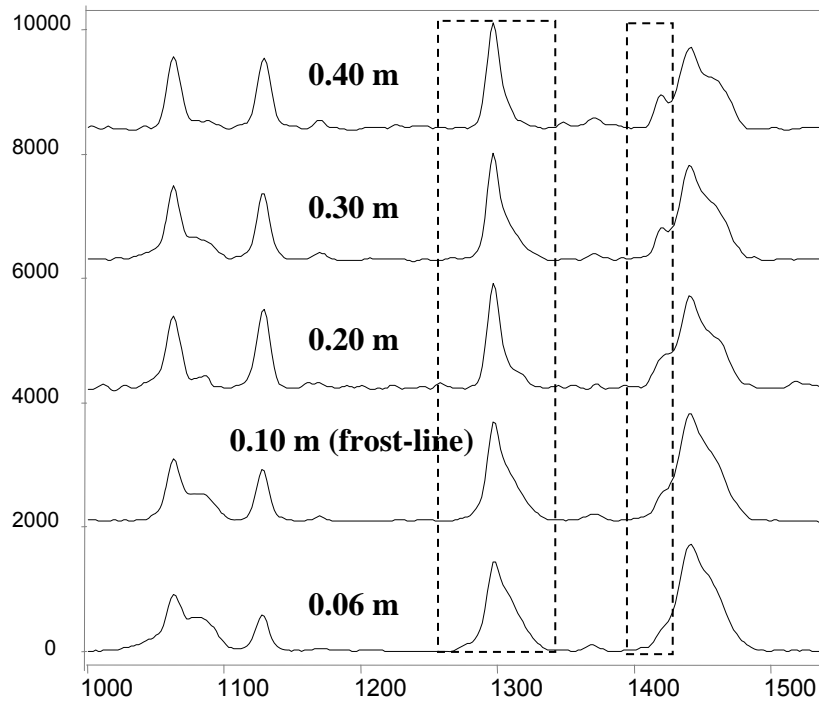
Figure 1.22 Raman spectra for linear low-density polyethylene in the range of 1000 – 1500 cm^{-1} along the axial distance of the blown film line [34] (Reproduced with permission from Dr. Cherukupalli, Clemson University, 2005)

The crystallinity profile, presented in **Figure 1.23**, shows a steep initial increase immediately after the frost-line, but then plateaus at higher axial distance. A real-time temperature profile, obtained using an IRCON Infrared pyrometer, shows a plateau at ≈104°C as a consequence of the exothermic heat of crystallization.
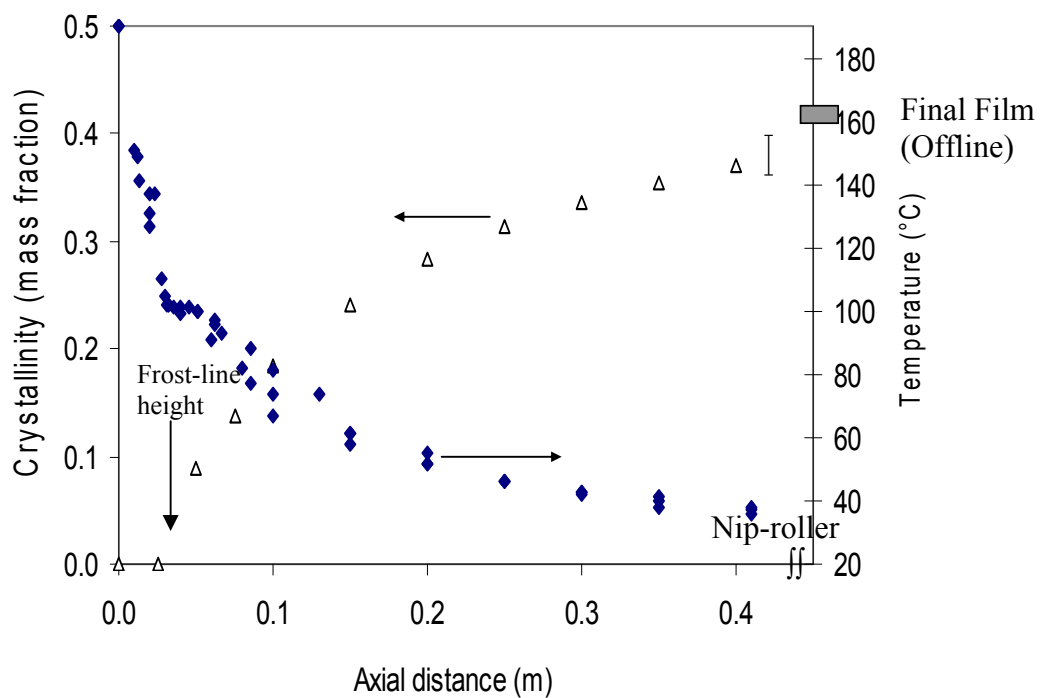
Figure 1.23 Crystallinity profile for LLDPE as a function of axial distance of the blown film line [34] (Reproduced with permission from Dr. Cherukupalli, Clemson University, 2005)

The development of crystallinity was reported to be significantly different when plotted as a function of time as compared to that along the axial distance. The process time is defined as the time taken for a particle exiting the die to reach a particular location along the film line. They reported an increase in the crystallization growth rate with an increase in TUR is an indication of flow enhanced crystallization. [71, 74, 75]

Another important aspect of microstructure that affects the mechanical properties of the films is the two-dimensional order in the film i.e., orientation of the molecular chains which is influenced by processing conditions [39]. Techniques such as wide-angle X-ray diffraction (WAXD), birefringence, fluorescence polarization, infrared spectroscopy (IR), nuclear magnetic resonance spectroscopy (NMR), and Raman spectroscopy are typically used to characterize molecular orientation in polymer samples [35, 76-79]. X-ray diffraction provides crystalline orientation values in the sample whereas birefringence gives information on the overall molecular orientation. Vibrational spectroscopic techniques such as infrared (IR) and Raman spectroscopy can measure the orientation information of crystalline and the amorphous phases individually. Of these, Raman spectroscopy offers distinct advantages[19] over other spectroscopic techniques because it is portable and amenable to fiber optics. The technique requires little sample preparation and is not influenced by humidity in the environment. Although more complex than IR spectroscopy from both an experimental and theoretical point of view, Raman spectroscopy enables determination of higher moments ($\langle P_4(\cos\theta)\rangle$) of the orientation distribution function.

Several studies have reported on the use of offline polarized Raman spectroscopy to estimate orientation in films [12, 14, 80, 81] and fibers [13, 82]. The detailed procedure for determining the orientation of the polymer specimens by polarized Raman spectroscopy was presented by Bower [83]. Later studies [12, 14, 80, 81] proposed approaches to simplify the experimental complexities.

Jarvis et al. [12] characterized the biaxial orientation in poly (ethylene terephthalate) (PET) films assuming cylindrical symmetry of principal Raman tensors ($a_1=a_2=-0.18$) for the benzene ring vibration (C=C stretch) at 1616 cm^{-1}. Studies by Pigeon et al. [14], Citra et al. [13], and Maxfield et al. [81] have reported a detailed experimental procedure for characterizing the uniaxial orientation in polyethylene fibers and films. They noted that the principal components of the Raman tensor for specific vibrations of polyethylene are not cylindrical ($a_1 \neq a_2$) due to the planar zigzag structure of the molecular chains. A complete list of assignment of Raman lines for a polyethylene chain present in the crystalline and amorphous phases along with vibration modes and space group geometries is given by Bentley and Hendra [72]. The 1130 cm^{-1} band in polyethylene corresponds to the stretching vibration of the C-C symmetrical bond of all-*trans* conformation of the chain and has been used in literature studies [13, 14, 81] to measure orientation parameters of PE samples.

Most of the past studies [13, 14, 17, 81, 84] on polarized Raman spectroscopy of films characterized processed samples. The use of polarized Raman spectroscopy for real-time orientation measurements was first reported by Paradkar et al. [85] during fiber spinning of isotactic polypropylene. They used the ratio of Raman bands at 841/809 cm^{-1}

which is sensitive to the molecular anisotropy in PP, to estimate a semi-quantitative molecular orientation in the spin line for different throughput and draw ratios. **Figure 1.24** displays the real-time ZZ polarized Raman spectra for PP obtained at three different positions along the spin line. The ratio of 841/809 cm^{-1} was reported to decrease as the polymer travels from a position near the die to the position near the draw roll. The values for the intensity ratios of the Raman bands for different take-up speeds were reported to linearly correlate with its birefringence values.

It is noted, however that the use of real-time polarized Raman spectroscopy has not been reported in literature studies for measuring molecular orientation development during blown film extrusion.
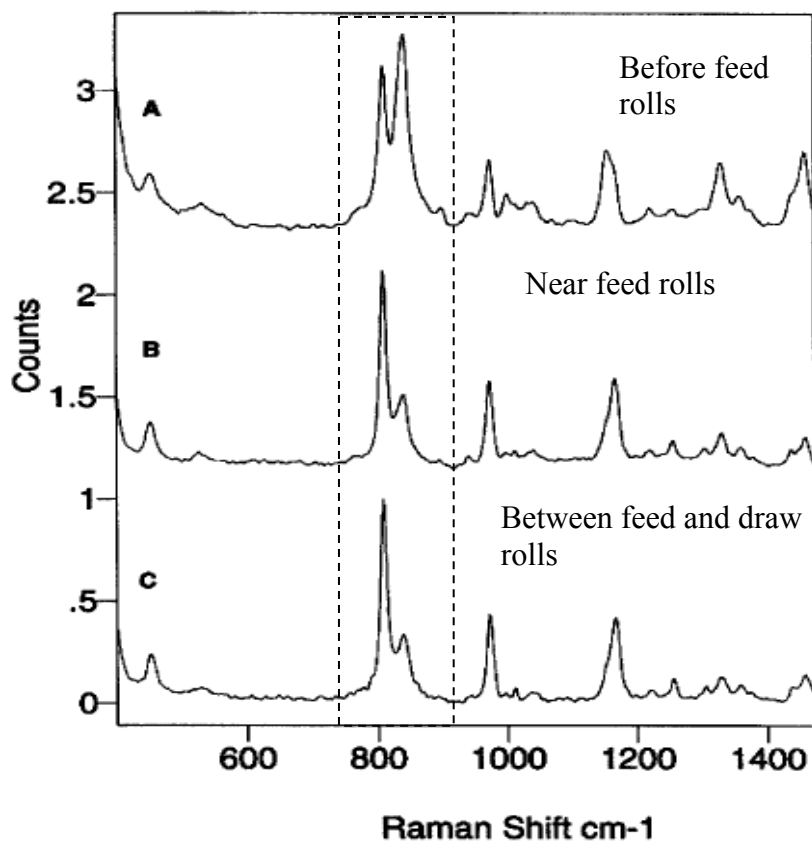
Figure 1.24 ZZ polarized Raman spectra showing development of molecular orientation in polypropylene at three different locations in the fiber-spinning line. [85] (Reproduced with permission from Society for Applied Spectroscopy)

45

1.5.1.2. Real-time Wide-Angle X-ray Diffraction Measurements

Although X-ray diffraction has been applied to characterize microstructure in both film and fiber, most of the studies on film are carried out as *ex situ* or offline. The use of an *in situ* X-ray diffraction technique has been primarily limited to fiber spinning operations and there are several publications [28-30, 86, 87] dating prior to 1970 till recent years. The pioneering work on online WAXD measurements during melt spinning of HDPE, LLDPE, PP and poly(1-butene) has been carried out by Katayama et al. (1968) [86] and Spruiell and co-workers (1970) [28, 29]. They combined temperature, diameter, velocity measurements along with structural measurements to understand flow-induced phenomenon during the process. Their study [28, 29] also reported orientation in polyethylene fibers at high and low take up speeds and investigated the formation of spherullitic, twisted and straight row-nucleated lamellar structure in PE. These studies used an X-ray source with a fixed beam line and moved the extruder to study the microstructure development along the axial distance in spinline. Later studies [87-89] used synchrotron X-ray sources that reduced the accumulation time for the X-ray pattern from 30 mins to time as low as 30 seconds.

Recent studies by Lopes et al. [90] at CAEFF conducted online X-ray diffraction (WAXD and SAXS) during melt spinning of isotactic polypropylene and the results were used to validate the experimental fiber spinning model developed by McHugh et al.[91]. Their study was carried out on a fiber bundle, complemented with diameter, velocity and temperature data on single fibers.

It is well known that vibrational spectroscopic techniques such Raman spectroscopy and FTIR are not primary measurement techniques [19]. The integral intensities from Raman spectra are usually calibrated using primary measurement techniques such as differential scanning calorimetry (DSC), density measurements or X-ray diffraction [10]. Therefore, simultaneous measurement of crystallinity using online WAXD and Raman spectroscopy will validate the data from vibrational spectroscopic technique on different states of the polymer. Similar simultaneous measurements using WAXD and Raman spectroscopy during polypropylene fiber spinning have been conducted by Panadana et al. [92] and a linear correlation between crystallinities calculated using online Raman spectroscopy and online WAXD was reported.

Unlike fiber-spinning, where the WAXD is performed on a single or bundle of filaments [28, 92], bubble geometry (hollow cylinder) adds to the complexity of real-time WAXD measurements during film blowing. The use of high intensity X-ray sources, such as synchrotron radiation, can reduce data collection time during continuous processing, but the equipment is typically not easily accessible. The application of online X-ray diffraction technique (lab-source X-ray) for real-time microstructural measurements during single-layer blown film extrusion need to be explored.

1.5.2. Multi-layer Blown Film Extrusion

1.5.2.1. Real-time Measurements

As discussed in previous sections, a large number of past research studies have focused on relating processing parameters with kinematics and film properties in single-layer blown films [25, 52]. The online microstructural development in single component fibers [30] and blown films [25, 27, 34] for different polyolefins, as a function of processing parameters, has been well studied. In contrast, only a few studies have been reported in the literature that addresses real-time measurements during the multi-layer blown film process [93].

For multi-layer blown film coextrusion, the process dynamics are different than single-layer blown film extrusion. Here, the layer which freezes first determines the location of maximum strain-rate. As noted earlier, the strain-rate is dependent on the change in velocity with distance. Therefore, after the first layer freezes, there is no change in velocity of the molten second layer. This can cause a decrease in orientation of the molecular chains in the second layer.

Typically, literature studies have reported the end use properties such as barrier [94], peel strength [95], optical [96] and mechanical strength [94, 97, 98], for multi-layer films. The kinematics and microstructural studies on multi-layer blown films are limited [93]. Morris [93] studied the effect of interaction of different polymers on bubble kinematics, temperature and film properties and suggested that film properties are

significantly changed as compared to single-layer film, even with the presence of small amount of a second polymer. **Figure 1.25** shows the strain-rate experienced by the bubble in the machine direction (MD) in single-layer HDPE and coextruded HDPE/EVOH blown films. The maximum strain-rate for HDPE/EVOH bilayer film occurs at higher temperature (after solidification of EVOH) compared to single layer HDPE film. This could cause significant relaxation of the molecular chains in HDPE layer during coextrusion. His study reported significant reduction in yield strength and tear strength of the HDPE layer compared to single layer HDPE films processed under similar condition. He reported that the additive rule, typically used for predicting the properties of the multi-layer films, may not apply to all types of coextruded blown films.
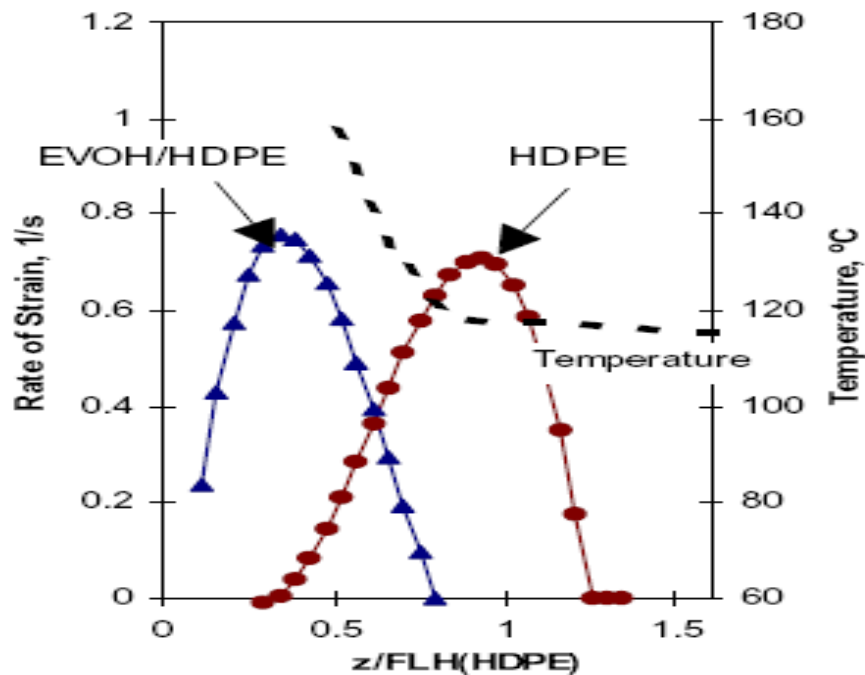
Figure 1.25 Machine direction strain rates (e_l) in the bubble for single-layer HDPE and EVOH/HDPE bilayer coextrusion [93]. [Reproduced with permission from Society of Plastics Engineers]

In recent years, multi-layer blown film extrusion is being increasingly utilized to make functional packaging films with the desired properties [40]. Systematic experimental studies addressing real-time microstructure development during coextrusion of different polymers are largely unavailable in the literature. Therefore, fundamental research is needed to understand the microstructure and process dynamics in the complex multi-layer blown film extrusion process.

1.6.   Processing-Structure-Properties in Blown Film Extrusion

Several researchers have reported on processing-structure-property correlation in single-layer blown films. The effect of processing parameters (TUR, BUR and FLH) on the tensile properties of single-layer HDPE and LDPE films was reported by Gupta et al [42].   Campbell et al.[52] correlated the tensile and impact properties of single-layer LLDPE blown films with strain and strain-rates experienced by the bubble during its formation and reported on the importance of strain-rate during crystallization for the final-film properties.

Studies by Han et al.[99] and Choi [100] reported that orientation factors of PE films are correlated only with stresses calculated at the FLH and did not consider the crystalline and orientation development after the FLH. However, studies by Srinivas [33, 34] monitored the real-time microstructural development in LLDPE blown film past the FLH and concluded that crystallization half-time as a valuable parameter for formulation

of processing-structure-property relations. The crystalline a- and c-axis orientation of LLDPE and i-PP films, respectively, was reported to increase with decreasing crystallization halftime. The transverse direction tensile modulus and tear strengths for LLDPE films also increased with decreasing half-time.[33]

One of the first studies reported in the literature on multi-layer blown films was carried out by Schrenk et al.[101, 102] in the early 1970s. Their study [101, 102] predicted layer distribution (thickness) in polystyrene/poly (methyl methacrylate) (PS/PMMA) multi-layer films using simple Newtonian flow equations and confirmed using electron microscopy images. Similar studies were conducted by Han et al. [103-105] in late 1970s and reported the effect of rhelogical parameters of LDPE and EVA polymers on the layer distribution by measuring the pressure-drop in the die, when different combinations of LDPE and EVA were coextuded. In the 1980s, there were several publications [106-109] and industrial patents [110, 111] that dealt with the design aspects of multi-layer blown film die with large interest in increasing the number of layers (upto 10 layers) in the multi-layer film [110, 111]

Later studies report on the adhesion between layers [95], flow instabilities at the interface [112, 113], properties [94, 114] of the multi-layer films. Two types of interaction are reported to occur at the interface of polymers that influence the adhesion between layers in coextruded films. One is mechanical locking between the two components to form strong interfacial bonds. Factors such as process time, glass transition temperature and compatibility of polymers determines this type of bonding.

51

Another factor is chemical interactions at the interface such as covalent, ionic or hydrogen bonding.

An important phenomenon that occurs during coextrusion of polymers is the interfacial instability which causes non-uniform layer distributions and unpredictable film properties. The primary cause of this type of instability is the viscosity ratio which increases the shear stress at the interface. The optical properties of the multi-layer film were reported [45, 96] to be affected by the interfacial instabilities.

Zhang and Ajji [114] characterized microstructure in LDPE/PET blown films using offline techniques such as birefringence and FTIR. Their study reported the structural changes (orientation and crystallinity) in the PET and LDPE layers for changing TUR, BUR, and FLH. The use of tie-layer resin (ethylene co-glycidyl methacrylate) between PET/LDPE layers did not significantly change the structure of the layers, but merely improved the adhesion between layers. They have also reported similar studies on PP/LLDPE multi-layer blown films [68].

Most of the studies reported in the literature characterized the multi-layer blown films using offline techniques. Because the microstructure of the film influences the mechanical and physical properties of the blown films, the real-time microstructure measurements help to understand the effect of coextruding two different polymers on the microstructure and properties.

1.7. Objectives

The primary objectives of this research were to:

1. Study the crystallinity and orientation development during blown film extrusion of a low-density polyethylene (LDPE) using real-time Raman spectroscopy;

2. Perform simultaneous real-time wide-angle X-ray diffraction and Raman spectroscopy measurements for crystallinity evolution during polyethylene blown film extrusion;

3. Conduct real-time Raman spectroscopy experiments to measure crystallinity of individual components, low-density polyethylene (LDPE) and polypropylene (PP), during LDPE/PP bilayer blown film coextrusion; and

4. To investigate the effect of coextrusion on the microstructure of the bicomponents films.

The remaining dissertation is organized as follows. Chapter 2 describes the protocol and the results from real-time orientation measurements conducted during single-layer blown film extrusion of low-density polyethylene using online polarized Raman spectroscopy. In Chapter 3, the feasibility of real-time wide-angle X-ray diffraction (WAXD) for blown film extrusion is established for the first-time, and a comparison of crystallinity profiles from real-time WAXD and Raman spectroscopy techniques is reported. In Chapter 4, the real-time Raman spectroscopic measurements on single-layer blown film are extended to bilayer blown film coextrusion of polyethylene

(LDPE) and polypropylene (PP). In Chapter 5, the crystallization-time difference between the components measured using online Raman spectroscopy is used to investigate the effect of coextrusion on the microstructure and morphology of the components in PP/LDPE bilayer blown film. Finally, Chapter 6 summarizes the conclusions drawn from this study, and provides recommendations for further studies.

1.8. References

1. van Overbeke E, Devaux J, Legras R, Carter JT, McGrail PT, and Carlier V. Applied Spectroscopy 2001;55(11):1514-1522.

2. Edwards HGM, Johnson AF, Lewis IR, Ward NJ, and Wheelwright S. Journal of Raman Spectroscopy 1993;24(8):495-500.

3. Tanto B, Guha S, Martin CM, Scherf U, and Winokur MJ. Macromolecules 2004;37(25):9438-9448.

4. De Santis A. Polymer 2005;46(14):5001-5004.

5. Parnell S, Min K, and Cakmak M. Polymer 2003;44(18):5137-5144.

6. Cappitelli F, Vicini S, Piaggio P, Abbruscato P, Princi E, Casadevall A, Nosanchuk JD, and Zanardini E. Macromolecular Bioscience 2005;5(1):49-57.

7. Zieba-Palus J and Borusiewicz R. Journal of Molecular Structure 2006;792:286-292.

8. Williams KPJ and Klenerman D. Journal of Raman Spectroscopy 1992;23(4):191-196.

9. Oldak D, Kaczmarek H, Buffeteau T, and Sourisseau C. Journal of Materials Science 2005;40(16):4189-4198.

10. Strobl GR and Hagedorn W. Journal of Polymer Science Part B-Polymer Physics 1978;16(7):1181-1193.

11. Nielsen AS, Batchelder DN, and Pyrz R. Polymer 2002;43(9):2671-2676.

12. Jarvis DA, Hutchinson IJ, Bower DI, and Ward IM. Polymer 1980;21(1):41-54.

13. Citra MJ, Chase DB, Ikeda RM, and Gardner KH. Macromolecules 1995;28(11):4007-4012.

14. Pigeon M, Prudhomme RE, and Pezolet M. Macromolecules 1991;24(20):5687-5694.

15. Everall N and King B. Macromolecular Symposia 1999;141:103-116.

16. Larsen RA. Raman spectroscopy of polymers. In: Craver CDC, Charles E., Jr, editor. Applied Polymer Science Oxford, UK, 2000. pp. 759-785.

17. Tanaka M and Young RJ. Journal of Materials Science 2006;41(3):963-991.

18. Pelletier MJ. Analytical applications of Raman spectroscopy. Oxford ; Malden, MA: Blackwell Science, 1999.

19. Lewis IR and Edwards HGM. Handbook of Raman spectroscopy : from the research laboratory to the process line. New York ; Basel: Marcel Dekker, 2001.

20. Bower DI and Maddams WF. The Vibrational Spectroscopy of Polymers. New York: Cambridge University Press, 1989.

21. Siessler HW and Holland-Moritz K. Infrared and Raman spectroscopy of polymers. NYC: Marcel Dekker Inc., 1980.

22. Marrow DG, Cochran AM, and Roger ST. US Patent. 2004063234, 1999.

23. Marrow DG, David A.; Veariel, Thomas R. US Patent. 20070019190, 2007.

24. Leugers MAS, Alison Kathleen; Weston, John W.; Sun, Zahn. Patent WO9927350, 1999.

25. Bullwinkel MD, Campbell GA, Rasmussen DH, Krexa J, and Brancewitz CJ. International Polymer Processing 2001;16(1):39-47.

26. Nagasawa Toshio MT, Hoshino Sadao. Appl Polym Symp 1973;20:275-293.

27. GhanehFard A, Carreau PJ, and Lafleur PG. International Polymer Processing 1997;12(2):136-146.

28. Dees JR and Spruiell JE. Journal of Applied Polymer Science 1974;18(4):1053-1078.

29. Spruiell JE and White JL. Polymer Engineering and Science 1975;15(9):660-667.

30. Hsiao BS, Barton R, and Quintana J. Journal of Applied Polymer Science 1996;62(12):2061-2068.

31. Lamberti G and Brucato V. Journal of Polymer Science Part B-Polymer Physics 2003;41(9):998-1008.

32. Paradkar RP, Sakhalkar SS, He X, and Ellison MS. Journal of Applied Polymer Science 2003;88(2):545-549.

33. Cherukupalli SS, Gottlieb SE, and Ogale AA. Journal of Applied Polymer Science 2005;98(4):1740-1747.

34. Cherukupalli SS and Ogale AA. Polymer Engineering and Science 2004;44(8):1484-1490.

35. Alexander LE. X-ray diffraction methods in polymer science. Huntington, N.Y.: Krieger Pub. Co., 1979.

36. Lu JJ, Sue HJ, and Rieker TP. Journal of Materials Science 2000;35(20):5169-5178.

37. Lahrouni A and Arman J. European Polymer Journal 1995;31(4):347-352.

38. Furukawa T, Sato H, Kita Y, Matsukawa K, Yamaguchi H, Ochiai S, Siesler HW, and Ozaki Y. Polymer Journal 2006;38(11):1127-1136.

39. Kanai T and Campbell GA. Film processing. Cincinnati, Ohio: Hanser/Gardner Publications, 1999.

40. Abdel-Bary E. Handbook of Plastic Films. Shawbury, U.K: Rapra Technology, 2003.

41. Ajji A, Zhang X, and Elkoun S. Polymer 2005;46(11):3838-3846.

42. Gupta A, Simpson DM, and Harrison IR. Journal of Applied Polymer Science 1993;50(12):2085-2093.

43. Kissin YV. Journal of Polymer Science Part B-Polymer Physics 1992;30(10):1165-1172.

44. Krishnaswamy RK and Lamborn MJ. Polymer Engineering and Science 2000;40(11):2385-2396.

45. Patel R, Ratta V, Saavedra P, and Li J. Journal of Plastic Film & Sheeting 2005;21(3):217-231.

46. Henrichsen LK and McHugh AJ. International Polymer Processing 2007;22(2):190-197.

47. Henrichsen LK, McHugh AJ, Cherukupalli SS, and Ogale AA. Plastics Rubber and Composites 2004;33(9-10):383-389.

48. Cao BS and Campbell GA. Aiche Journal 1990;36(3):420-430.

49. Petrie CJS. Polymer Engineering and Science 1975;15(10):708-724.

50. Pirkle JC and Braatz RD. Polymer Engineering and Science 2003;43(2):398-418.

51. Zatloukal M and Vlcek J. Journal of Non-Newtonian Fluid Mechanics 2004;123(2-3):201-213.

52. Campbell GA and Babel AK. Macromolecular Symposia 1996;101:199-206.

53. Cherukupalli SS, Gottlieb SE, and Ogale AA. Journal of Applied Polymer Science 2005;98(4):1740-1747.

54. Cherukupalli SS and Ogale AA. Plastics Rubber and Composites 2004;33(9-10):367-371.

55. Halter H and Caspar G. Kunststoffe-German Plastics 1983; 73(10):597-598.

56. Colvin R. Modern Plastics 1999; 76(8):56-59.

57. Sidiropoulos V and Vlachopoulos J. Polymer Engineering and Science 2000; 40(7):1611-1618.

58. Sidiropoulos V and Vlachopoulos J. International Polymer Processing 2001; 16(1):48-53.

59. Sawyer L and Grubb D. Polymer Microscopy, Second ed. London, UK: Chapman & Hall, 1996.

60. Southern JH. Polymer Engineering and Science 1976; 16(3):125-125.

61. Henrichsen LK and McHugh AJ. International Polymer Processing 2007;22(2):179-189.

62. Kumar A and Gupta RK. Fundamentals of polymers. New York: McGraw-Hill, 1998.

63. Broda J. Journal of Applied Polymer Science 2003;90(14):3957-3964.

64. Bruckner S, Phillips PJ, Mezghani K, and Meille SV. Macromolecular Rapid Communications 1997;18(1):1-7.

65. Obadal M, Cermak R, and Stoklasa K. Macromolecular Rapid Communications 2005;26(15):1253-1257.

66. Pennings AJ. Journal of Polymer Science Part C-Polymer Symposium 1977(59):55-86.

67. deBaez MA, Hendra PJ, and Judkins M. Spectrochimica Acta Part a-Molecular and Biomolecular Spectroscopy 1995;51(12):2117-2124.

68. Zhang XM and Ajji A. Polymer 2005;46(10):3385-3393.

69. Peacock AJ. Handbook of polyethylene : structures, properties, and applications. New York: Marcel Dekker, 2000.

70. Keller A and MJ Machin. Journal of Macromolecular Science, Physics B 1967;1(1).

71. Keller A and Kolnaar JWH. Orientational Phenomena in Polymers: Springer Berlin / Heidelberg, 1993.

72. Bentley PA and Hendra PJ. Spectrochimica Acta Part a-Molecular and Biomolecular Spectroscopy 1995;51(12):2125-2131.

73. Clas SD, Heyding RD, Mcfaddin DC, Russell KE, Scammellbullock MV, Kelusky EC, and Stcyr D. Journal of Polymer Science Part B-Polymer Physics 1988;26(6):1271-1286.

74. Kolnaar JWH, Keller A, Seifert S, Zschunke C, and Zachmann HG. Polymer 1995;36(20):3969-3974.

75. Mchugh AJ. Polymer Engineering and Science 1982;22(1):15-26.

76. Strobel JM and Nam S. Journal of Applied Polymer Science 1991;42(1):159-168.

77. Schartel B, Wachtendorf V, Grell M, Bradley DDC, and Hennecke M. Physical Review B 1999;60(1):277-283.

78. Zhang XM, Elkoun S, Ajji A, and Huneault MA. Polymer 2004;45(1):217-229.

79. Schmack G, Schreiber R, Veeman WS, Hofmann H, and Beyreuther R. Journal of Applied Polymer Science 1997;66(2):377-385.

80. Kip BJ, Vangurp M, Vanheel SPC, and Meier RJ. Journal of Raman Spectroscopy 1993;24(8):501-510.

81. Maxfield J, Stein RS, and Chen MC. Journal of Polymer Science Part B-Polymer Physics 1978;16(1):37-48.

82. Lu S, Russell AE, and Hendra PJ. Journal of Materials Science 1998;33(19):4721-4725.

83. Bower DI. J Polym Sci Pol Phys Ed 1972;10:2135-2153.

84. Voyiatzis G, Petekidis G, Vlassopoulos D, Kamitsos EI, and Bruggeman A. Macromolecules 1996;29.

85. Paradkar RP, Sakhalkar SS, He XJ, and Ellison MS. Applied Spectroscopy 2001;55(5):534-539.

86. Katayama K, Amano T, and Nakamura K. Kolloid-Zeitschrift and Zeitschrift Fur Polymere 1968;226(2):125

87. Samon JM, Schultz JM, Wu J, Hsiao B, Yeh F, and Kolb R. Journal of Polymer Science Part B-Polymer Physics 1999;37(12):1277-1287.

88. Samon JM, Schultz JM, Hsiao BS, Khot S, and Johnson HR. Polymer 2001;42(4):1547-1559.

89. Wu G, Li HW, Wu YQ, and Cuculo JA. Polymer 2002;43(18):4915-4922.

90. Lopes PE. Ph.D. Dissertation, Clemson University, 2005.

91. McHugh AJ and Doufas AK. Composites Part a-Applied Science and Manufacturing 2001;32(8):1059-1066.

92. Pandana DV Mater's Thesis, Clemson University, 2007.

93. Morris BA. Journal of Plastic Film & Sheeting 1999;15(1):25-36.

94. Huang CH, Wu JS, and Huang CC. Polymer Journal 2004;36(5):386-393.

95. Poon BC, Chum SP, Hiltner A, and Baer E. Polymer 2004;45(3):893-903.

96. Zimmerman D. The effect of tie-layers on optical properties of coextruded multilayer films. ANTEC - Society of Plastics Engineers, vol. 2: Society of Plastics Engineers, 2000. pp. 1915-1917.

97. Elkoun S, Huneault MA, McCormick K, Puterbaugh F, and Kale L. Polymer Engineering and Science 2005;45(9):1214-1221.

98. Martin O, Schwach E, Averous L, and Couturier Y. Starch-Starke 2001;53(8):372-380.

99. Kwack TH and Han CD. Journal of Applied Polymer Science 1988;35(2):363-389.

100. Choi KJ, Spruiell JE, and White JL. Journal of Polymer Science Part B-Polymer Physics 1982;20(1):27-47.

101. Schrenk WJ and Alfrey T. Spe Journal 1973;29(6):38-42.

102. Schrenk WJ and Alfrey T. Spe Journal 1973;29(7):43-47.

103. Han CD and Shetty R. Polymer Engineering and Science 1976;16(10):697-705.

104. Han CD and Shetty R. Polymer Engineering and Science 1978;18(3):180-186.

105. Han CD and Shetty R. Polymer Engineering and Science 1978;18(3):187-199.

106. Hensen F, Hessenbruch R, and Bongaerts H. Kunststoffe-German Plastics 1981;71(9):530-538.

107. Hessenbruch R. Kunststoffe-German Plastics 1987;77(5):475-479.

108. Prall GM. Tappi Journal 1985;68(2):78-81.

109. Snyder MR. Modern Plastics 1995;72(4):95

110. Mavridis H. US Patent, 5716650, 1998.

111. Galloway, DE, Lind KD, Kittel, DJ, Walburn, GH, US Patent, 7316833, 2008

112. Valette R, Laure R, Demay Y, and Agassant JF. International Polymer Processing 2004;19(2):118-128.

113. Zatloukal M and De Witte J. Plastics Rubber and Composites 2006;35(4):149-154.

114. Zhang XM, Ajji A, and Jean-Marie V. Polymer 2001;42(19):8179-8195.

CHAPTER TWO

REAL-TIME MONITORING OF MOLECULAR ORIENTATION DURING LDPE

AND *i*-PP BLOWN FILM EXTRUSION: POLARIZED RAMAN SPECTROSCOPY

In this chapter, exploratory experiments were planned and performed to use real-time polarized Raman spectroscopy to measure molecular orientation development during blown film extrusion. Two polymers were investigated: a low-density polyethylene (LDPE) and an isotactic polypropylene (*i*-PP). Polarized and non-polarized Raman spectra, along with temperature data, were obtained at different locations along the blown film line, starting from the molten state near the die and extending upto the solidified state near the nip-rolls. The second ($\langle P_2(\cos\theta)\rangle$) and fourth ($\langle P_4(\cos\theta)\rangle$) moments of the orientation distribution function (denoted as P_2 and P_4, respectively) were quantitatively determined from the polarized scattering intensities of the band at 1130 cm^{-1}.

2.1 Experimental

2.1.1 Materials and Processing

Figure 2.1 shows a schematic of the blown film extrusion process that was used in this study. Low-density polyethylene (LDPE, Dow 640I) had a density of 0.92 g/cc

and a melt-flow index (MFI) of 1 g/10 min, whereas isotactic polypropylene (PP Dow INSPiRE 114) had a density of 0.9 g/cc and a MFI of 0.5 g/10 min. The polymers were extruded using a lab-scale 19 mm, 24:1 L/D ratio extruder (Alex James & Associates, Greenville, SC) equipped with a cross-head die (Wayne Machine Co., NJ) of 50 mm diameter, 0.64 mm gap and a single-lip air ring supplying air at a nominal velocity of 20 m/s.
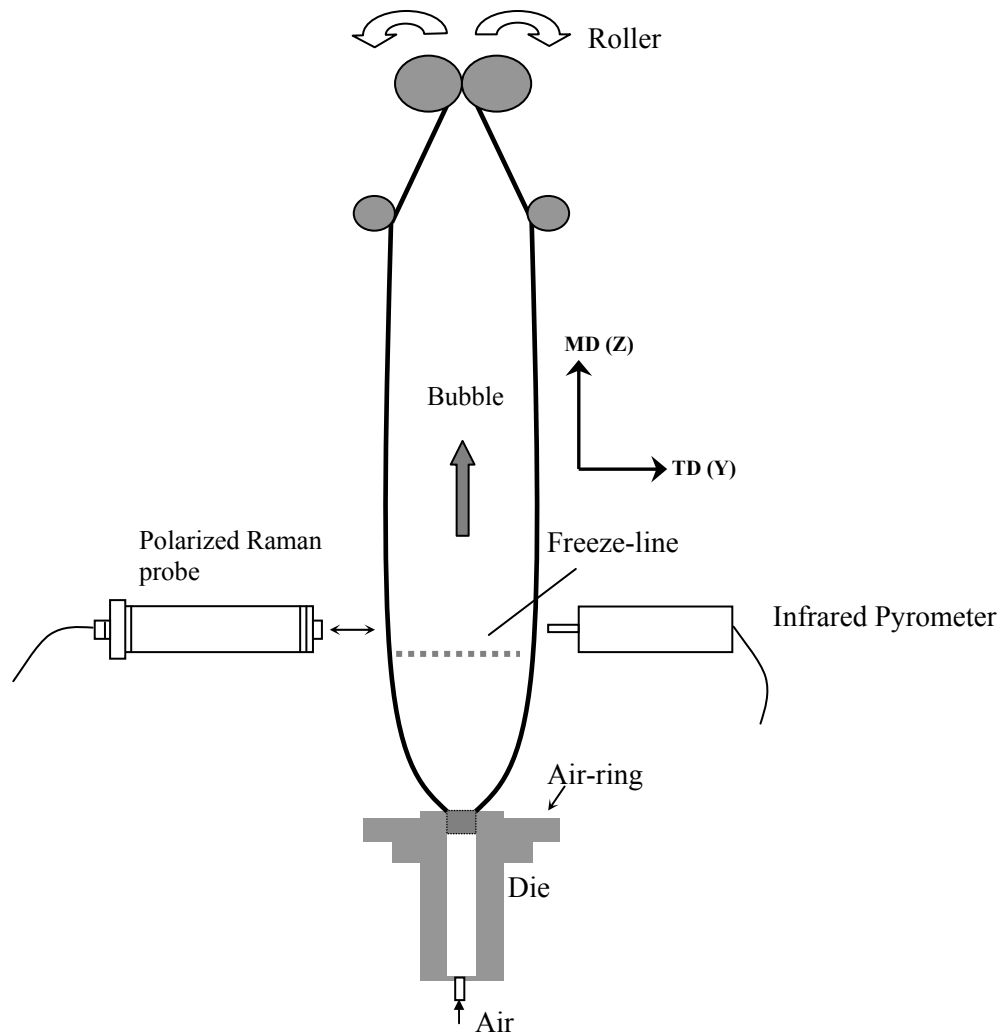
Figure 2.1 A schematic of blown film extrusion with online instruments

The die temperatures were 195°C and 230°C for LDPE and PP, respectively, and the polymer mass flow rate of approximately 36 g/min was maintained throughout the experiment. The detailed procedure for extrusion is presented in **Appendix A.**

In the most general configuration, when blown films are stretched to different extents in the machine direction (MD) and transverse direction (TD), orientation parameters in biaxial systems are not tractable using Raman spectroscopy because there are 16 unknowns but only 9 Raman intensity equations [1]. However, if the bubble is stretched primarily in one direction, a satisfactory estimate of orientation can be obtained for uniaxial symmetry with no preferred alignment of the structural units about the chain axis [2, 3]. Therefore, the bubble was extended uniaxially at a take-up ratio (TUR) of 7 and a blow-up ratio (BUR) of 0.4, which led to a thickness ratio of 0.4 for the processed film. This resulted in an essentially uniaxial extensional flow within the film and led to uniaxial symmetry of the sample (as measured by birefringence).

Real-time Raman spectroscopy consisted of a Renishaw system 100 with a near infrared 785 nm-diode laser coupled to custom-built polarized and non-polarized probes. At the maximum laser power, the polarized probes delivered approximately 5 mW of polarized radiation at the sample. The non-polarized Renishaw Raman probe delivered 10 mW near-infrared laser beam on the film through a 90 μm diameter excitation cable. The scattered Raman signal from the film was collected through a 200 μm diameter collection fiber.

The instrument was calibrated using a standard cyclohexane prior to the real-time experiments. The probes are set on a XYZ micrometer stage which can be moved axially along the film line to obtain spectra at 12 different z-positions starting from the melt and extending up to the nip rolls approximately 2m above. All spectra were obtained in back-scattering (BS) and right-angle scattering (RAS) modes over a spectral range of 900–1500 cm^{-1} with an integration time of 120 s. At least three replicate measurements were performed per location.

For the offline right-angle scattering measurements, a second polarized probe was coupled to the existing set-up at 90° to the excitation probe to act as a collection probe. **Figure 2.2** displays a schematic of the setup for back-scattering (BS) and right-angle scattering (RAS) measurements. To minimize polarization scrambling by the thick sample, the incident beam was focused close to the film edge and the scattered light was collected after passing through a thin layer of the sample. A good focus can be visually

judged when the laser sparkles on the film. The collection time was approximately 1 hr for RAS measurements and 120s for backscattering measurements. A thin aluminum foil was placed behind the film to effectively capture the Raman scattering. The experiments were conducted in a darkened environment to improve signal-to-noise ratio in the Raman spectra and to avoid saturation of the charged-couple device (CCD) detector resulting in unwanted peaks.

Data acquisition of the spectra was performed using Renishaw WiRE v 1.3 β software and GRAMS/32 software was used for data processing and analysis. Raman spectra were quantified for crystallinity values following a protocol illustrated in Chapter 1 and **Appendix B**. Real-time temperature measurements were also performed using an IRCON Infrared pyrometer (Modline 340, Niles, IL).
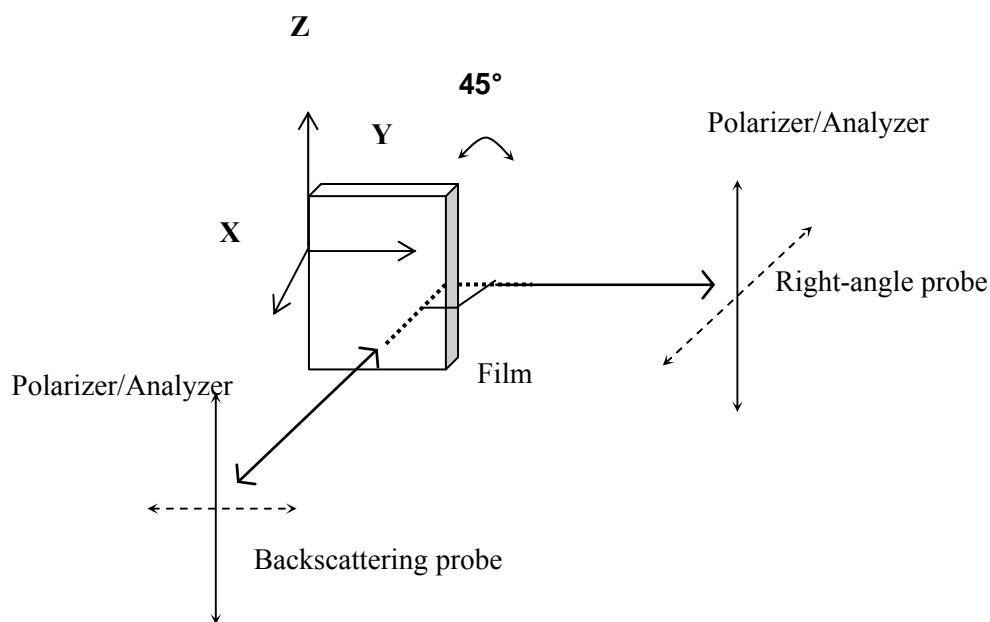
Figure 2.2 A schematic of experimental setup for backscattering and right-angle scattering measurements

Wide-angle X-ray diffraction patterns on the processed blown films were obtained

from a Rigaku 2-D diffractometer (Rigaku/ MSC) using Cu-Kα radiation with conditions

of 40 KV and 30 μA. All of the WAXD data were taken in the transmission mode. The

collected patterns were then analyzed using POLAR software to compute the Hermans'

uniaxial orientation factor (f_c = 0.5 (3$\left\langle \cos^2 \theta \right\rangle$ -1)) of the crystallographic c-axis of the

polyethylene orthorhombic unit-cell. The $\left\langle \cos^2 \theta \right\rangle$ is the average value of the cosine

squared of the angle θ between the film machine direction and the crystallographic c-axis.

Birefringence was measured using an optical microscope (BX-60F5, Olympus

Optical Co. Ltd., Japan) fitted with cross-polarizers and U-TCB Berek compensator using

the method described by Stein[4]. The detailed experimental procedures are reported in

Appendix D. In-plane (Δn_{ZY}) birefringence values indicate MD orientation with respect

to TD orientation, whereas out-of-plane (Δn_{ZX}, Δn_{YX}) birefringence values indicate MD

and TD orientation with respect to ND.

2.2 Theory and Approach

Figure 2.3 shows the system of axes *OXYZ* fixed in the sample. The laboratory

axes, X, Y and Z, represent the normal direction (ND), transverse direction (TD) and

machine direction (MD), respectively. To simplify the orientational analysis, the

structural unit, represented by a rectangular co-ordinate system (*Oxyz*) was considered to

possess orthorhombic symmetry. The structural unit is defined by the Euler angles θ, φ, and ψ as shown in **Figure 2.3**, where θ and φ are the polar and azimuthal angles, respectively. The Euler angle ψ represents rotation of the structural unit about the *Oz* axis.
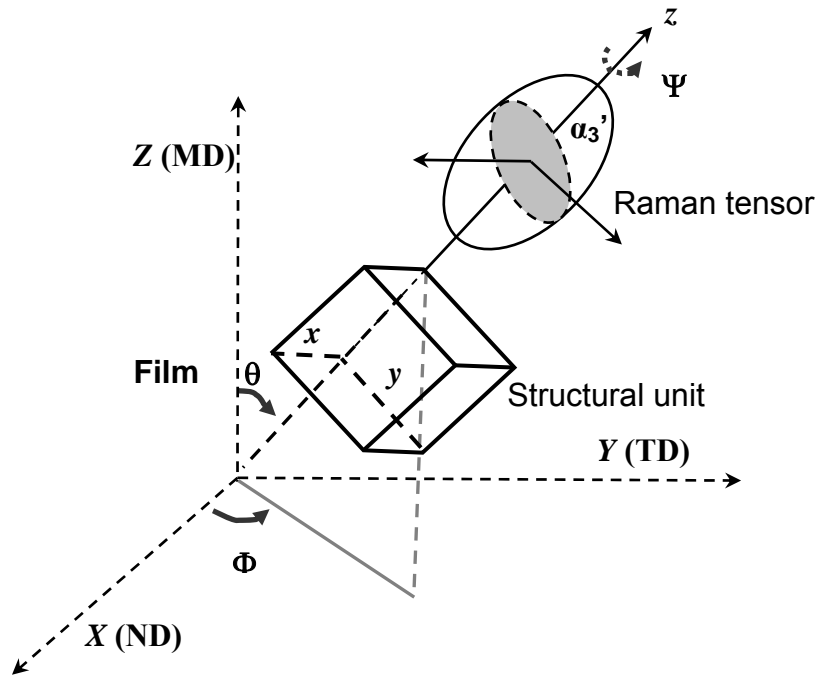
Figure 2.3 Raman tensor element coincident with the chain axis of the structural unit (*Oxyz*) (shown separately for visualization) is shown with reference to the laboratory co-ordinates O*XYZ* using Euler angles (θ,Φ,Ψ)

The scattered Raman intensity I_s is given by [1]:

$$I_s = I_o \Sigma \, (\Sigma \, l_i{}'l_j\alpha_{ij})^2,$$

where I_o is the intensity of the incident laser beam, while $l_i{}'$ and l_j are the direction cosines of the plane-polarized incident and scattered light, respectively, with reference to the laboratory axes (*OXYZ*) and α_{ij} represents the Raman tensor of the structural unit.

The expression I_s is denoted by the form $I_o \Sigma \alpha_{ij}\, \alpha_{pq}$, where $\alpha_{ij}\, \alpha_{pq}$ was expressed as linear combinations of the principal components of the Raman polarizability tensor (α_{11}, α_{22}, and α_{33}) and the Euler angles defining the orientation of the principal axes (*Oz*) of the Raman tensor with respect to *OXYZ* [2, 3, 5].

For the most general case, there are 16 unknowns ($N_o\alpha_3{}^2$, a_1, a_2 and 13 values of P_{lmn}) but only 9 equations and therefore cannot be solved.

However, if the principal axes of the tensor $[\alpha]_2$ are coincident with the axes fixed in the structural unit, the intensity equation can be simplified as:

$$I_s = I_o \Sigma \alpha_{ij}\, \alpha_{pq} = 4\pi^2 N_o \, \Sigma \, M_{lmn} A_{lmn}{}^{ijpq}$$

where, N_o is the number of structural units that contribute to the scattered Raman intensity, $A_{lmn}{}^{ijpq}$ represents the distribution of orientations of the Raman tensor and is a quadratic sum of expressions involving α_{11}, α_{22}, and α_{33} terms, while the term, M_{lmn} represents the distribution of orientations of the structural unit and contains the expansion coefficients of the orientation distribution function (ODF), $\langle P_l(\cos\theta)\rangle$.

Table 2.1 lists the simple cases when considering the four combinations of sample symmetry and symmetry of the structural which fall within the orthorhombic symmetry of the sample and unit. [1]

Table 2.1 Representation of orientation for different sample and structural symmetry

Sample	Representation	No. of Unknowns	Number of Equations
Biaxial Orientation	General Biaxial Orientation Two axes of the structural unit with respect to two axes of the specimen	P_{000}, P_{200}, P_{400}, P_{202}, P_{402}, P_{404}, P_{220}, P_{420}, P_{440}, P_{222}, P_{422}, P_{442}, P_{424}, P_{444} $N_o\alpha_3{}^2$, a_1, a_2 **(16)**	9 Equations
	Single axis of the structural unit with respect to two axes of the specimen	P_{000}, P_{200}, P_{400}, P_{202}, P_{402}, P_{404}, $N_o\alpha_3{}^2$, a_1, a_2 **(8)**	9 Equations
Uniaxial Orientation	General Uniaxial Orientation Two axes of the structural unit with respect to single axis of the specimen	P_{000}, P_{200}, P_{400}, P_{220}, P_{420}, P_{440}, $N_o\alpha_3{}^2$, a_1, a_2 **(8)**	9 Equations
	Single axis of the structural unit with respect to single axis of the specimen	P_{000}, P_{200}, P_{400}, $N_o\alpha_3{}^2$, a_1, a_2 **(5)**	5 Equations

For a uniaxial specimen [1, 3, 5], with no preferred orientation of the structural unit ($Oxyz$) about its c-axis (the structural unit is not aligned in equal probability in every direction) and the Raman tensor axes is coincident with the structural unit axes, the expression $\Sigma \alpha_{ij}\, \alpha_{pq}$ is represented as

$$\Sigma\, \alpha_{ij}\, \alpha_{pq} = 4\pi^2 N_o \Sigma_l\, M_{l00}A_{l00}{}^{ijpq}$$

$A_{l00}{}^{ijpq}$ represents the distribution of orientations of the Raman tensor and is a quadratic sum of expressions involving α_{11}, α_{22}, and α_{33} terms, while the term

$$M_{l00} = \left(\frac{1}{4\pi^2}\right)\left(\frac{2l+1}{2}\right)^{\frac{1}{2}}\langle P_l(\cos\theta)\rangle .$$ $\langle P_l(\cos\theta)\rangle$ is the lth coefficient (l=0, 2, 4, 6…) of the ODF defining the structural unit with respect to $OXYZ$.

Therefore, for a sample possessing uniaxial symmetry and the Raman tensor coincident with the c-axis of structural unit, the set of five nonlinear algebraic equations for the Raman scattering intensity are given by [2, 3, 6],

$$\mathbf{I_o\, \Sigma\, \alpha_{22}{}^2 = b\; [f_1\, (a_1,a_2)/15 + P_2 * f_2\, (a_1,a_2)/21 + 3\, P_4 * f_3\, (a_1,a_2)/280]}$$

$$\mathbf{I_o\, \Sigma\, \alpha_{33}{}^2 = b\; [f_1\, (a_1,a_2)/15 - 2P_2 * f_2\, (a_1,a_2)/21 + P_4 * f_3\, (a_1,a_2)/35]}$$

$$\mathbf{I_o\, \Sigma\, \alpha_{21}{}^2 = b\; [f_4\, (a_1,a_2)/15 - P_2 * f_5\, (a_1,a_2)/21 + P_4 * f_6\, (a_1,a_2)/280]}$$

$$\mathbf{I_o\, \Sigma\, \alpha_{32}{}^2 = b\; [f_4\, (a_1,a_2)/15 - P_2 * f_5\, (a_1,a_2)/42 - P_4 * f_6\, (a_1,a_2)/70]}$$

$$\mathbf{I_o\, \Sigma\, \alpha_{22}\alpha_{33} = b\; [f_7\, (a_1,a_2)/15 - P_2 * f_8\, (a_1,a_2)/42 + P_4 * f_9\, (a_1,a_2)/70]}$$

where b = $I_0 N_0 \alpha_{33}{}^2$, $a_1 = \alpha_{11}/\alpha_{33}$, $a_2 = \alpha_{22}/\alpha_{33}$, $P_2 = \langle P_2(\cos\theta) \rangle$, $P_4 = \langle P_4(\cos\theta) \rangle$, and $f_i(a_1, a_2)$ is a quadratic expression of a_1 and a_2.

The intensity values that were measured directly using the back-scattering (BS) geometries were $I_{ZZ}{}^{180}(0)$, $I_{YY}{}^{180}(0)$, $I_{ZY}{}^{180}(0)$, $I_{YZ}{}^{180}(0)$, $I_{ZZ}{}^{180}(45)$, $I_{YY}{}^{180}(45)$, $I_{ZY}{}^{180}(45)$, $I_{YZ}{}^{180}(45)$. The right-angle scattering (RAS) modes were $I_{YX}{}^{90}(0)$, $I_{ZZ}{}^{90}(0)$, $I_{ZX}{}^{90}(0)$ and $I_{YZ}{}^{90}(0)$, where the first and second subscripts of intensities represent the polarizer and analyzer direction, respectively. The intensity values are related to intensity expressions, $I_o\Sigma\alpha_{22}{}^2$, $I_o\Sigma\alpha_{33}{}^2$, $I_o\Sigma\alpha_{21}{}^2$, and $I_o\Sigma\alpha_{32}{}^2$, $I_o\Sigma\alpha_{22}\alpha_{33}$ [6]. The measured intensities need to be corrected for differences in focus, fluorescence, effect of polarization on the power delivered to the sample, CCD response, and fiber optic efficiency [6]. Thus, a set of 12 spectra recorded in different geometries and polarizations are needed for the calculation of the orientation parameters.

For our real-time experimental set-up, only four back-scattering Raman measurements could be recorded because RAS measurements proved to be impractical due to lateral bubble movement and hardware limitations. However, previous studies [2, 3] on HDPE have reported that if the ratios of the principal components of the Raman tensor (a_1, a_2) are known *apriori* from right-angle and back-scattering measurements, the number of unknowns are reduced to three (b, P_2, P_4) and the system reduces to three equations that can be solved from back-scattering spectra only. This method assumes that the Raman tensor does not change with crystallinity or orientation. The vibrational band at 1132 cm^{-1}, which has tensor axes coincident with the structural unit, was used to solve

intensity equations to estimate the molecular orientation parameters for polyethylene films.

2.3 Results and Discussion

2.3.1 Real-Time Crystallinity and Temperature

Figure 2.4 displays a series of Raman spectra of LDPE obtained using non-polarized Raman probe. As the polymer travels from a location below the freeze line to that above, the 1418 cm^{-1} peak intensity steadily increases as a consequence of the crystallization. As the melt is subjected to cooling, nucleation occurs followed by crystallization growth, which slows when the bubble temperature decreases to ambient. The calculated crystallinity profile based on the Strobl and Hagedorn method is presented in **Figure 2.5**. Since, there was gradual cooling of the bubble during the process, the profile shows a steep increase of crystallinity initially, immediately after the frost line height and shows a gradual increase of crystallinity at higher axial distance. Real-time temperature profile obtained using an IRCON Infrared pyrometer (Modline 340, Niles, IL) shows a plateau at ≈98°C as a consequence of the exothermic heat of crystallization.
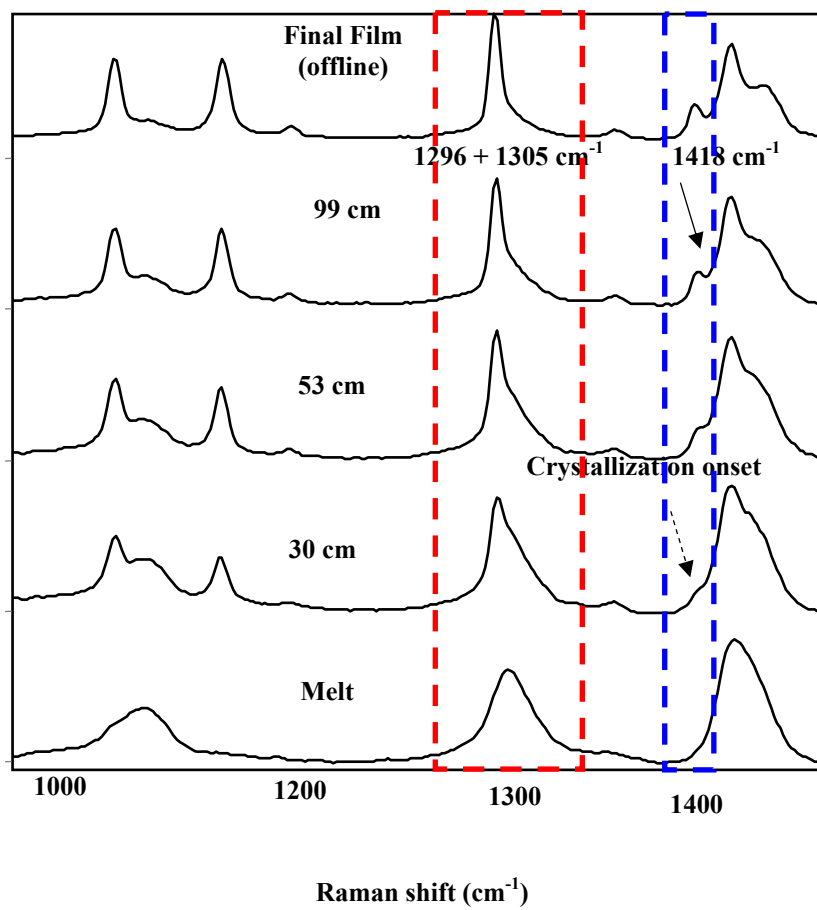
Figure 2.4 Real-time Raman spectra of LDPE at different axial locations in the film line
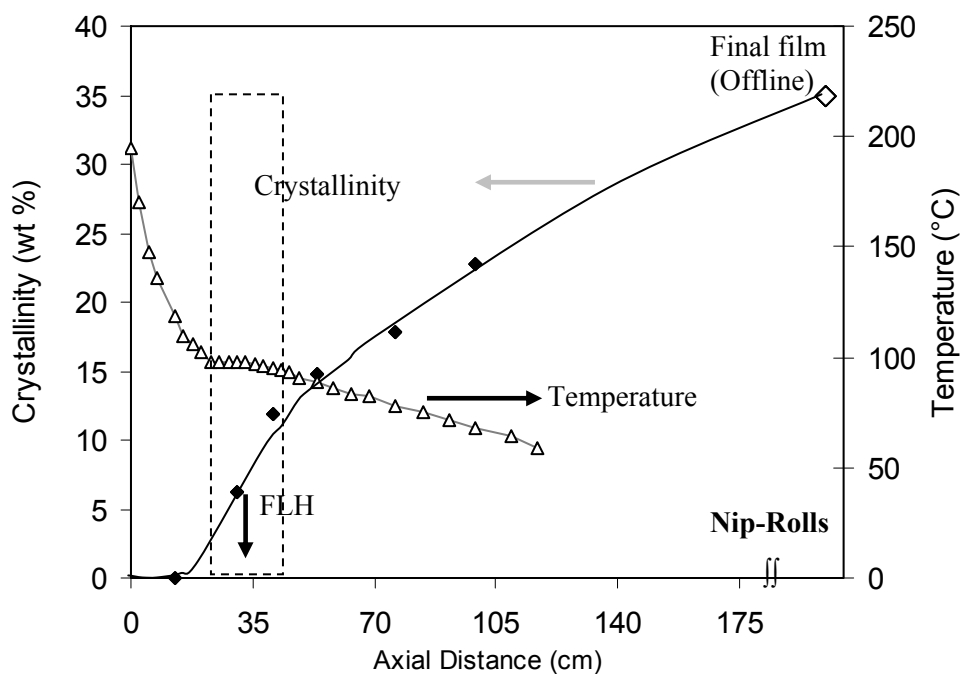
Figure 2.5 Crystallinity profile for LDPE as a function of axial distance of the blown film line. (Curves represent trends)

2.3.2 Real-Time Orientation

Figure 2.6 displays a series of polarized Raman spectra obtained at different axial locations in the film line starting from the position near the die extending up to the nip-roller. For comparison purposes, the spectra were normalized with respect to the CH_2 twisting band at 1296 cm^{-1}. In the ZZ spectra, the C-C all-*trans* conformation band at

1132 cm^{-1} increases in intensity while the 1080 cm^{-1} gauche conformation band decreases along the axial distance, indicating an increasing *trans* content with orientation in the bubble.

The differences in ZZ and YY polarized spectra indicate transformations taking place in the bubble from an isotropic to non-isotropic state during processing. **Figure 2.7** present overlaid spectra at four different locations from polarized (ZZ and YY) and non-polarized Raman probes. In the melt, as expected ZZ-, YY- polarized Raman spectra and non-polarized Raman spectrum match closely indicating the near-isotropic molten state. At higher axial distances, the C-C stretching vibration at 1132 cm^{-1} that is coincident with the chain axis (c-axis) is of interest. The I_{ZZ} (1132 cm^{-1}) intensifies as compared to I_{YY} (1132 cm^{-1}) with the evolution of orientation in the Z–direction. A similar change in depolarization ratio (I_{ZZ}/I_{YY}) of the 1132 cm^{-1} peak with increase in chain axis orientation due to deformation has been reported in previous studies by Maxfield et al.[7] on LDPE films and Thierry et al. on extruded HDPE rods [8]. The significant advantage of conducting real-time Raman spectroscopy is the ability to obtain orientation measurements starting all the way from the molten state up to the solidified state of the polymer.
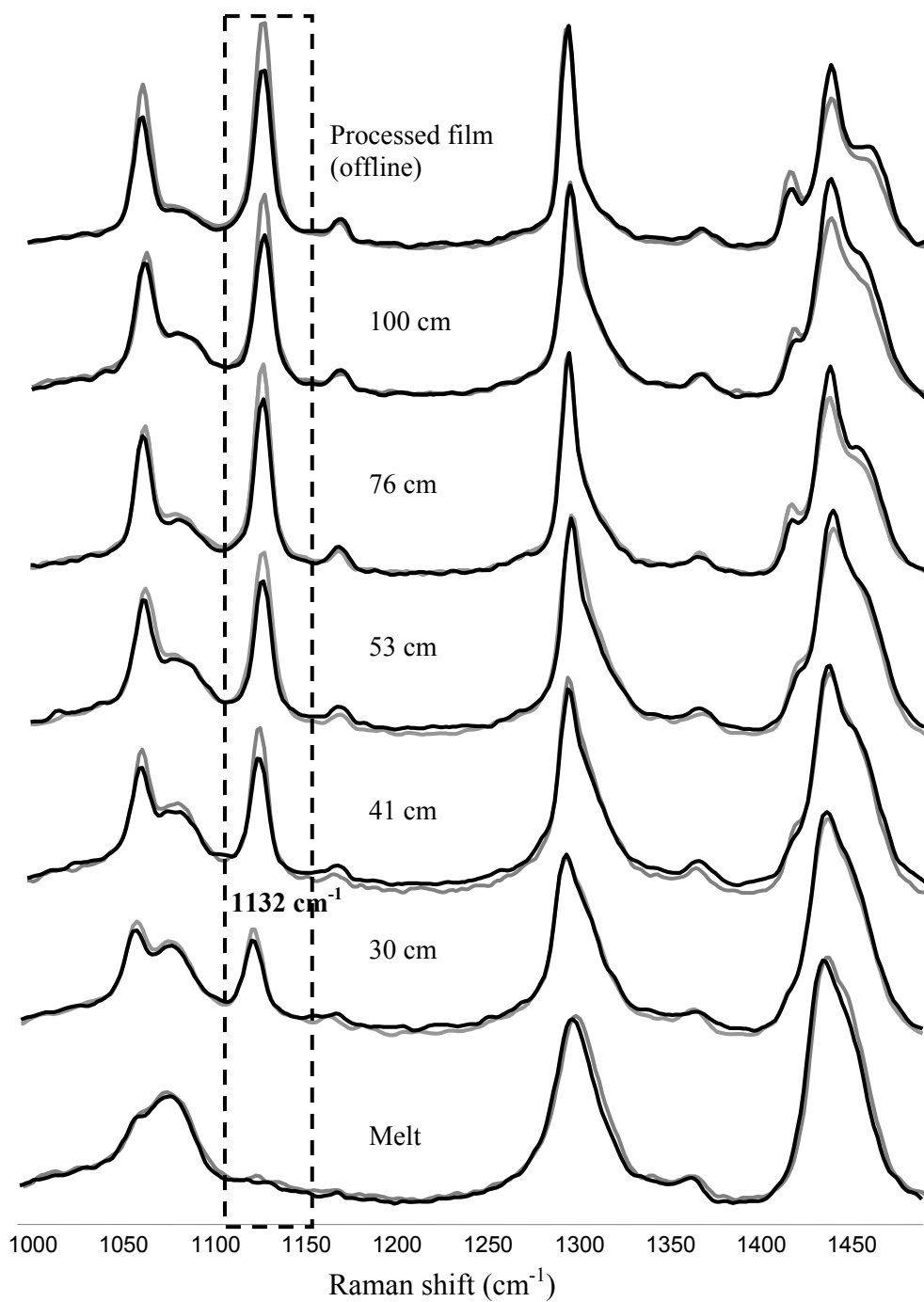
Figure 2.6 Real-time polarized Raman spectra in ZZ-direction (grey line) and YY-direction (dark line) for LDPE obtained at different axial positions along the blown film line (Spectra normalized with respect to the intensity of 1300 cm^{-1} band)
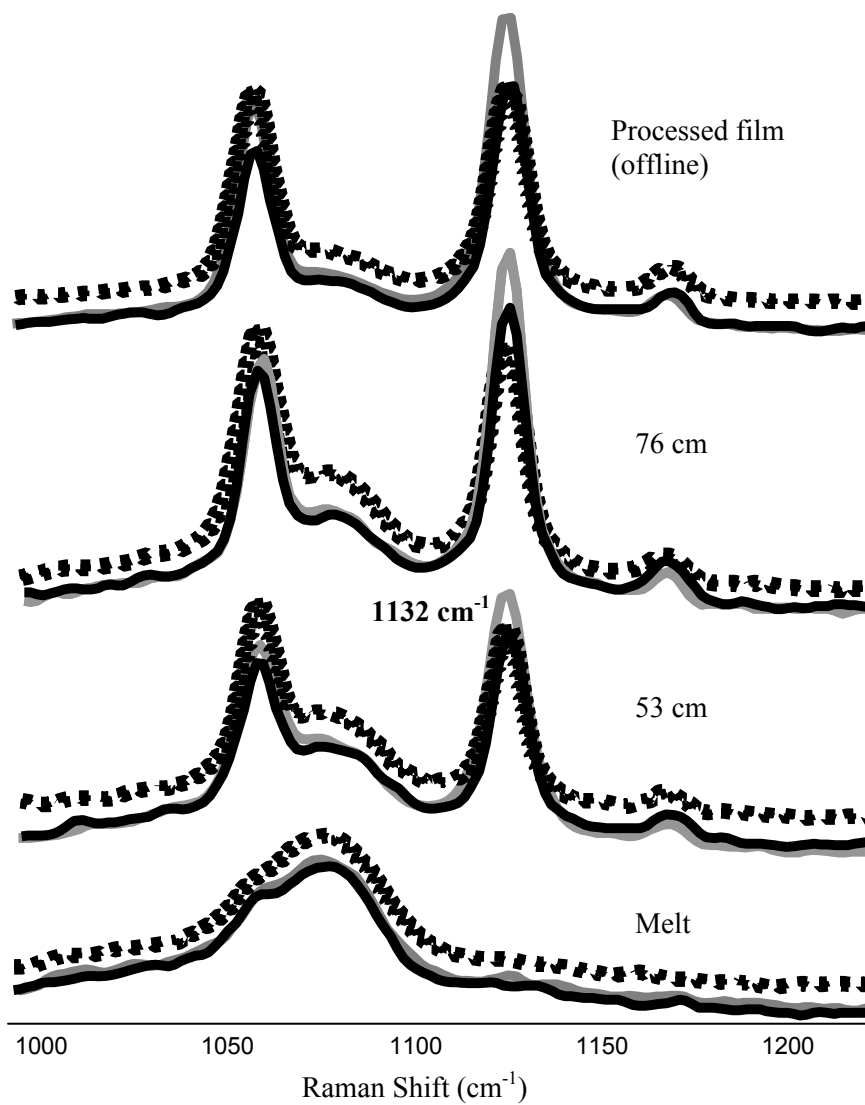
Figure 2.7 Comparison of non-polarized (dotted-line), ZZ-polarized (light-grey line) and YY-polarized (dark line) Raman spectra of PE obtained at different axial positions along the blown film line

A comparison of Raman spectra obtained from four different polarization and scattering geometries are presented in **Figure 2.8.** The intensities I_{ZY} (0) and I_{YZ} (0) for back-scattering, and I_{YZ} (0) and I_{ZX} (0) for right-angle-scattering were observed to be equivalent, which confirms the uniaxial symmetry of the specimens studied as also observed previously by Citra et al. [3] and Lesko et al. [6]. This uniaxial symmetry in the sample is further supported by birefringence values of the polyethylene film in different planes which were found to be $\Delta n_{ZY} \approx \Delta n_{ZX}$ (0.0025) and $\Delta n_{YX} \approx 0$ (0.0001). This indicates that the overall molecular orientation is preferentially in the machine direction with MD-TD plane similar to MD-ND plane but different from TD-ND plane.
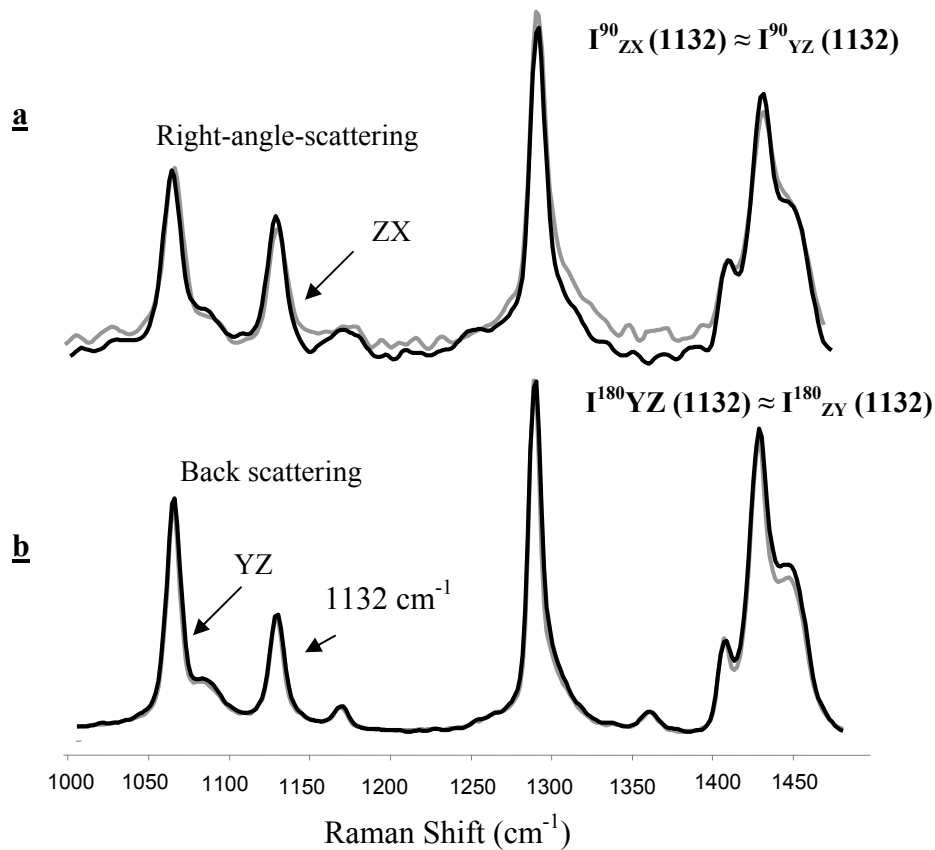
Figure 2.8 Comparison of Raman spectra obtained from two different scattering geometries: Right angle scattering (b) Back-scattering for validating uniaxial symmetry of the sample

As discussed earlier, to estimate real-time molecular orientation factors (P_2 and P_4) and principal Raman tensor components (β, a_1, a_2) along the axial distance of the film line, the simplified approach of assuming invariant Raman tensor ratios (a_1 and a_2) was used as suggested in the previous studies on polyethylene [2, 3]. The a_1 and a_2 values

determined from a set of 12 spectra on the processed blown films were used to obtain real-time P_2, P_4 and β parameters using 3 real-time back-scattering results. The estimated Raman tensor ratios (a_1 and a_2) for the 1132 cm^{-1} vibration mode of the processed films were transferred to molecular chains present in different states of the polymer during microstructural evolution.

Using the relative intensities listed in **Table 2.2**, non-linear equations (three from real-time data and five offline data) were solved using Maple$^{®}$ 9.5. The equations yield multiple solutions depending on the choice of initial conditions. Therefore, based on the understanding of the molecular structure and Raman vibration modes of the system under consideration, the restrictions for parameters: β, P_2, and P_4 were set at 0 to 100, -0.5 to 1.0, and, -0.39 to 1.0, respectively [2, 3]. The solutions that are physically unreasonable values were discarded during the calculations. Based on the 1130 cm^{-1} band, the Raman tensor ratios, a_1 (α_{11}/α_{33}) and a_2 (α_{22}/α_{33}) were -1.4 and 0.8, respectively. The sign and relative magnitude of these values are consistent with those reported in the literature [2, 3] (-0.54 for a_1 and 0.31 for a_2 for HDPE) and the difference in a_1 and a_2 values is attributed to the non-cylindrical nature of Raman tensor in polyethylene because of its planar zigzag structure.

Table 2.2. Relative Raman Intensities of 1132 cm^{-1} band for different $I_o \Sigma \alpha_{ij} \alpha_{pq}$

Axial dist. (cm)	$I_o \Sigma \alpha_{33}^2$	$I_o \Sigma \alpha_{22}^2$	$I_o \Sigma \alpha_{32}^2$	$I_o \Sigma \alpha_{21}^2$	$I_o \Sigma \alpha_{22} \alpha_{33}$
13.0	–	–	–	–	–
40.0	1.000	0.962	0.653	–	–
50.0	1.000	0.910	0.482	–	–
100.0	1.000	0.860	0.378	–	–
Final Film	1.000	0.861	0.365	0.704	-0.358

From the real-time back-scattering intensity data at different locations, the molecular orientation factors P_2 and P_4 were obtained, and are presented in **Figure 2.9**. The figure shows that the orientation factor P_2 are close to zero near the frost-line height (FLH), increase steadily with the axial distance, and then plateau near the nip rolls. The P_2 values calculated near the nip rolls are comparable with those calculated from offline Raman measurements on the processed blown films. The large initial increase in orientation factor P_2 during crystallization can be attributed to oriented nucleation and crystallization growth processes. This is supported by the online temperature profile, which is superimposed on the orientation profile. We note that some orientation also takes place even as the temperature plateaus. Thus, even after the bubble shape is locked into place, reorganization of the chain orientation continues in the stretching direction. A similar trend for overall molecular orientation as a function of axial distance was observed in birefringence studies [9, 10], which reported that the overall molecular orientation is significantly influenced by the crystallization process.
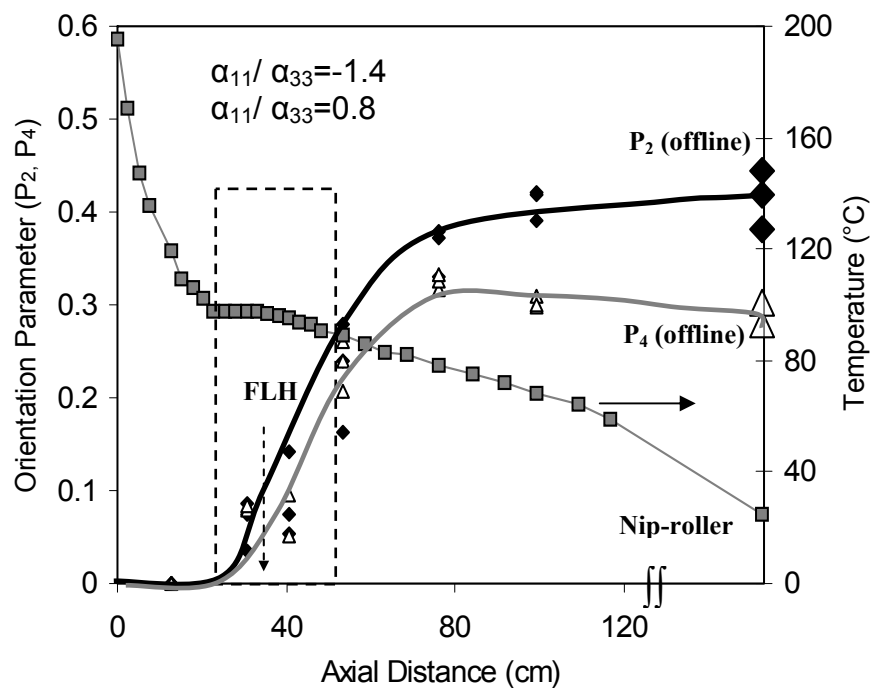
Figure 2.9 Real-time molecular orientation parameters: P_2 (diamond) and P_4 (triangle) from Raman spectroscopy as function of axial distance (lines represents the trends). The large symbols are values from offline Raman measurements on the processed films. The online temperature profile is superposed with real-time orientation data (solid curves represent trends).

Figure 2.9 also presents P_4 values, which represent the width of the orientation distribution function [5, 11]. These values were found to increase initially but stay constant higher up in the film line. The increase in the P_4 value along with that of P_2 may indicate the contribution from oriented amorphous chains during the phase transformation, since all-*trans* C-C band has contribution from crystalline and amorphous regions. The increase may also be caused by counteracting effects of orientation and relaxation of the molecular chains. The values for P_4 fall within the range of the most probable ones estimated by Bower [5]: $35P_2^2 -10P_2 -7)/18 \leq P_4 \leq (5P_2+7)/12$.

Next, **Figure 2.10** displays the change of molecular orientation with crystallinity. Initially the orientation increases significantly with crystallinity, but plateaus as the equilibrium crystallinity values are approached. This result can be explained on the basis of Keller's theory [12] according to which the non-isothermal crystallization process acts in consolidating the molecular chain orientation that is caused by the applied stresses.
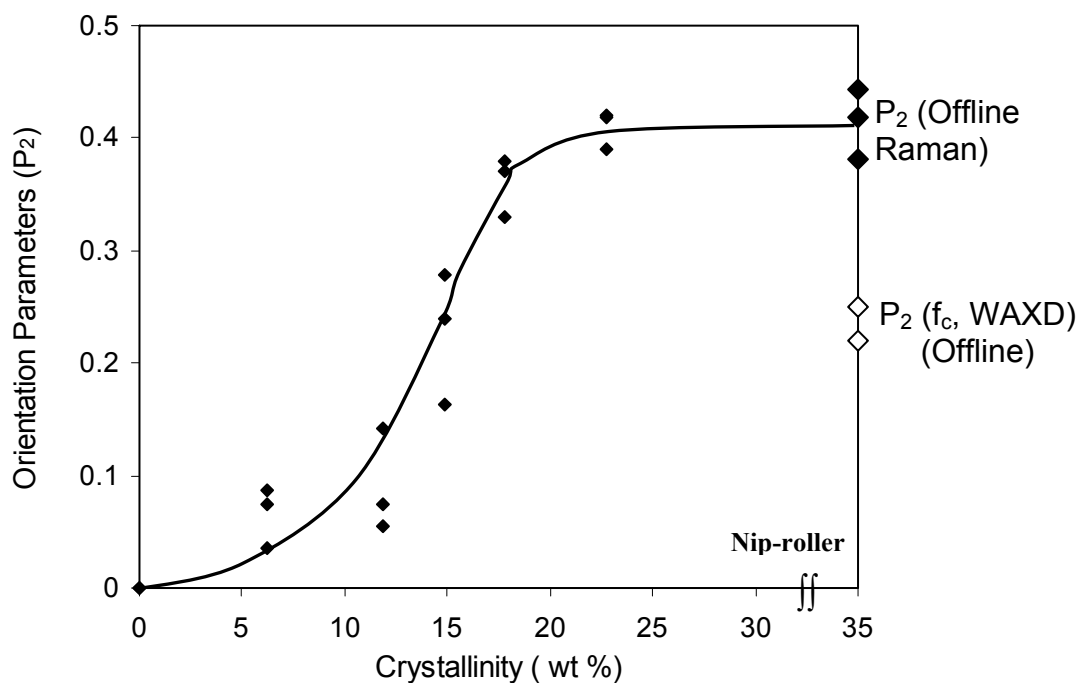
Figure 2.10 Molecular orientation parameter, P_2, plotted as a function of absolute crystallinity at corresponding axial positions in the blown film line (solid curve represents trend)

The Herman's orientation factor (f_c) for the final solidified films were obtained from offline WAXD measurements, and are shown in **Figure 2.10** for comparison. These f_c values were smaller than those obtained from Raman measurements. The difference in these values may arise not only from the sensitivity of the Raman measurements to polarization scrambling (multiple reflections and refractions), sample geometry

(thickness, translucency), instrumental factors (objective lens) [2, 6, 13] but also from different interactions that the incident radiations (X-rays vs. laser beam) have with the crystalline phase, which itself possess a range of perfection. Such quantitative differences in orientation values from spectroscopic (FTIR) and X-ray diffraction measurements have also been reported in a recent literature study [14].

A reasonable estimate of the molecular orientation in LDPE can also be obtained from the ZZ backscattered Raman spectrum. Pigeon et al. [2] reported an increase in intensity ratio I_{1132}/I_{1064} with the increase in orientation factors P_2 and P_4. Also, Lu and coworkers[15] concluded that an increase in modulus of high density linear polyethylene is associated with an increase in intensity ratio I_{1132}/I_{1064}. The symmetrical C-C stretching band at 1132 cm^{-1} have $A_g + B_{1g}$ symmetry mode which intensifies parallel to the stretching direction (ZZ) [3], while the asymmetrical C-C stretching band at 1064 cm^{-1} have $B_{2g} + B_{3g}$ symmetry mode that intensifies only for cross-polarization (ZY). As presented in **Figure 2.11**, the integral intensity ratio I_{1132}/I_{1064} from backscattered ZZ polarized spectra was found to increase with the axial distance indicating an increase in chain axis orientation in the machine direction. The trend is consistent with that observed in **Figure 2.9**.
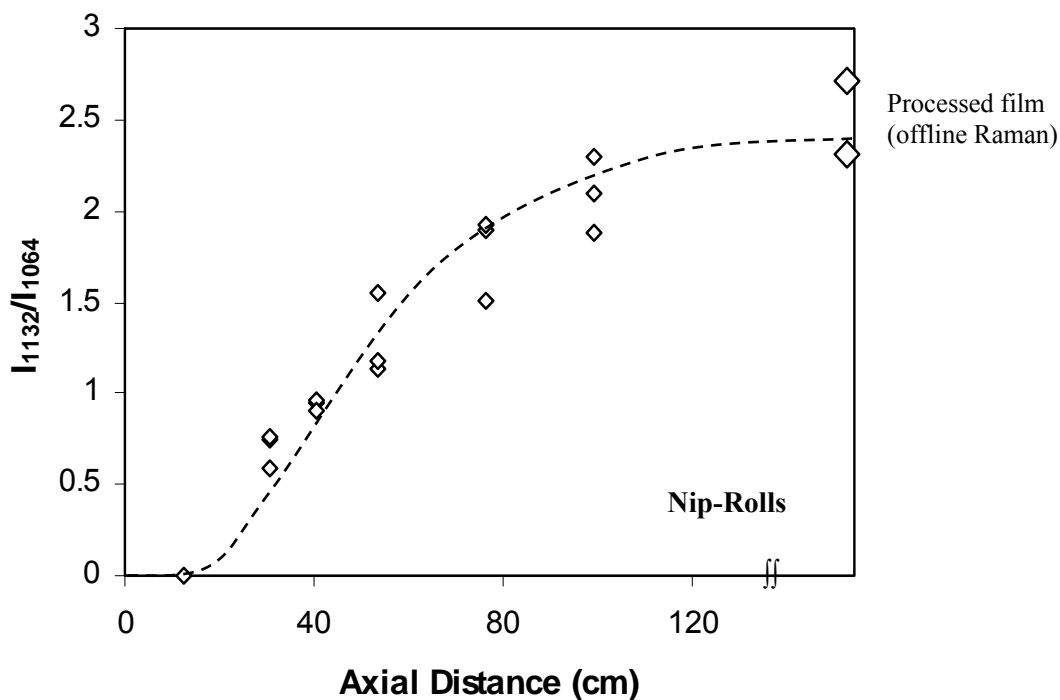
Figure 2.11 Integral intensity ratio I_{1132}/I_{1064} from backscattered ZZ polarized

spectra as a function of axial distance (dotted curve represents the trend)

Real-time polarized Raman spectroscopy was also conducted during blown film

extrusion of polypropylene. A semi-quantitative estimate of molecular orientation was

obtained. **Figure 2.12** shows a series of ZZ and YY polarized Raman spectra for PP

along the film line. The relative intensities of 809 cm^{-1} and 841 cm^{-1} have been reported
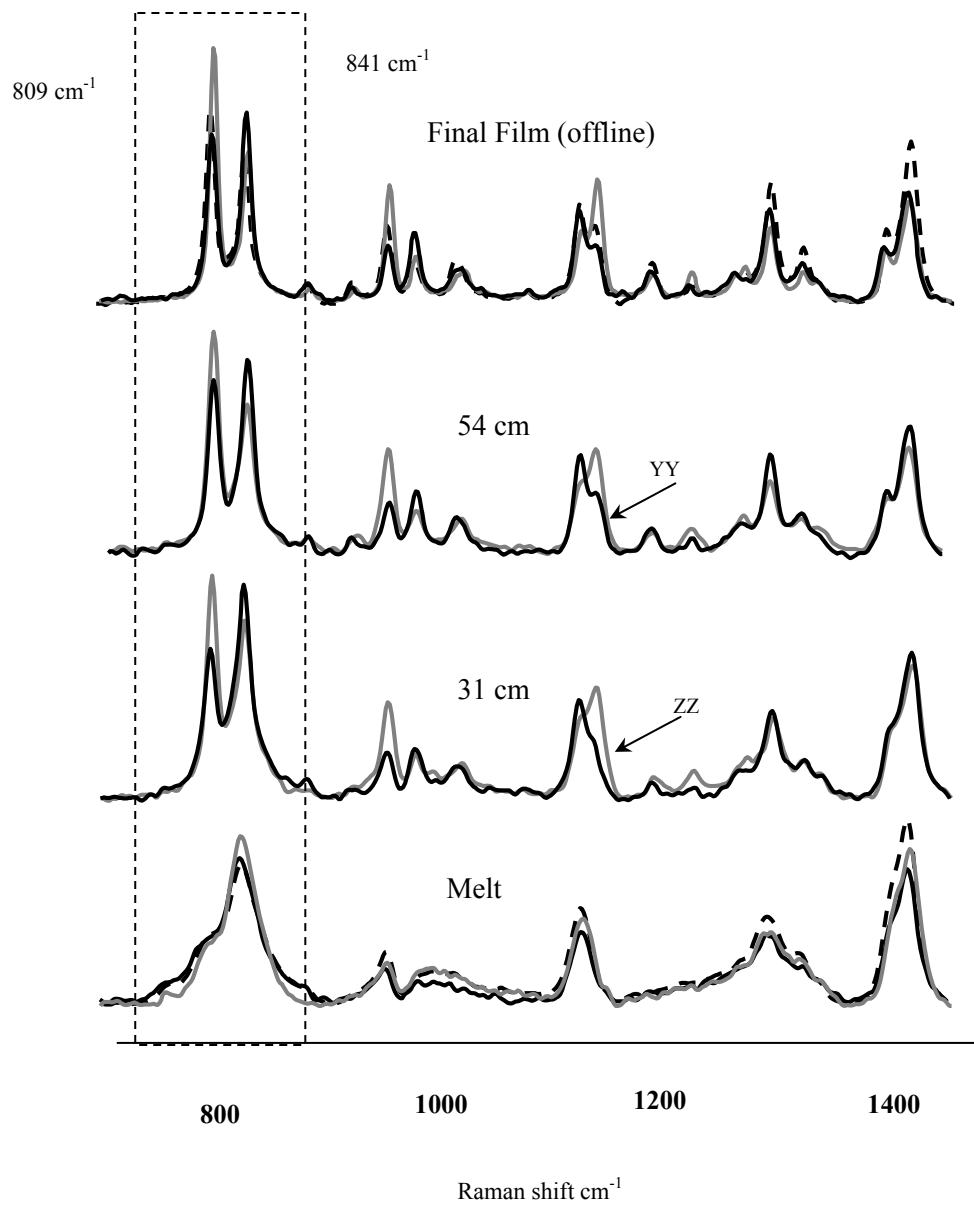
Figure 2.12 ZZ (grey line) and YY (dark line) polarized Raman spectra of PP obtained online at different positions in the film line. (The unpolarized Raman spectrum of PP is shown by dotted line for the melt state)

to change with an increase in the chain-axis orientation in the machine direction [16]. As can be noted from the spectra, in the melt, the 809 cm^{-1} band is absent or weak indicating the random orientation of the chain axis in the amorphous melt. The differences in ZZ and YY polarized spectra indicate transformations taking place in the bubble from an isotropic to non-isotropic state during processing. The rocking vibrations at 809 cm^{-1} and 841 cm^{-1} that are coincident with the chain axis (c-axis) is of interest here. In the melt, as expected, the peaks in ZZ and YY polarized Raman spectra match closely with the peaks in unpolarized Raman spectra (dotted line), indicating the near-isotropic molten state. However, at higher axial distances along the film line, the I_{ZZ} (809/841) intensifies as compared to I_{YY} (809/841) with the evolution of molecular chain orientation in the Z–direction. **Figure 2.13** presents the change in intensity ratio I_{ZZ} (809/841) from the backscattered ZZ polarized spectra indicating an increase in chain axis orientation due to an extensional flow field. The increase is consistent with previous studies [16] reported in the literature.
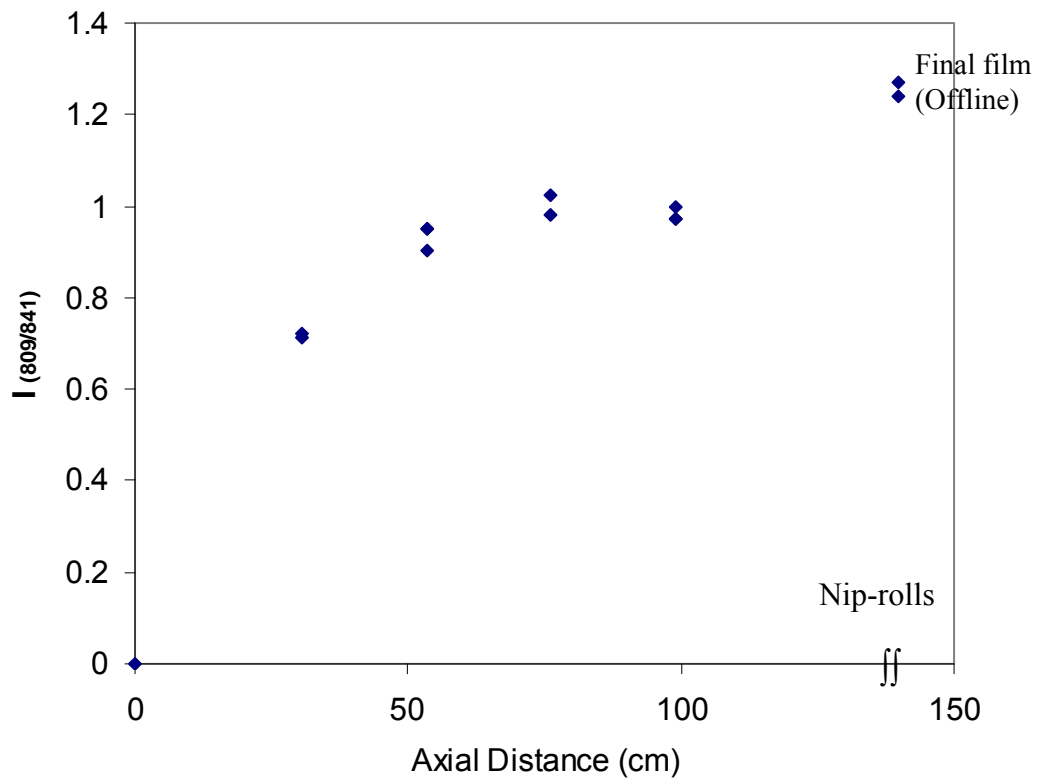
Figure 2.13 Raman intensity ratio I_{ZZ} (809/841) for polypropylene as

a function of axial distance in the film line

2.4 Conclusions

Real-time polarized Raman spectroscopy was successfully performed during single-layer blown film extrusion of LDPE and PP for certain combinations of experimental conditions. Quantitative estimate of molecular orientation of LDPE are presented for the first time. The experimental difficulties involved in the measurements were overcome by using the invariance of Raman tensor components during phase transformation and conducting measurements on the bubble subjected to uniaxial extension. As expected, the orientation parameters, P_2 and P_4, increased with the crystalline development. The difference in P_2 values measured from Raman measurements and WAXD techniques is noted. The increase in molecular orientation parameters (P_2 & P_4) even after the bubble shape is locked into place (at the frost-line height) indicates that reorganization of the chain orientation continues far above the frost line height during the process.

2.5 References

1. Bower DI. J Polym Sci Pol Phys Ed 1972;10:2135-2153.

2. Pigeon M, Prudhomme RE, and Pezolet M. Macromolecules 1991;24(20):5687-5694.

3. Citra MJ, Chase DB, Ikeda RM, and Gardner KH. Macromolecules 1995;28(11):4007 4012.

4. Stein RS. Journal of Polymer Science 1957;24.

5. Bower DI. Journal of Polymer Science Part B-Polymer Physics 1981;19(1):93-107.

6. Lesko CCC, Rabolt JF, Ikeda RM, Chase B, and Kennedy A. Journal of Molecular Structure 2000;521:127-136.

7. Maxfield J, Stein RS, and Chen MC. Journal of Polymer Science Part B-Polymer Physics 1978;16(1):37-48.

8. Lefevre T, Rousseau ME, and Pezolet M. Applied Spectroscopy 2006;60(8):841-846.

9. GhanehFard A, Carreau PJ, and Lafleur PG. International Polymer Processing 1997;12(2):136-146.

10. Ito H, Suzuki KI, Kikutani T, KANG HJ, and Kanai T. Proceedings of society of plastics engineers, vol. 50: Society of Plastics Engineers, 2004.

11. Frisk S, Ikeda RM, Chase DB, Kennedy A, and Rabolt JF. Macromolecules 2004;37(16):6027-6036.

12. Keller A and Kolnaar JWH. Orientational Phenomena in Polymers: Springer Berlin / Heidelberg, 1993.

13. Tanaka M and Young RJ. Journal of Materials Science 2006;41(3):963-991.

14. Ajji A, Zhang X, and Elkoun S. Polymer 2005;46(11):3838-3846.

15. Lu S, Russell AE, and Hendra PJ. Journal of Materials Science 1998;33(19):4721-4725.

16. Paradkar RP, Sakhalkar SS, He XJ, and Ellison MS. Applied Spectroscopy 2001;55(5):534-539.

CHAPTER THREE

REAL-TIME WIDE-ANGLE X-RAY DIFFRACTION DURING POLYETHYLENE

BLOWN FILM EXTRUSION

In this chapter, real-time wide-angle X-ray diffraction (WAXD) measurements during blown film extrusion of low-density polyethylene (LDPE) are reported. WAXD patterns were obtained at different axial positions in the blown film line starting from a location near the die and extending up to the nip-roller. The X-ray diffraction patterns from the bubble were analyzed for crystalline growth along the bubble. Simultaneous real-time Raman spectroscopy was also conducted to compare crystallinity values obtained from these two different techniques.

3.1 Experimental

3.1.1. *Materials and Processing*

Low-density polyethylene (LDPE, Dow 640I, 0.92 g/cc) with a melt-flow index (MFI) of 1 g/10 min was processed into blown films using a lab-scale extruder (19 mm, 24:1 L/D, Alex James & Associates, Greenville, SC) equipped with a die of 25.4 mm diameter and 0.25 mm gap (Haake Inc, AZ). A die temperature of 210°C and a throughput of 20 g/min were maintained during the experiment. The films were

processed using a single-lip air ring adjusted to supply air at a velocity of 12 m/s as measured with an air velocity transducer (TSI model 8455, St. Paul, MN). Of the various combinations of processing parameters, a blow-up ratio (BUR) of 0.6 and a take-up ratio (TUR) of 5.5 were chosen for the real-time measurements based on the stability of the bubble. In addition, control blown film samples were also formed, one with a diameter of 2.2 cm (small) and another with a diameter of 8 cm (large), for offline X-ray diffraction experiments.

3.1.2. *Real-time Measurements*

A custom-built X-ray diffraction system (Rigaku/ MSC) shown in **Figure 3.1** was used throughout this study. It consisted of X-ray generator, beam-collimator, and image-plate detector stationed on a motor-driven Z-platform. The platform can be moved axially from a distance of one meter up to a distance of 5 meters above the ground with a resolution of 1 mm. During the experiment, the extruder with the blown film die was raised above the ground using a bench and the take-up roller was stationed at a position more than 5 meters from the ground, so that it did not interfere with the online X-ray diffraction system.

Wide-angle X-ray diffraction patterns were obtained from a Rigaku 2-D diffractometer (Rigaku/ MSC) using Cu-Kα radiation with conditions of 45 KV and 0.67 mA. The incident X-ray beam was collimated to a beam size of 0.5 mm diameter and was focused on the bubble surface using a video-camera arrangement. An image plate
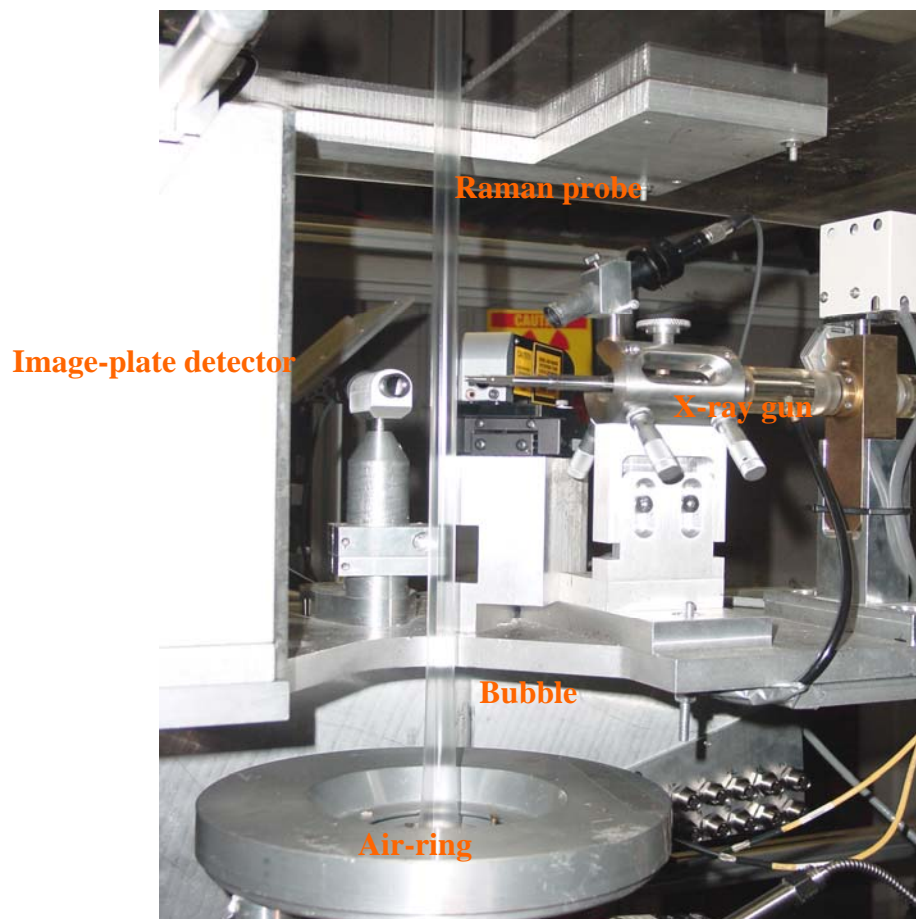
Figure 3.1 Photographic image of blown film extrusion with online X-ray diffraction system and Raman spectroscopic probes

(Fujifilm, BAS-IP MS2325) was used to collect the diffracted X-rays from the sample. A Mitsubishi RV-E2 robot with a CR-E116 controller interfaced with the computer enable automatic control of exposure, scanning, erasing and reloading of the image plate during the experiment. All of the WAXD data were obtained in transmission mode with an exposure time of 30 min and two repetitions. During the experiment, the lateral movement of the bubble was constrained so that it was stable and the X-ray beam was focused on the longitudinal axis of the bubble. The patterns collected at different axial distances during the film blowing were corrected for air-scattering background using POLAR software (STAR Inc., SUNY, NY) and analyzed using GRAMS/32 software (Galactic Inc., Salem, N.H).

Further, in order to compare the real-time X-ray diffraction results with those obtained by a different technique, simultaneous real-time Raman spectroscopic measurements were conducted following the procedure presented in Chapter 1. The online Raman spectroscopy system consisted of Raman probe connected to a charged-coupled device (CCD) detector (Renishaw Raman system 100, Gloucestershire, UK). The adjustable platform for X-ray diffraction measurements also holds other instruments such as the Raman spectroscopic probes and the infrared pyrometer as shown in **Figure 3.1**

3.2. Results and Discussion

3.2.1. *Offline Measurements*

Prior to online X-ray diffraction measurements, offline control studies were conducted on the processed blown films to explore the nature of the X-ray diffraction pattern for different geometries of the film. **Figure 3.2** shows a schematic of three different methods for obtaining an X-ray diffraction pattern on a blown film: (a) Transmittance of X-ray beam through a lay-flat blown film; (b) Grazing incidence of X-ray beam on a hollow cylindrical blown film (simulating the film bubble); and (c) Transmittance of X-ray beam through the hollow cylindrical blown film, where the beam is transmitted through the front-face (the face immediately encountered by the X-ray beam) and the back-face (the face encountered by the X-ray beam before reaching the image-plate detector) with air between them.
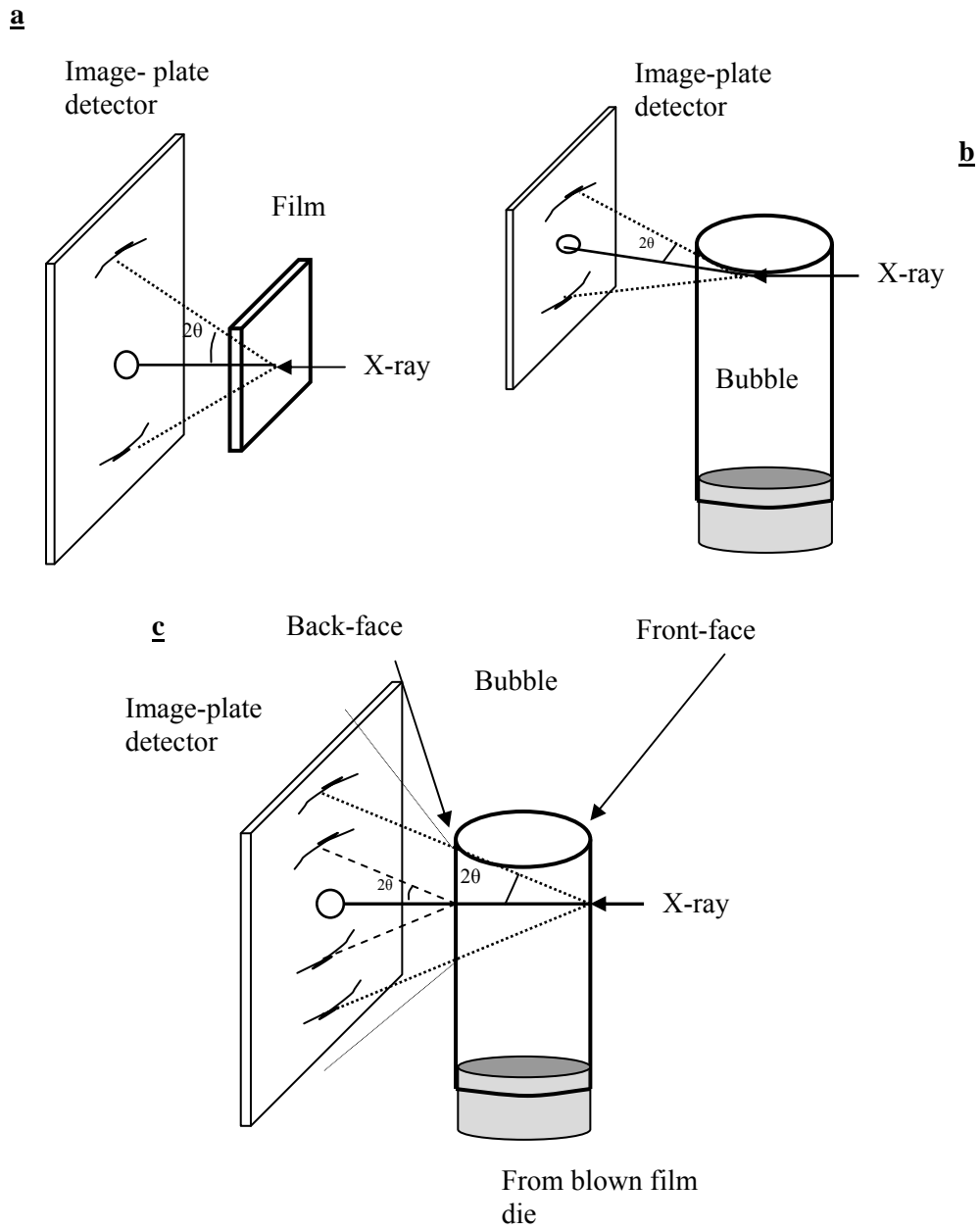
Figure 3.2. Generation of X-ray patterns in blown film: (a) Lay-flat blown film; (b) Grazing incidence X-ray diffraction on a hollow cylindrical blown film; and (c) Transmittance of X-ray beam through the hollow cylindrical blown film.

The normalized 2θ (theta) intensity spectra obtained from the diffraction pattern for a grazing-incidence on a hollow cylindrical blown film and a lay-flat film (flattened after grazing-incidence experiment) are presented in **Figure 3.3**. The prominent crystallographic planes of interest in polyethylene are the (110) and (200) peaks at diffraction angles of 21.6° and 23.8°, respectively, and are used to calculate the orthorhombic crystalline content[1]. The WAXD intensity spectrum obtained from the grazing incidence of an X-ray beam on the hollow cylindrical geometry is not different from the spectrum obtained for the lay-flat film. However, the use of grazing incidence X-ray diffraction during the real-time measurements is impractical because of the lateral movement of the bubble during continuous processing.
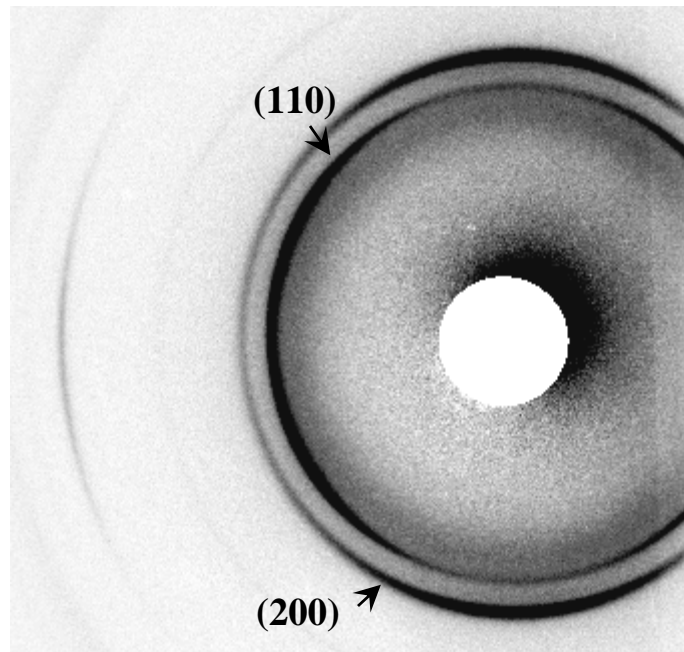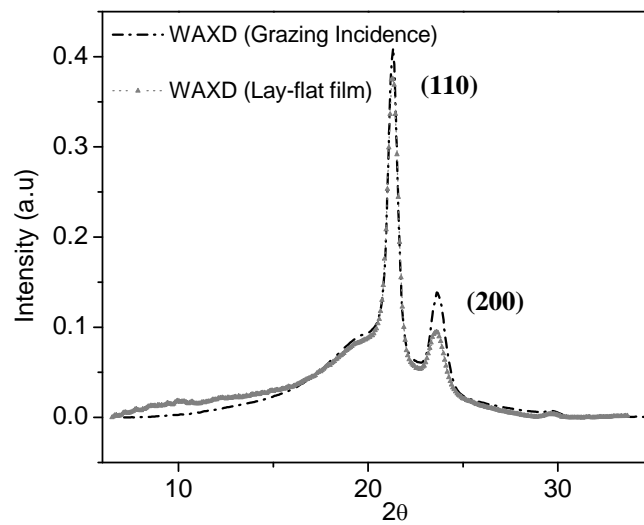
Figure 3.3. (a) X-ray diffraction pattern a lay-flat LDPE blown film, and (b) Comparison of normalized intensity spectrum from WAXD obtained on a lay-flat LDPE blown film (grey dotted line) and grazing incidence X-ray diffraction on a cylindrical blown film (black dotted line) with planes of interest.

Figure 3.4 presents the X-ray diffraction pattern along with the 2θ spectrum generated by the transmittance of the X-ray beam through the cylindrical blown film. A composite diffraction pattern is formed on the image-plate detector that consists of the response from the front and back faces, at a high and low angle, respectively, caused by the differences in distance between a given face and the image-plate detector. The spectrum obtained using the lay-flat film is overlaid with the spectrum from the cylindrical blown film for comparison. As expected, the intensity of diffracted X-ray beam was slightly lower for the front-face compared to that of the back-face. This is attributed to scattering of diffracted X-ray beam by the back-face in its path from the front-face to the image-plate detector. However, the secondary scattering of the scattered X-ray from the front-face was not detected because it is expected at an angle that is beyond the range of the image-plate detector.
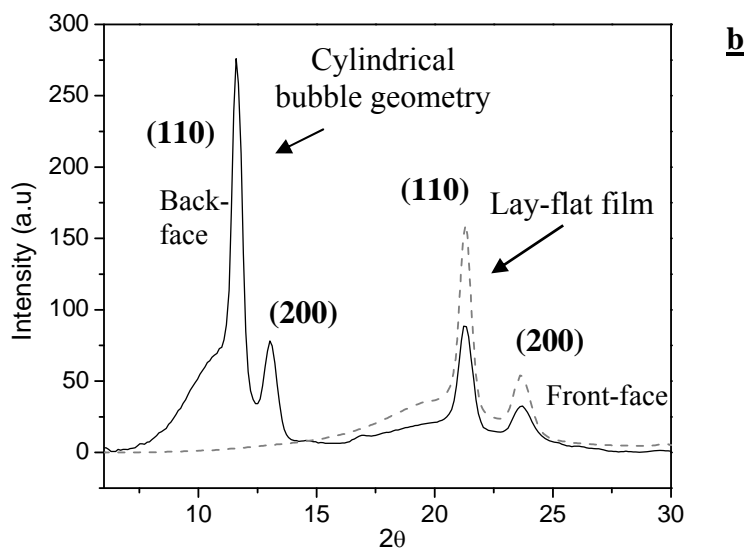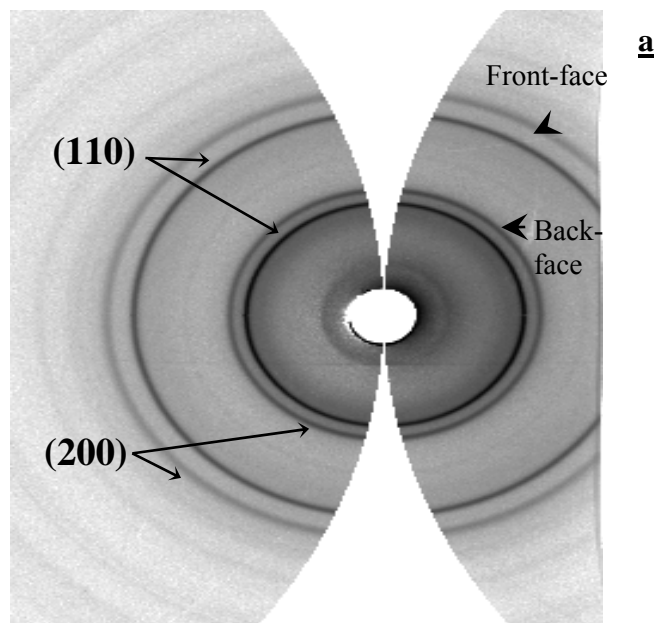
Figure 3.4. (a) X-ray diffraction pattern obtained by transmittance of X-ray beam through a hollow cylindrical blown film, (b) Intensity spectrum from WAXD pattern of a hollow cylindrical blown film (solid) and lay-flat film (dotted)

With the appropriate choice of the face-to-detector distance, the spectrum from a given face of the cylindrical blown film can be matched with its spectrum from the lay-flat geometry. For the X-ray system used in this study, the sample-to-detector distance was 11.3 cm. The hollow cylindrical blown film, 2.2 cm diameter, was mounted such that the front face was at a sample-to-detector distance of 11.3 cm. **Figure 3.5** presents a comparison of the X-ray spectrum obtained on the lay-flat film to the spectrum obtained on the hollow cylindrical film. The known sample-to-detector distance of 11.3 cm leads to a match of the diffraction peaks from the front-face (**Figure 3.5b**) to the diffraction peaks from the lay-flat film (**Figure 3.5a**). On the other hand, a sample-to-detector distance of 9.1 cm, calculated from the diameter (2.2 cm) of the cylindrical blown film, leads to a match between the diffraction peaks from the back-face (**Figure 3.5c**) and the peaks from the lay-flat film.
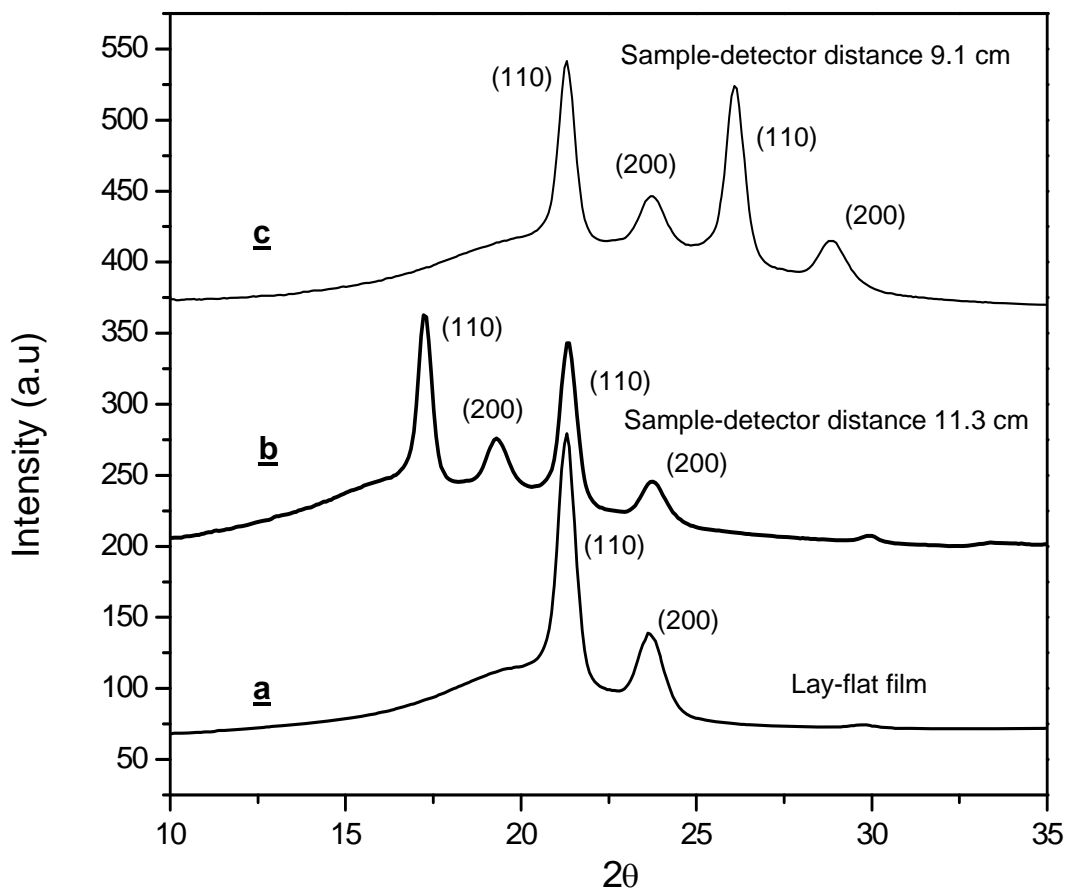
Figure 3.5 2θ-Intensity spectra from a) Lay-flat film, b) Front-face, (11.3 cm), and c) Back face (9.1 cm) of a hollow cylindrical blown film (2.2 cm diameter). The peaks from the hollow cylindrical film matched with the peaks from a lay-flat film based on appropriate face-to-detector distance.

3.2.2. *Online X-ray diffraction measurements*

Two-dimensional WAXD images for LDPE bubble obtained at various axial distances along the line are presented in **Figure 3.6**. The pattern formed on the image-plate is a composite pattern due to scattering from front and back faces of the bubble. Since the bubble diameter during the experiment was smaller compared to the controlled samples for the processing condition studied, the (200) peak of the front-face of the bubble overlaps the (110) peak of the back-face of the bubble.

Below the frost-line height (i.e., axial distance <50 cm), the WAXD pattern exhibit an isotropic amorphous halo as expected for the melt state of the polymer. At a distance of 51 cm, close to the FLH, the crystalline (110) and (200) reflections start to appear in the pattern, indicating the onset of crystallization. At higher axial distances (>76 cm), the crystalline reflections become stronger, indicating an increase in the crystal population. The patterns also show the existence of preferred orientation of the crystalline structure in the bubble. The (110) reflections intensifies in the equatorial direction, and the (200) reflections appears on the meridian. Simultaneously, the amorphous halo decreases.
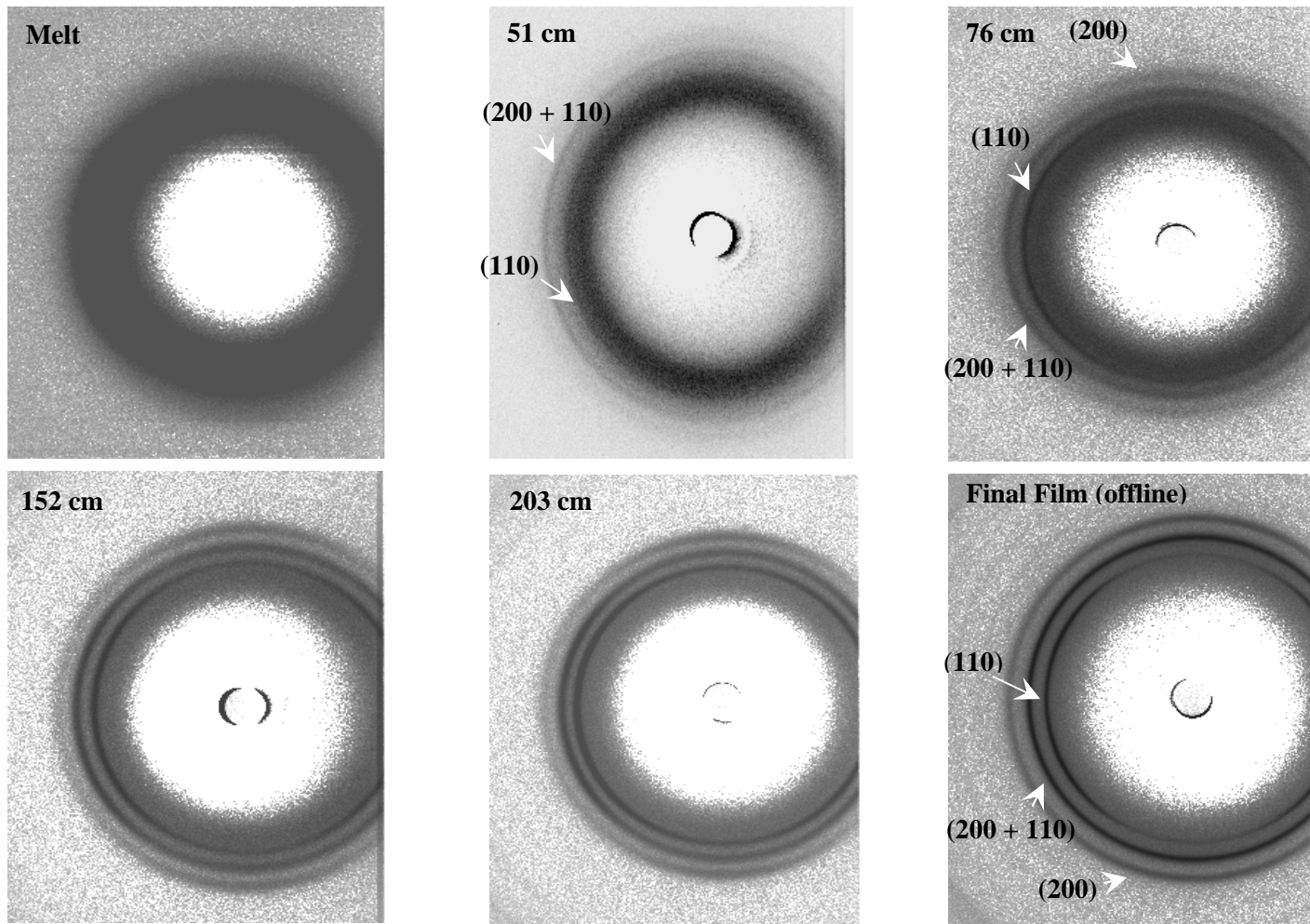
Figure 3.6. WAXD Patterns at different axial positions along the film line starting from the melt to processed final film

The 2θ intensity spectra from the WAXD patterns obtained at various axial locations in the blown film line are presented in **Figure 3.7**. As expected, the WAXD spectrum for the melt exhibits a diffuse amorphous halo and lacks any defined peaks. As the polymer travels past the freeze line, the (110) and (200) crystalline peaks increase in intensity at the expense of the amorphous halo due to crystallization.
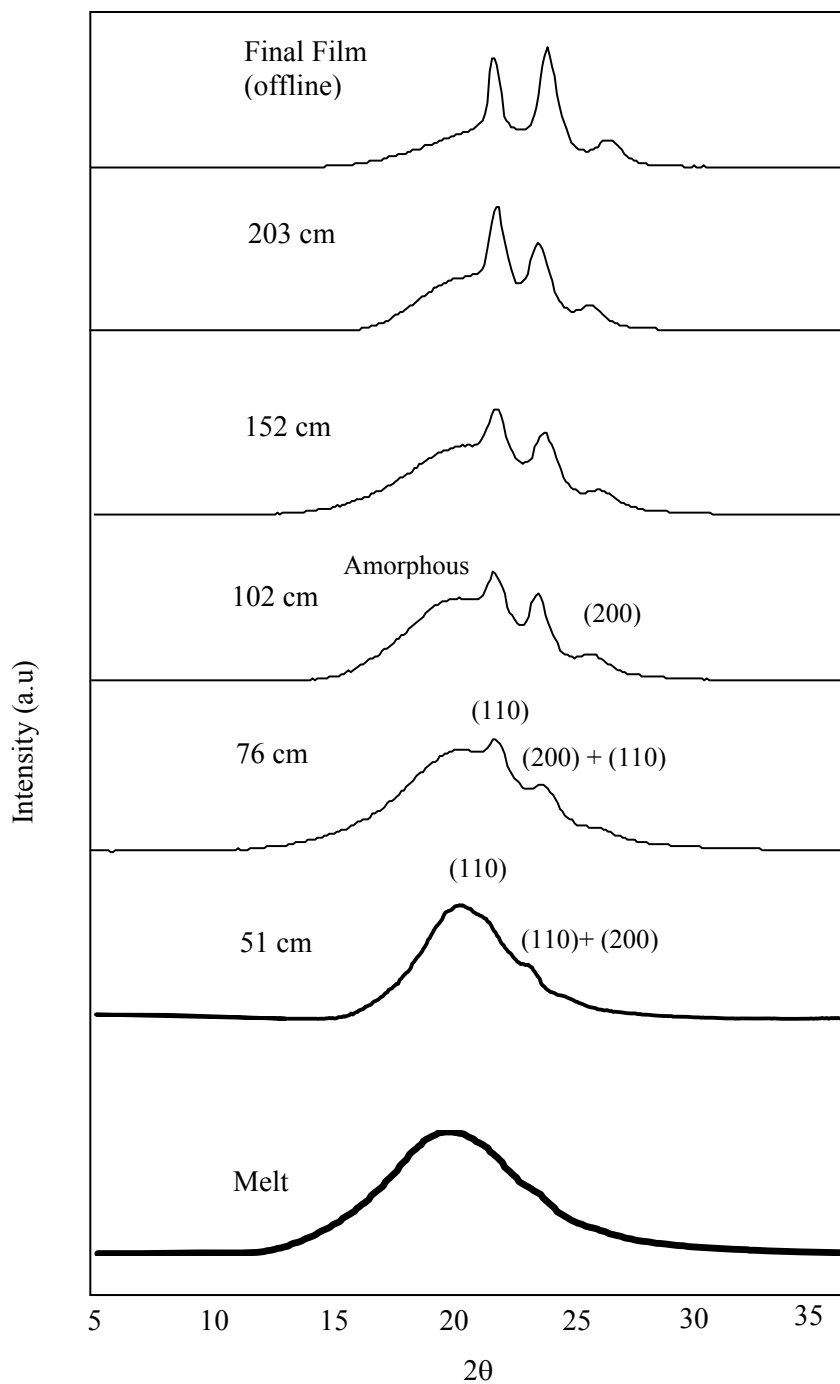
Figure 3.7 Composite WAXD Intensity spectrum at different axial positions

starting from the melt to the processed final film (after nip-roller)

From the composite WAXD spectra, the peak position, peak height, peak width, and integrated intensity for each diffraction arc and amorphous background can be extracted. The deconvolution of the peaks was carried out using a mixed Gaussian-Lorentzian (G-L) function. The center, width of the peak, and the percentage Lorentzian function in the mixed Gaussian-Lorentzian fit that were estimated on the amorphous spectrum (from the melt) were later used to calculate the amorphous content of the composite intensity spectrum obtained at other locations in the film line.

The mixed G-L fit performed on the composite X-ray diffraction spectra of amorphous (molten) and semi-crystalline states of the LDPE bubble are presented in **Figures 3.8a and 3.8b,** respectively. The crystalline content was determined by fitting all of the crystalline peaks obtained for the front and back faces of the bubble. The crystalline fraction in the bubble was estimated using $X_c = I_c/(I_c + I_a)$, where I_c is the area under crystalline peaks and I_a is the area under the amorphous halo [2]. The crystallinity value of 39 ± 2 wt % measured for the processed blown film using cylindrical geometry of the bubble was consistent with a value of 40 ± 2 wt % measured for the same sample with a lay-flat geometry. These results indicate that a suitable deconvolution procedure may be used to analyze the composite spectra.
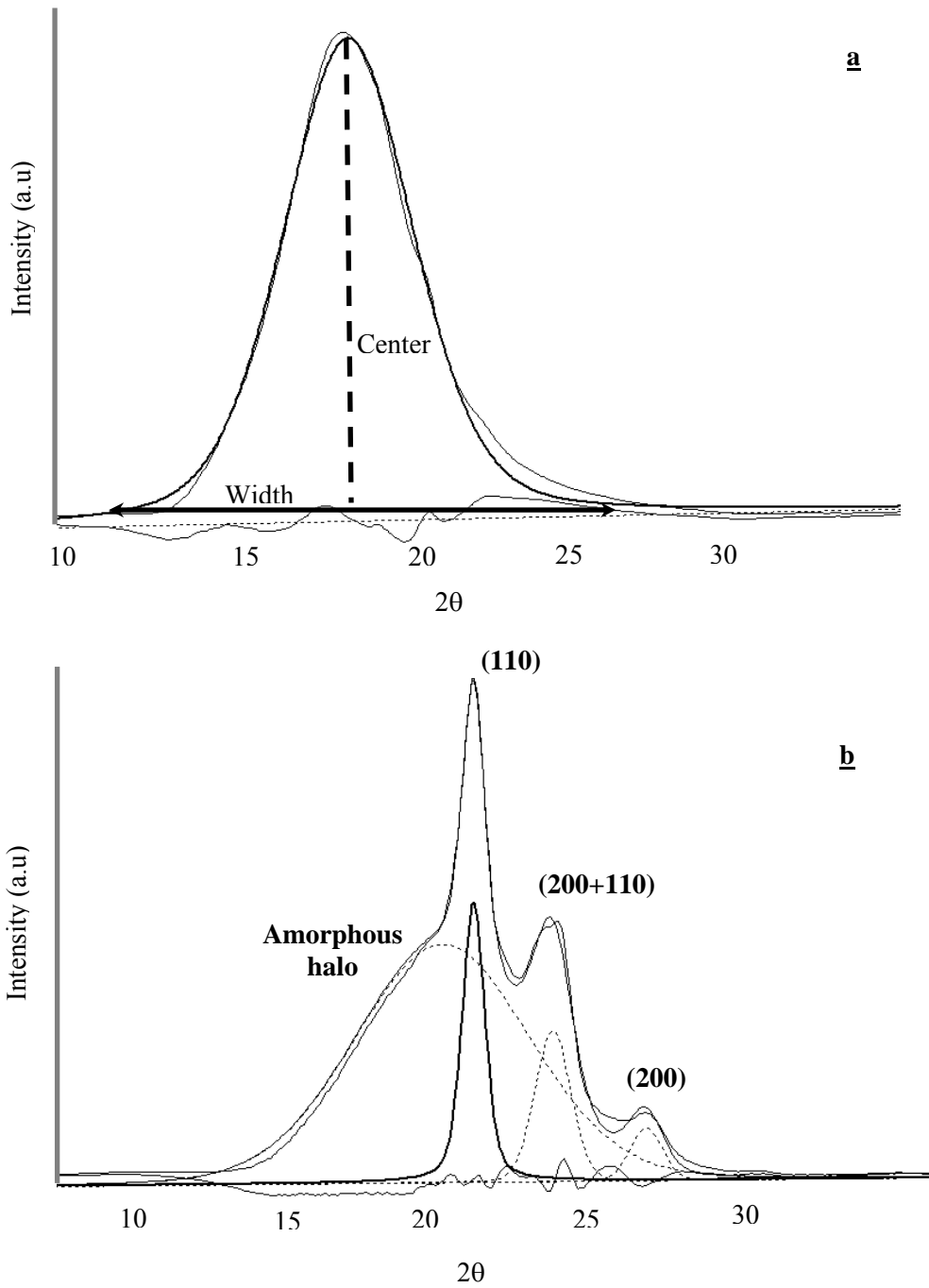
Figure 3.8 Mixed Gaussian-Lorentzian curve fit for composite X-ray intensity spectrum for a) Amorphous halo and b) Semi-crystalline state of the hollow cylindrical polyethylene bubble.

The development of crystallinity as a function of axial distance is presented in **Figure 3.9.** The crystallinity profile from online WAXD measurements displays a sigmoidal shape. The crystalline growth starts near the frost-line height, steeply increases at lower axial distances, and then plateaus at higher axial distances near the nip-rolls. Crystallinity content as low as 2 wt % was successfully detected by real-time WAXD technique. Real-time temperature measurements were also performed using an IRCON Infrared pyrometer (Modline 340, Niles, IL), and the profile is shown on the secondary axis in **Figure 3.9.** The temperature profile shows a plateau at ≈98°C as a consequence of the exothermic heat of crystallization.
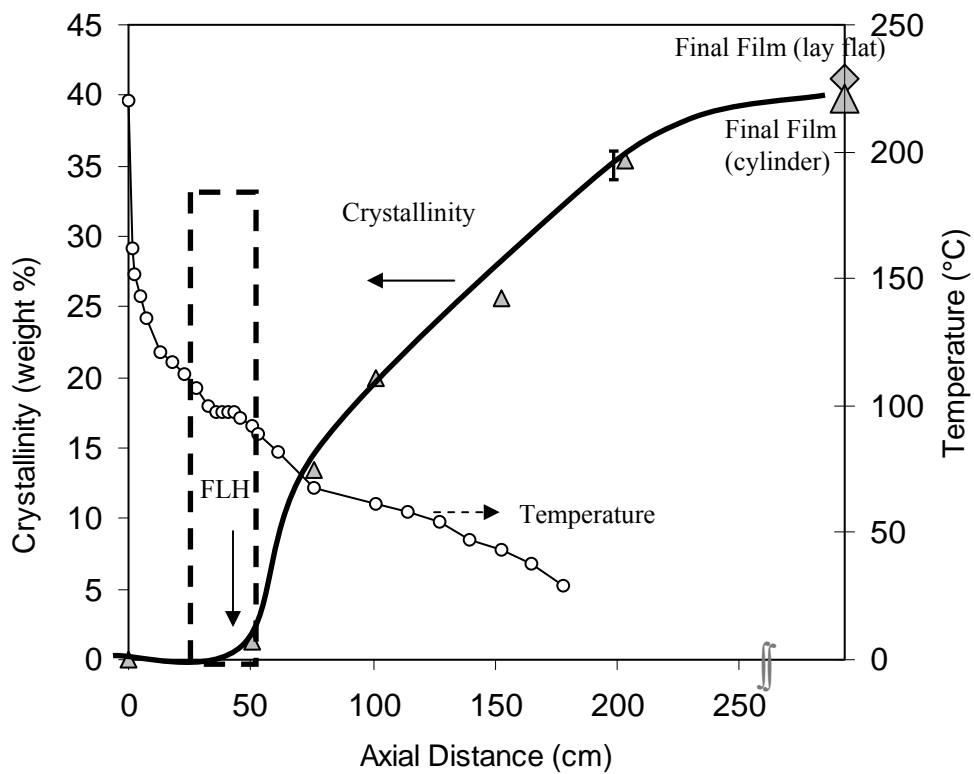
Figure 3.9. Real-time crystallinity profile (solid line represents the trend)

from WAXD along with online temperature profile (secondary axis)

The Raman spectra obtained simultaneously with X-ray diffraction measurements at different axial locations in the film line is presented in **Figure 3.10**. The characteristics features of the spectra are as described in Chapter 1.
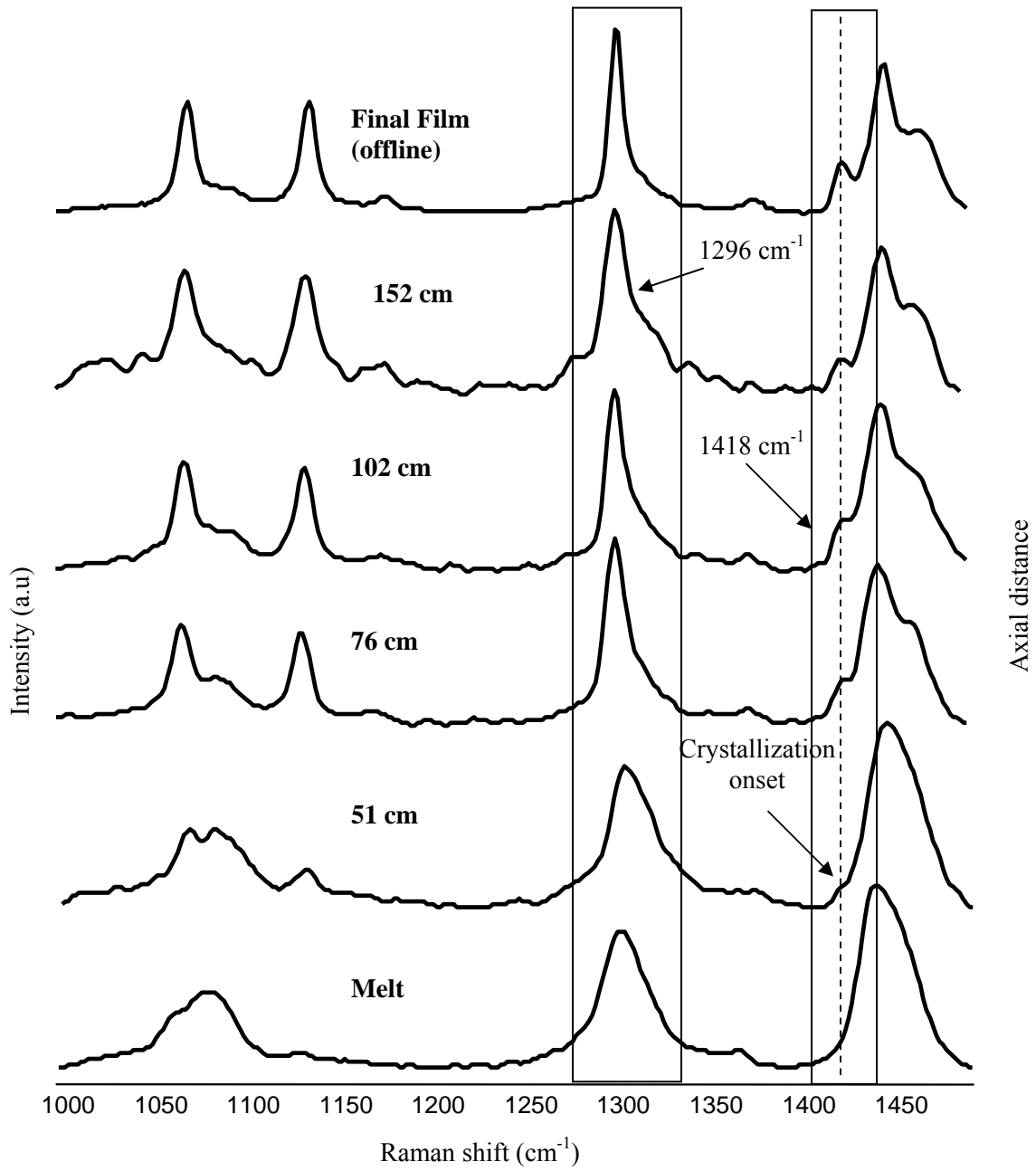
Figure 3.10 Real-time Raman spectra obtained along the axial distance during

X-ray diffraction experiments in blown film

114

Next, in **Figure 3.11**, a comparison of real-time crystallinity measurements from WAXD and Raman spectroscopy is presented. The crystalline content from the Raman spectrum was calculated by calibrating the ratio of integral intensities from 1418 cm^{-1} and 1300 cm^{-1} bands with the crystallinity obtained from differential scanning calorimetry [3]. The two techniques probe microscopic material structure over different length scales, from individual molecular bonds to large-scale domains. They also differ in the information they provide on different phases within a single material (e.g., amorphous and crystalline) and can be used to select complementary sampling volumes due to their different penetration depths within one material. The crystallinity profiles from the two different techniques are consistent (within ± 3 wt %). The crystallinity curves from the present study also show good agreement with trends reported in previous experimental studies[4-6].
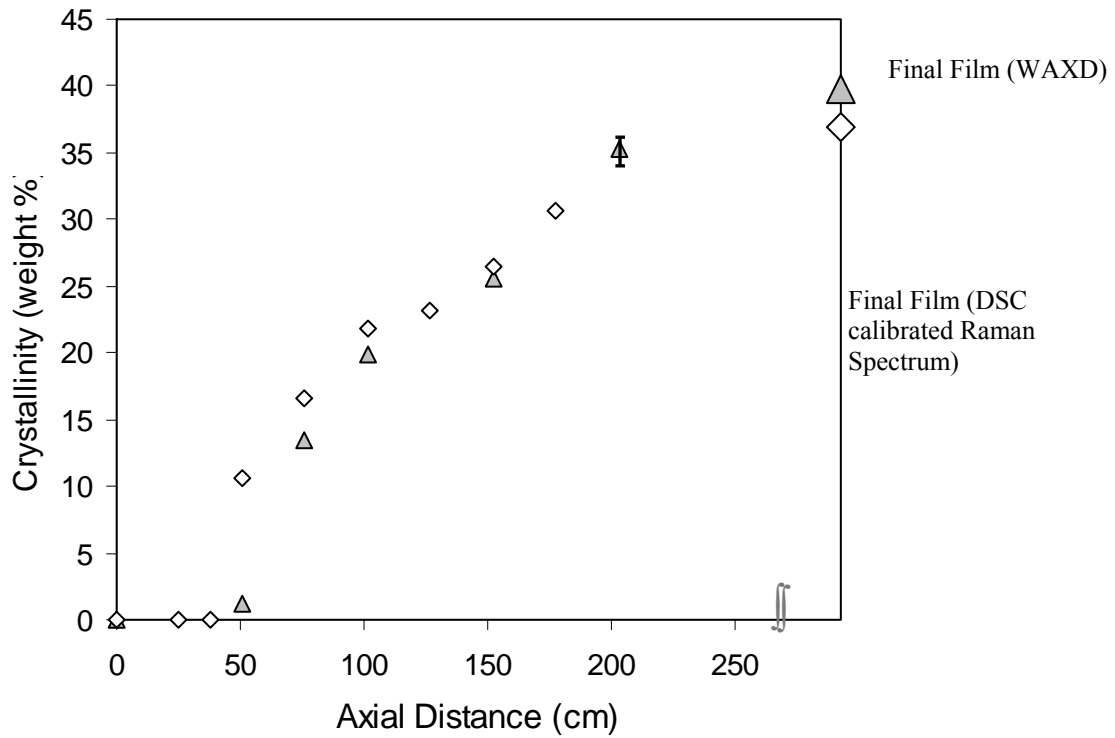
Figure 3.11 Comparison of crystallinity values from real-time Raman

spectroscopy (open diamonds) and online WAXD (solid triangles)

3.2.3. *Effect of take-up ratio*

To investigate the non-isothermal crystalline growth rate, the evolution of
crystallinity was plotted as a function of *process-time* rather than axial distance. In
Figure 3.12, process-*time* is defined as the time taken for a particle exiting the die to

reach a particular location along the film line. The figure displays crystallinity profiles as a function of *process-time* for TURs of 2.5 and 5.5 and at a BUR of 0.6. The curves indicate that the crystallization process starts as the extrudate reaches the FLH, increases along the film line, and finally plateaus. The increase in the crystallization growth rate with an increase in TUR is an indication of stress-induced crystallization[7, 8]. The increase in TUR causes an increase in stress along the machine direction due to faster cooling on the thin film, which results in increased crystallization-rate.
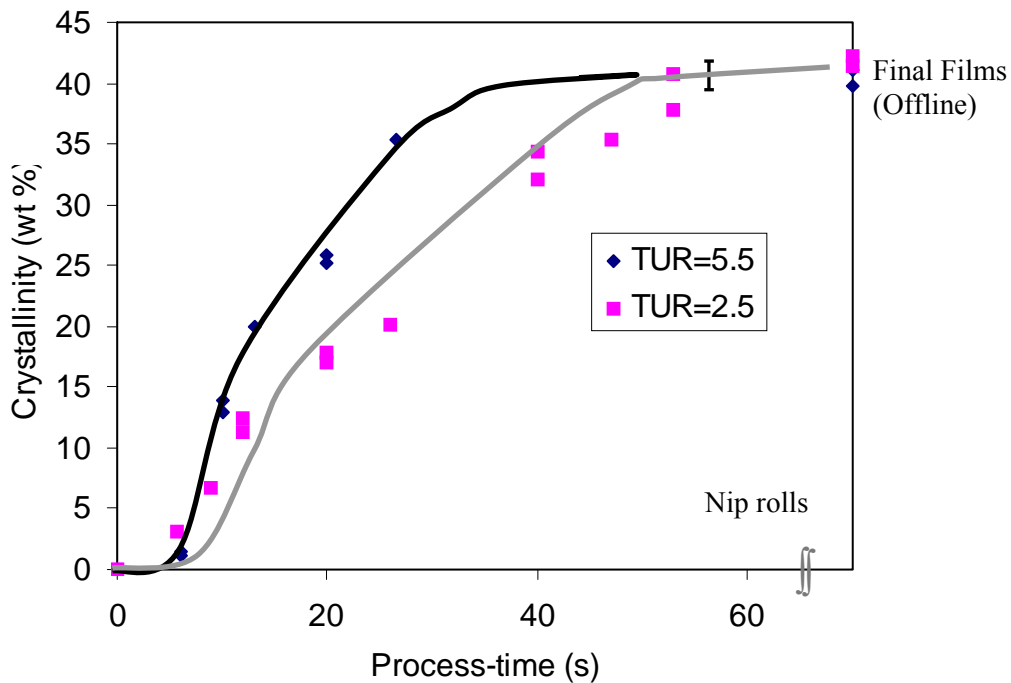
Figure 3.12 Crystallinity profiles from online X-ray diffraction of LDPE at TURs of 2.5, 5.5 at a constant BUR of 0.6 (Curves represent trends)

3.2.4. *Real-time Orientation*

The WAXD patterns were also analyzed for Herman's uniaxial orientation parameters along the axial distance. The patterns typically displayed distributed arcs of (110) and (200) at lower axial distances. The arcs tend to become much more defined and sharper at higher axial distances. The a-axis plane (200) concentrated near the meridian, while the (110) plane showed an arced pattern with maxima off the equator.

The intensity is plotted as a function of azimuthal angle for various axial distances in **Figure 3.13 a and b**. The (200) peak has a maximum about 0°, while the (110) plane showed a maximum at about 25° from the equator. The peaks tend to become narrower at higher axial distances. The orientation parameter calculated from the patterns indicate the formation of row-nucleated lamellar orientation of Keller-Machin I type where the a-axis is oriented along the machine direction and b- and c- axes randomly oriented about the a-axis. The orientation parameter f_a increases from a value close to 0 to 0.01 with axial distance with increase in a-axis orientation, while the f_c value increases from 0 to 0.026.
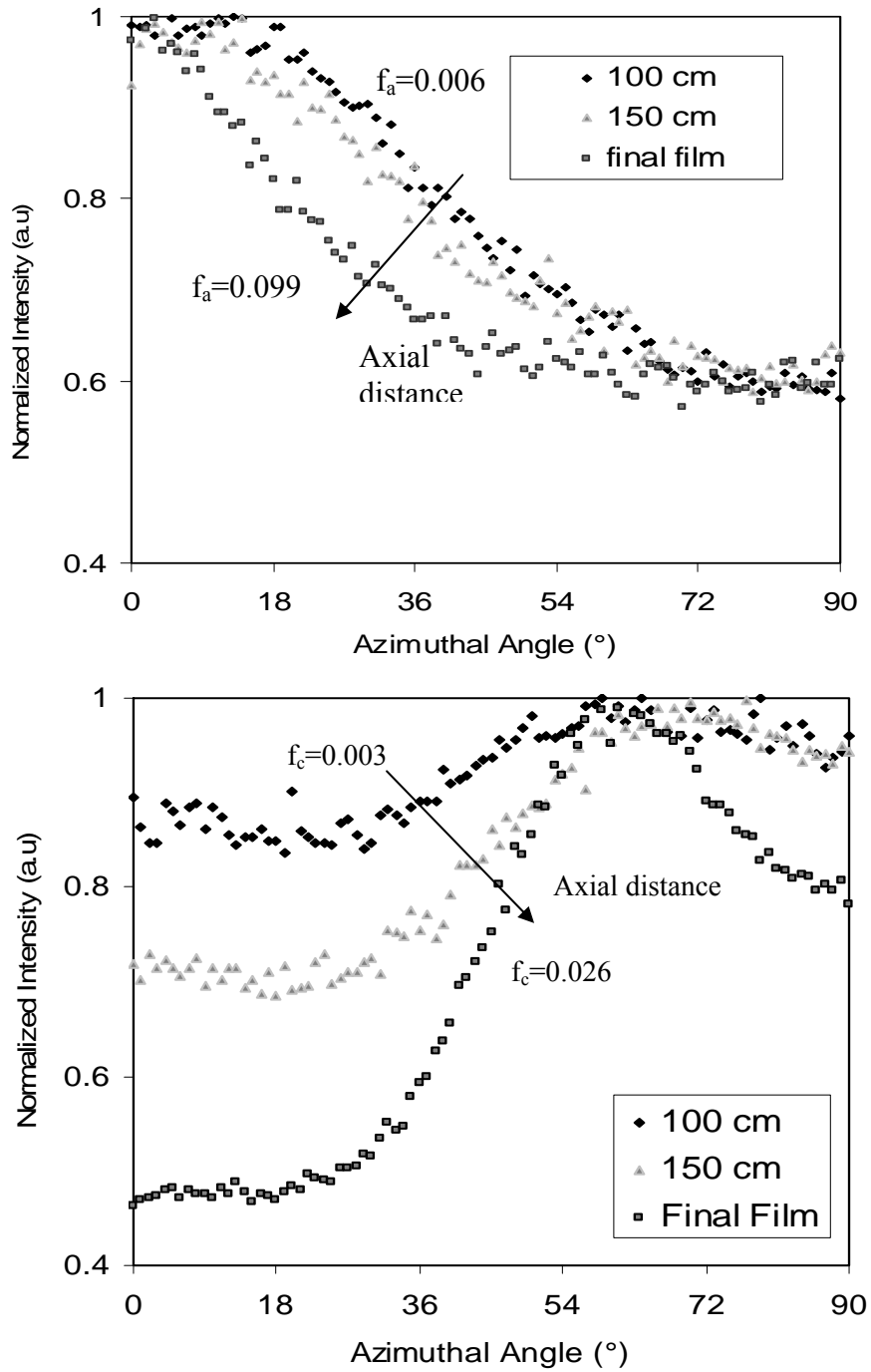
Figure 3.13 Real-time azimuthal scans during LDPE blown film extrusion

for a) (200) plane and b) (110) plane

3.3. Application of real-time X-ray diffraction

Finally, **Figure 3.14** presents a comparison of an offline spectrum obtained from a large-diameter cylindrical film to that obtained from a small-diameter blown film shown earlier (**Figure 3.7**). It is evident that the diffraction peaks generated by the two faces of the large cylindrical blown film are separate. Therefore, for a large-diameter cylindrical bubble, typically obtained from a pilot-scale blown film extrusion, the response from one of the faces of the bubble can be used to analyze for crystallinity (38 wt %) without the need to analyze a composite spectrum. The consistency of crystallinity data from WAXD and Raman spectroscopy indicates that any one of these techniques may be used in a pilot-scale blown film line for the purpose of real-time microstructural measurements.
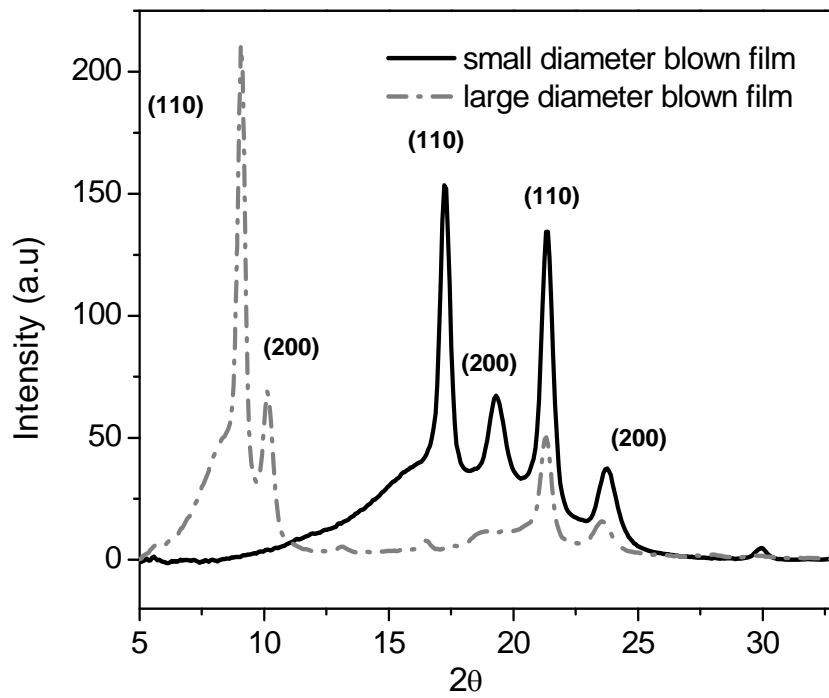
Figure 3.14. 2θ-Intensity spectra from two different diameters
of hollow cylindrical blown film.

3.4. Conclusions

The feasibility of using wide-angle X-ray diffraction for real-time crystallinity measurements during the blown film extrusion of low-density polyethylene was established. From the evolution of (110) and (200) peaks, it was evident that the crystallization process starts near the frost-line height (FLH), shows a steep growth immediately past the FLH, and then plateaus at higher axial distances near the nip-rolls. The real-time crystallinity profiles obtained from WAXD were consistent with those measured using online Raman spectroscopy.

3.5. References

1. Alexander LE. X-ray diffraction methods in polymer science. Huntington, N.Y.: Krieger Pub. Co., 1979.

2. Aggarwal S and Tilley G. Journal of Polymer Science, 1955;18.

3. Strobl GR and Hagedorn W. Journal of Polymer Science Part B-Polymer Physics 1978;16(7):1181-1193.

4. Cherukupalli SS and Ogale AA. Polymer Engineering and Science 2004;44(8):1484 1490.

5. Kanai T and White JL. Polymer Engineering and Science 1984;24(15):1185-1201.

6. Bullwinkel MD, Campbell GA, Rasmussen DH, Krexa J, and Brancewitz CJ. International Polymer Processing 2001;16(1):39-47.

7. Kolnaar JWH, Keller A, Seifert S, Zschunke C, and Zachmann HG. Polymer 1995;36(20):3969-3974.

8. Mchugh AJ. Polymer Engineering and Science 1982;22(1):15-26.

CHAPTER FOUR

REAL-TIME CRYSTALLINITY EVOLUTION IN LDPE/PP BICOMPONENT

BLOWN FILM EXTRUSION USING RAMAN SPECTROSCOPY

Multilayer blown film extrusion involves simultaneous extrusion of two or more polymers through an annular die to form a homogeneous layered structure. It is a desirable technique to make packaging films with superior properties. Therefore, it is important to conduct a systematic understanding of microstructure development in multilayer blown film extrusion as it affects the properties of the films. In this chapter, real-time Raman spectroscopic measurement of crystallinity of the individual components: LDPE and i-PP of a bilayer film (LDPE/PP) during blown-film extrusion is reported. The possibilities and limitations of real-time Raman spectroscopy during LDPE/PP coextrusion are discussed.

4.1 Experimental

4.1.1.Materials and Processing

The pilot-scale bicomponent blown film coextrusion unit consisted of custom-designed 25 mm blown film extruder (Haake, 24:1 L/D ratio) and a 19 mm extruder (Alex James Associates, Greenville, SC, 24:1 L/D) connected to a 50 mm cross-head

annular die (Wayne Machine Die Co., Totowa, NJ) with a 0.635 mm die gap. Low density polyethylene resin, Dow 640 I (density of 0.92 g/cc, and a melt flow index of 2.0 g/10 min) and isotactic polypropylene resin, Dow INSPiRE 112 (density of 0.91 g/cc, and a melt flow index of 1.0 g/10 min) were coextruded to produce LDPE (inner)/PP (outer) bilayer films. The gear pumps in the extruders ensured a constant total mass flow rate of 36 gm/min (50 wt% each) during the process. The mass flow-rates of the components from the extruders were measured each time before the start of the experiment. The die temperature was maintained at 240 °C. The cooling air-flow rate measured using an air velocity transducer (TSI model 8455, St. Paul, MN) near the die exit was 20 m/s. The detailed procedure for extrusion is described in **Appendix A**.

Figure 4.1 presents different combinations of processing parameters in the blown film line. First, the BUR, defined as the ratio of the final bubble-radius to the die-radius, was kept constant at 1.5 and the TUR, defined as the ratio of take-up speed to the velocity of the polymer at the die exit, were 3.3 and 10. Second, the TUR was kept constant at 10 and the BURs were 1.5 and 2. Third, the bubble was subjected to uniaxial stretching with a TUR of 17 and a BUR of 0.8.The total thickness of the processed films as measured using Nikon Digimicro micrometer (Model MFC-101, Melville, NY) were 55-145 microns.
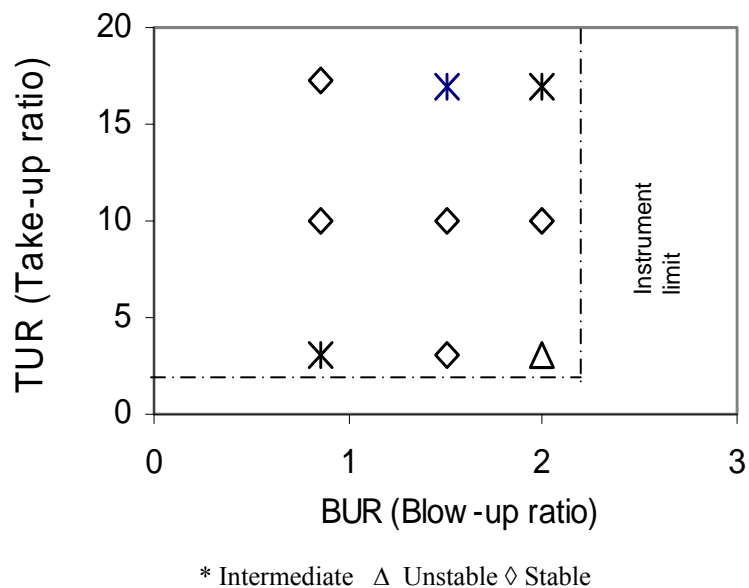
Figure 4.1 Experimental conditions explored in PE/PP blown film coextrusion

4.1.2.Process Measurements and Analysis

4.1.2.1.Offline measurements

Offline conventional Raman measurements were performed using a Renishaw Raman 200 connected to a non-polarized Raman probe (38 mW) fitted with a 20 X objective. Single layer PP and PE blown films of different thicknesses (13 μm, 26 μm &

45 µm) were used for this experiment. The layers were tightly stacked in a metal frame. The films were marked at three different locations and the laser beam was focused within the marks. The accumulation time for each spectrum was 120 s.

Offline confocal Raman and conventional Raman measurements were also carried out on the processed LDPE/PP (50 wt% each) bilayer blown films. The schematic is shown in **Figure 4.2**. Confocal Raman microspectroscopy allows one to probe within the sample without interference from other areas in the path of the incident laser beam. This is achieved by an aperture which discards the signal from out-of-focus laser while allowing the scatter from a point within the sample. For confocal measurements, a Renishaw Raman microspectrometer 100 equipped with a 26 mW He-Ne laser of 785 nm wavelength was used. Using a 100 X magnifying objective and by adjusting the pinhole aperture (10 µm) and the CCD detector area (5 x 574 pixels), a depth resolution of $\approx$ 2 µm can be obtained along the optical axis. Raman spectra of the components, LDPE and PP without influence from one another could be obtained by focusing the laser on the surface of the films. The spectra were acquired at an accumulation time of 120 s.
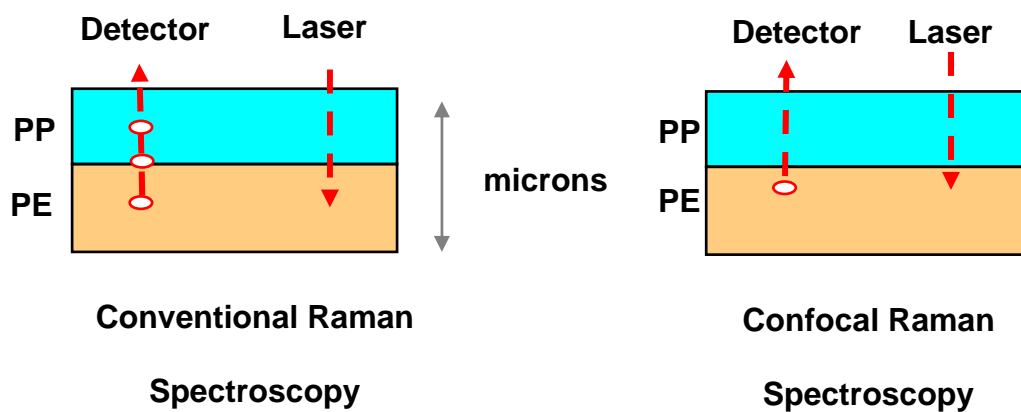
Figure 4.2 Schematic of a) Conventional Raman spectroscopy b) Confocal Raman spectroscopy on PP/PE films

The analysis of the acquired spectrum was performed using GRAMS/32 software (Galactic Inc., Salem, NH), the peaks were deconvoluted and the area under the peaks was obtained by a curve-fitting procedure using a mixed Gaussian-Lorentzian function. The curve-fitting procedure was repeated for 3 times and an average of the integral intensities was calculated.

DSC measurements for calculation of crystallinities of PP and PE were carried out on a Perkin-Elmer Pyris 1 DSC instrument. The thermal scanning involving a heating and a cooling cycle was performed in the temperature range from 50 °C to 190 °C at a rate of 10 °C/min. A minimum of 7 samples were tested. Crystallinity values of PP and PE were

estimated from their respective enthalpies of fusion values (ΔH_f) obtained from the samples (50 wt% each) and using the enthalpy of fusion values of perfect crystalline samples: 138 J/g for PP [1] and 288 J/g of PE [2].

For crystallinity calculation in PP from the Raman spectrum, the integral intensity of 809 cm^{-1} peak was divided by the total integral intensity under 809-841 cm^{-1} band as described by Nielsen et al.[3]. The final crystallinity values calculated from Nielsen's method [3] also correlated to DSC results as $X_{c,\ Raman} = 0.9\ X_{c,\ DSC}$. The crystallinity values were $\approx$ 32 % for LDPE and $\approx$ 53 % for i-PP in all processed films. For PE, total integral area under 1296 cm^{-1} and 1305 cm^{-1} peaks were used as the reference and the ratio of integral intensity at 1418 cm^{-1} and 1296-1305 cm^{-1} bands was calibrated with the crystallinity obtained from DSC measurements on the processed films [4] and subsequently used for calculation of crystallinity at different locations during online measurements.

4.1.2.2. Real-time Measurements

Figure 4.3 shows the experimental setup for real-time measurements during bilayer blown film extrusion. The online Raman system consisted of an unpolarized non-objective Inphotonics probe coupled to a Renishaw Raman system 200. The probe delivered a 130 mW He-Ne laser beam on the film at 785 nm through a 90 μm excitation cable and the Raman scattered light from the film were collected through a 200 μm
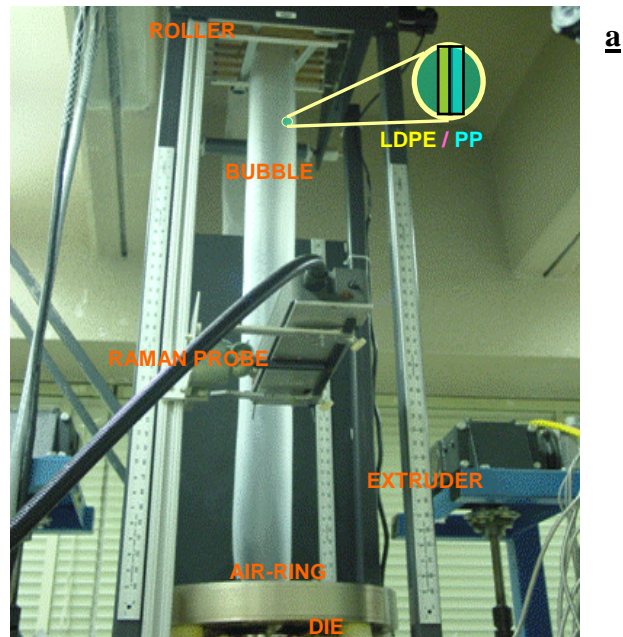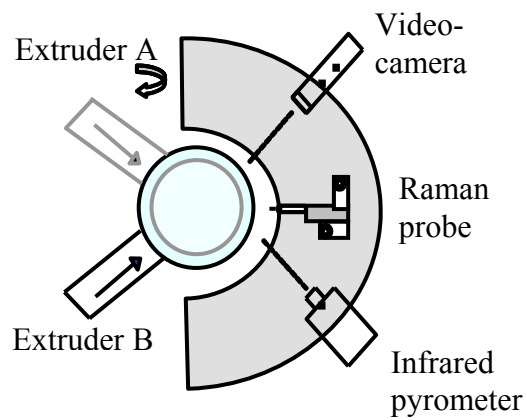
Figure 4.3 Experimental setup for real-time measurements during bilayer blown film extrusion: (a) Photographic image of blown film coextrusion line with Raman probe, and (b) schematic of blown film line with online instruments.

collection fiber. The device was mounted on a y-z micrometer stage and was moved axially (z-direction) to obtain spectra at 12 different z-positions in the film line, starting from the melt up to the nip rolls. A minimum of 3 spectra were obtained from each location. The spectrum at each point was recorded using Renishaw WiRE 1.3 β data acquisition software covering a spectral range of 750-1500 cm^{-1} for an accumulation time of 300 s in the static capture mode (**Appendix B**).

The bubble surface temperature was also measured along the film line at every 2.5 cm interval using an IRCON modline 340 camera with a 3.43 μm IR frequency filter suitable for polyolefin films. The resolution of the instrument was ± 2 °C. The IR camera was placed at distance approximately 42 cm to minimize the spot size (≈0.3 mm) in the target. Five temperature readings at each location were measured and an average is reported.

4.2. Results and Discussion

4.2.1. Offline Raman measurements

Figure 4.4 represents a typical Raman spectrum of a single-layer polyethylene (LDPE) film, a single-layer polypropylene (PP) film and a bicomponent LDPE/PP blown film. As seen in **Figure 4.4a**, the CH_2 rocking and C-C stretching peaks (809-841 cm^{-1}) used for crystallinity measurement in PP are characteristic of the helical structure present in PP [19] and are not present in polyethylene. Also, as shown in the blocks in **Figure 4.4b**, the methylene-bending peak at 1418 cm^{-1}, used for calculation of orthorhombic content in PE, is characteristic only of PE.

Figure 4.4c represents the superimposed spectrum obtained from a bilayer LDPE/PP film with contribution from the components PE and PP. The 1296–1305 cm^{-1} peak, it turns out, is present in both PE and PP. However, its intensity is reported to be very weak in PP compared with that in PE [5, 6]. Recent studies by Quintana and co-workers on PP/PE blends [5] and Markwort et al.[6] on heterogeneous polymer systems using Raman spectroscopy, and reported the 1296–1305 cm^{-1} band as characteristic of PE and only slightly influenced by the PP component in PP/PE blends. **Figure 4.4c** displays the spectrum obtained from a bilayer LDPE/PP film with contributions from both components; the spectrum appears generally consistent with that reported for the LDPE/PP blends.[5, 6] **Table 4.1** [7, 8] lists some of the important crystalline peaks observed in a Raman spectrum of polypropylene and polyethylene films with their corresponding vibration modes and characteristic intensities.
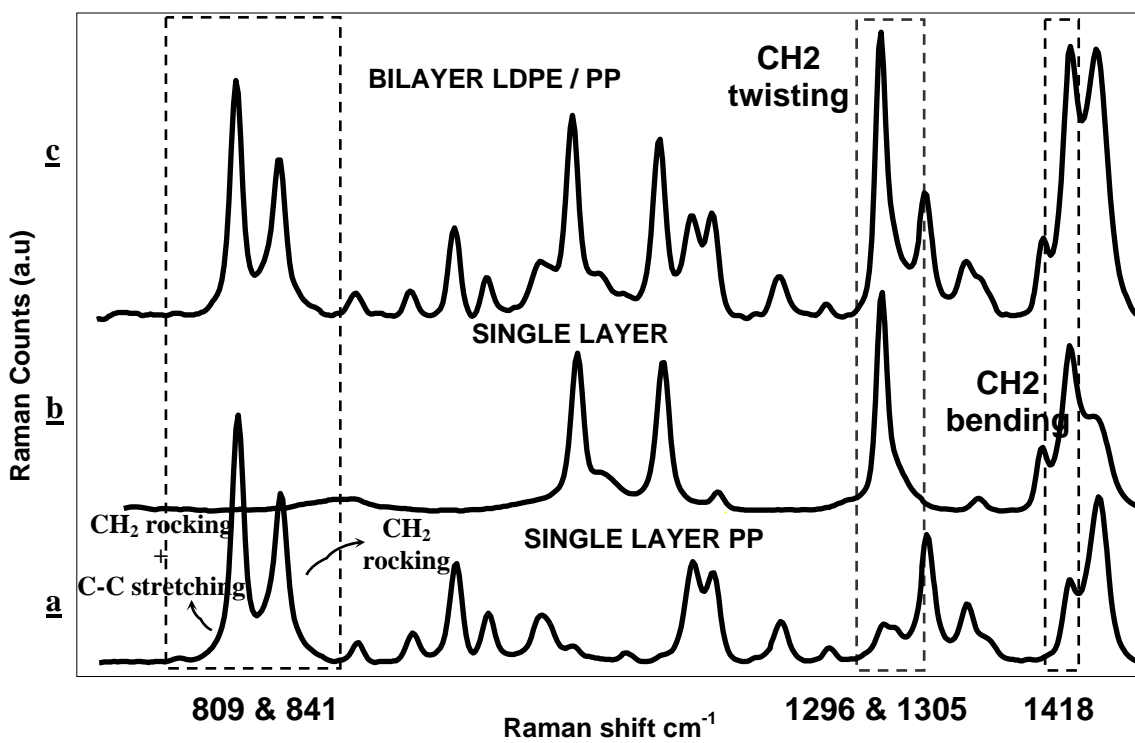
Figure 4.4 Raman spectra for: (a) single-layer polypropylene, (b) single-layer

polyethylene, and (c) bilayer LDPE/PP films

Table 4.1 Raman peaks of i-PP and LDPE

Raman shift (cm^{-1})	PP	PE
809	$\nu CH_2 + \nu C\text{-}C + \nu C\text{-}CH$ (vs)	_
841	$rCH_2 + \nu C\text{-}CH_3$ (vs)	_
972	$rCH_3 + \nu C\text{-}C$ chain (s)	_
1062	_	ν_s (C-C) (m)
1130	_	ν_{as} (C-C) (m)
1152	ν (C-C) $+ \nu C\text{-}CH_3 + \delta$ CH $+$ rCH_3 (vs)	_
1220	$tCH_2 + \delta$ CH $+$ $\nu C\text{-}C$ (s)	_
1296	$\omega(CH_2) + \delta$ CH weak (vw)	tCH_2 (vvs)
1307	$\omega(CH_2) + t\,CH_2$ weak (vw)	tCH_2 (w)
1330	δ CH $+ t\,CH_2$ (vs)	_
1418	_	ωCH_2 (w)
1435	$\delta\,CH_3$ asym (w)	_
1440	_	δCH_2 (vs)
1460	$\delta\,CH_3$ asym $+ \delta(CH_2)$ (vs)	$2 \times rCH_2$ (m)

(ν = stretching, r = rocking, t = twisting, ω = wagging, δ = bending, v = very,

s = sharp, w = weak, m = medium)

Prior to the real-time Raman measurements, offline Raman measurements were performed using conventional Raman and confocal Raman spectroscopy to determine the masking effect of PP layer upon PE layer and vice versa. **Figures 4.5 and 4.6** show the curve fitting procedure followed for single layer PP and LDPE films and bicomponent LDPE/PP films, respectively. The crystallinity obtained from the DSC measurements was $\approx$32% for LDPE and $\approx$53% for i-PP in all processed films.
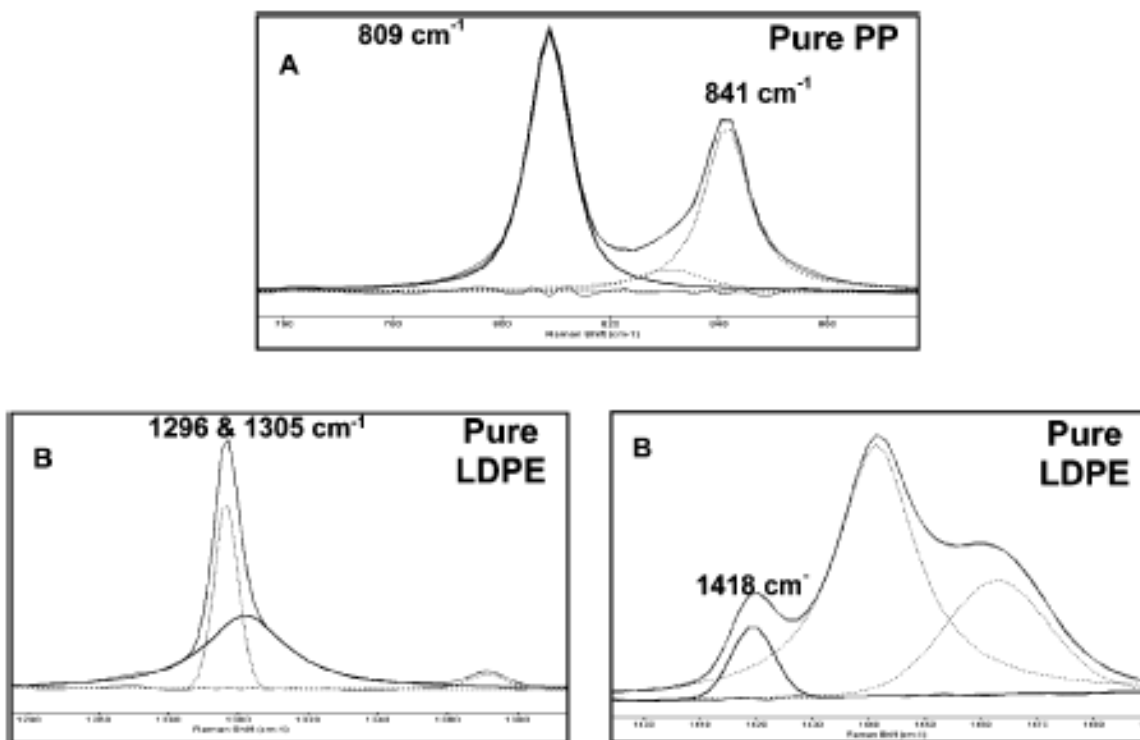
Figure 4.5 Curve fitting for determination of crystallinity using mixed Lorentzian–Gaussian function: (A) single layer PP film and (B) single layer LDPE film
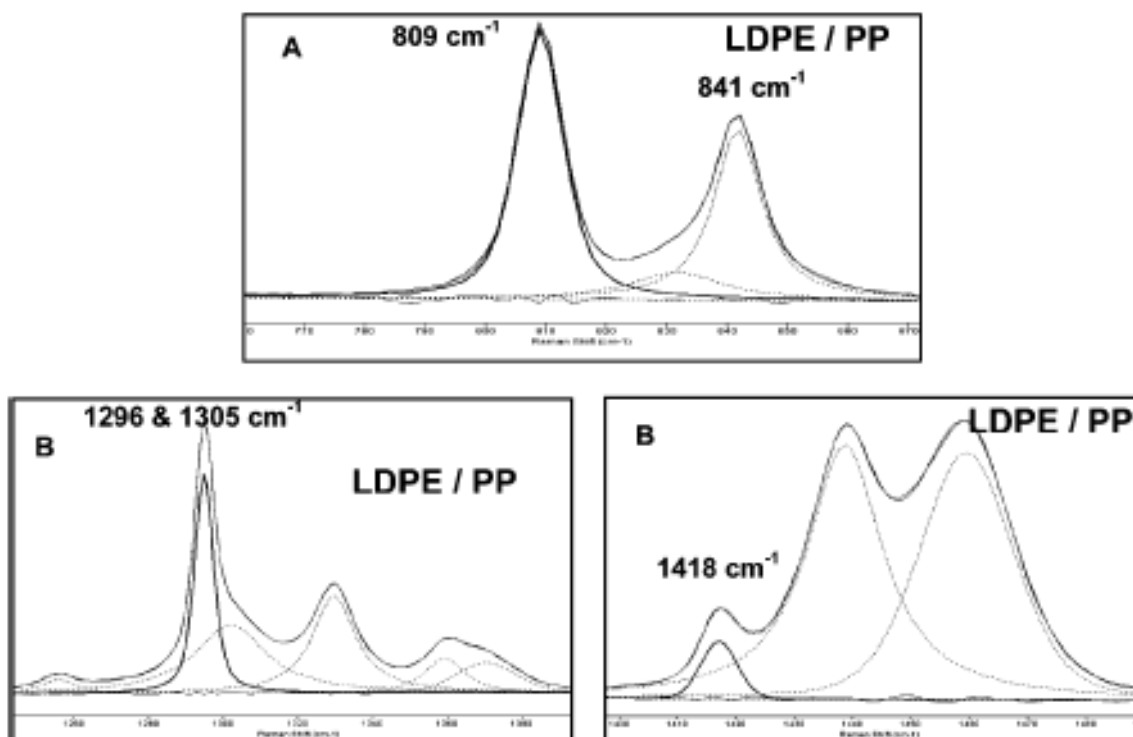
Figure 4.6 Curve fitting for determination of crystallinity in LDPE/PP films using mixed Lorentzian–Gaussian function; (A) PP component and (B) LDPE component

Figure 4.7a displays the integral intensity ratio $I_{809}/I_{(809 + 835 + 841)}$ of the bottom PP layer when PE films were stacked over it. As shown, the apparent integral intensity ratio $I_{809}/I_{(809 + 835 + 841)}$ of PP were not significantly affected by the presence of top PE layer. The PP layer could be probed through the top PE layer upto a total thickness of ≈180 μm.

Figure 4.7b displays the effect of PP on top of PE layer. As observed, the integral intensity ratio, $I_{1418/1296}$ of PE is not significantly affected by the presence of PP layer upto a thickness of ≈45 μm. However, the integral intensity $I_{1418/1296}$ start to drop from the actual values when the PP layer thickness was increased to ≈90 μm. This is likely due to the opacity of the PP film with high % haze compared to PE [9, 10], which causes the intensity of the weak 1418 cm^{-1} peak (crystallinity peak) of bottom PE layer to diminish as compared with strong 1296 cm^{-1} peak. LDPE film, being optically transparent, allowed higher penetration of the beam through its layers than PP film. Thus the optical clarity [11] of the material plays a major role in determining the intensity of Raman scattered light to the detector and henceforth on the masking effect of PP on PE.
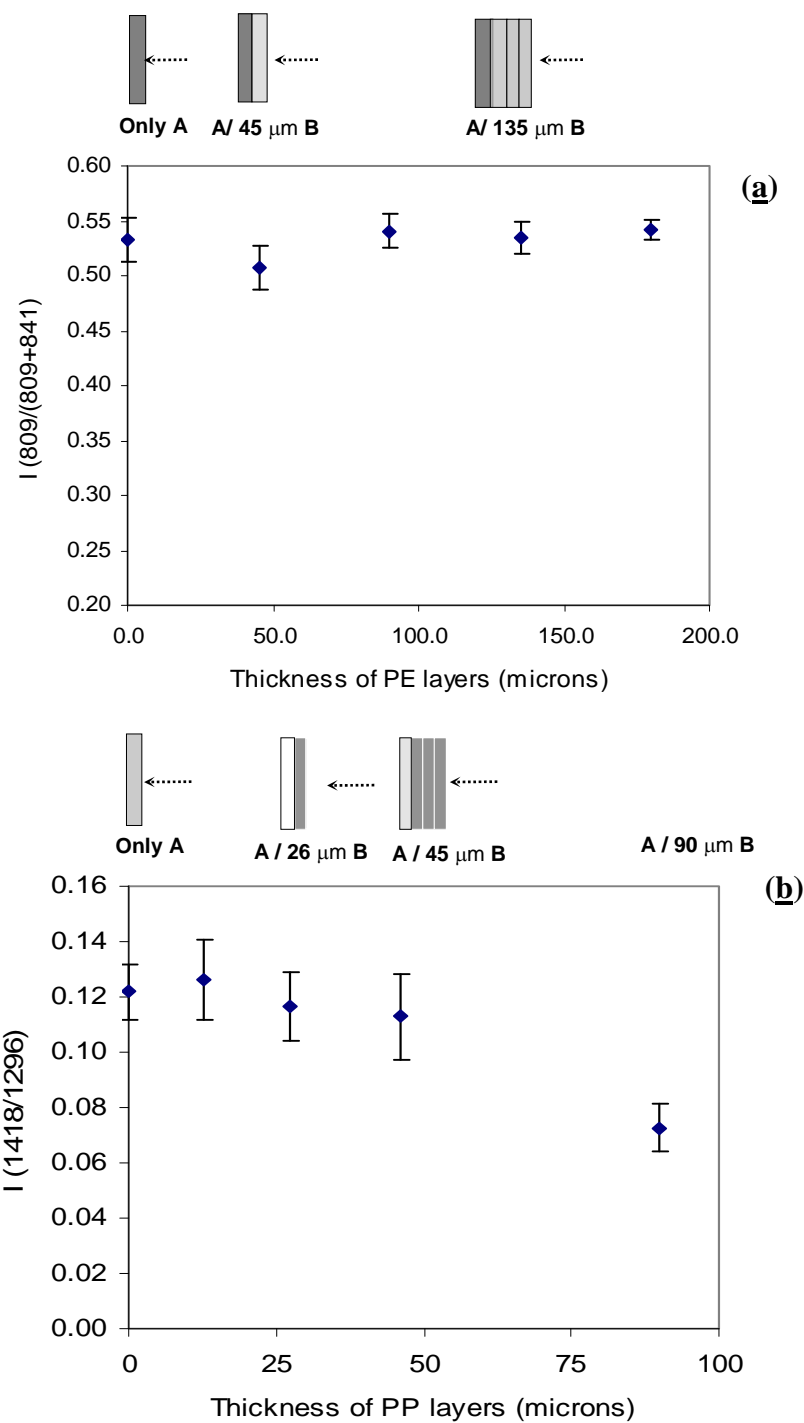
Figure 4.7 Measured values of crystalline peak ratio for a given component A as influenced by the presence of top layers of various thickness of component B: a) A-PP, B-LDPE; (b) A-LDPE, B-PP

In a complementary study, confocal Raman spectroscopy was performed on the processed LDPE/PP blown films. Raman spectra obtained through optical sectioning of the individual layers of PP and PE was compared with superimposed Raman spectra obtained using the non-confocal online Raman probe. The results are presented in **Table 4.2** for films obtained under four different processing conditions. The crystalline intensity ratio of $I_{1418\,/\,1296}$ calculated from the Raman spectra of the component PE by confocal Raman spectroscopy can be compared with the intensity ratio ($I_{1418\,/\,1296}$) obtained from the superimposed Raman spectra of PE-on-PP and PP-on-PE films.

Table 4.2: Comparison of confocal and conventional Raman measurements on PE/PP films

Condition		Total Thickness (μm)	PE ($I_{1418\,/1296}$) (CONFOCAL)	PP/PE ($I_{1418\,/\,1296}$) (CONVENTIONAL)	PE/PP I($_{1418\,/\,1296}$) (CONVENTIONAL)
BUR	TUR				
0.8	17	61	0.16±0.01	0.14±0.02	0.13±0.02
1.5	4	146	0.13±0.01	0.13±0.01	0.13±0.01
1.6	10	55	0.15±0.01	0.16±0.01	0.16±0.003
2	10	38	0.16±0.01	0.14±0.02	0.16±0.02

The data reveals that the characteristic intensity ratios of the components: PE ($I_{1418 / 1296}$) and PP ($I_{809/ (809 + 835+ 841)}$) are not significantly different from the intensity ratios obtained from the superposed Raman spectra of PP/PE or PE/PP films, indicating that the interaction of Raman spectrum from PP and PE layers does not significantly affect their crystalline intensity ratios. The difference in the depth of probe compared to the previous offline Raman experiments (20X objective probe) can be attributed to the objective and small air-gap that might have reduced the optical volume of illumination on the sample, when several single-layer films were stacked during the Raman experiments.

It becomes evident from this study that the presence of ~50 μm of PP on PE or vice versa does not significantly change their integral intensity ratio values used for calculation of their respective crystallinity. Since, the 809-841 cm^{-1} band and 1418 cm^{-1} are unique to PP and PE, respectively, and the integral area of the 1296-1305 cm^{-1} reference band of PE remains constant irrespective of the state of the polymer, the integral intensity ratios $I_{1418 / 1296}$ and $I_{809/ (809 + 835+ 841)}$ can be used as a very good approximation to probe the crystalline growth in real-time during blown film coextrusion of LDPE and PP, respectively. It is also important to note that in a typical film blowing process, the layers are transparent in the melt state and the films produced are less than 50 μm thick. In addition, the crystallization starts close to the freeze-line height, the point after which the film thickness becomes nearly constant. Therefore, based on our confocal and conventional Raman spectroscopy measurements on PP/PE film, the technique can be a used to estimate crystallinity during PE and PP coextrusion if the thickness of the outer layer is about 50-70 μm.

4.2.2. Real-Time Raman Measurements during PE/PP Coextrusion

Figure 4.8 displays a series of real-time Raman spectra obtained for the bilayer blown film line for a take-up ratio of 1.5 and a blow-up ratio of 10. The Raman spectra in the melt are devoid of any characteristic crystalline peaks. The broad bands from PP and PE indicate the amorphous nature of the melt. Near the freeze-line height, a characteristic peak appears at 809 cm^{-1}, indicating the onset of crystallization of PP. Farther up in the line, the peak 1418 cm^{-1} appears indicating the onset of crystallization of PE component. The development of structure with axial distance is evident from the increase in intensity of the characteristic bands for crystallinity, i.e., increase of 809 cm^{-1} relative to 841 cm^{-1} for PP and development of 1418 cm^{-1} for PE. The transformation taking place in PE can also be confirmed from the emergence of a crystalline peak at 1130 cm^{-1}. The crystallinity peaks of PP and PE gradually become intense along the axial direction and saturate at some distance in the film line when the bubble temperature drops.
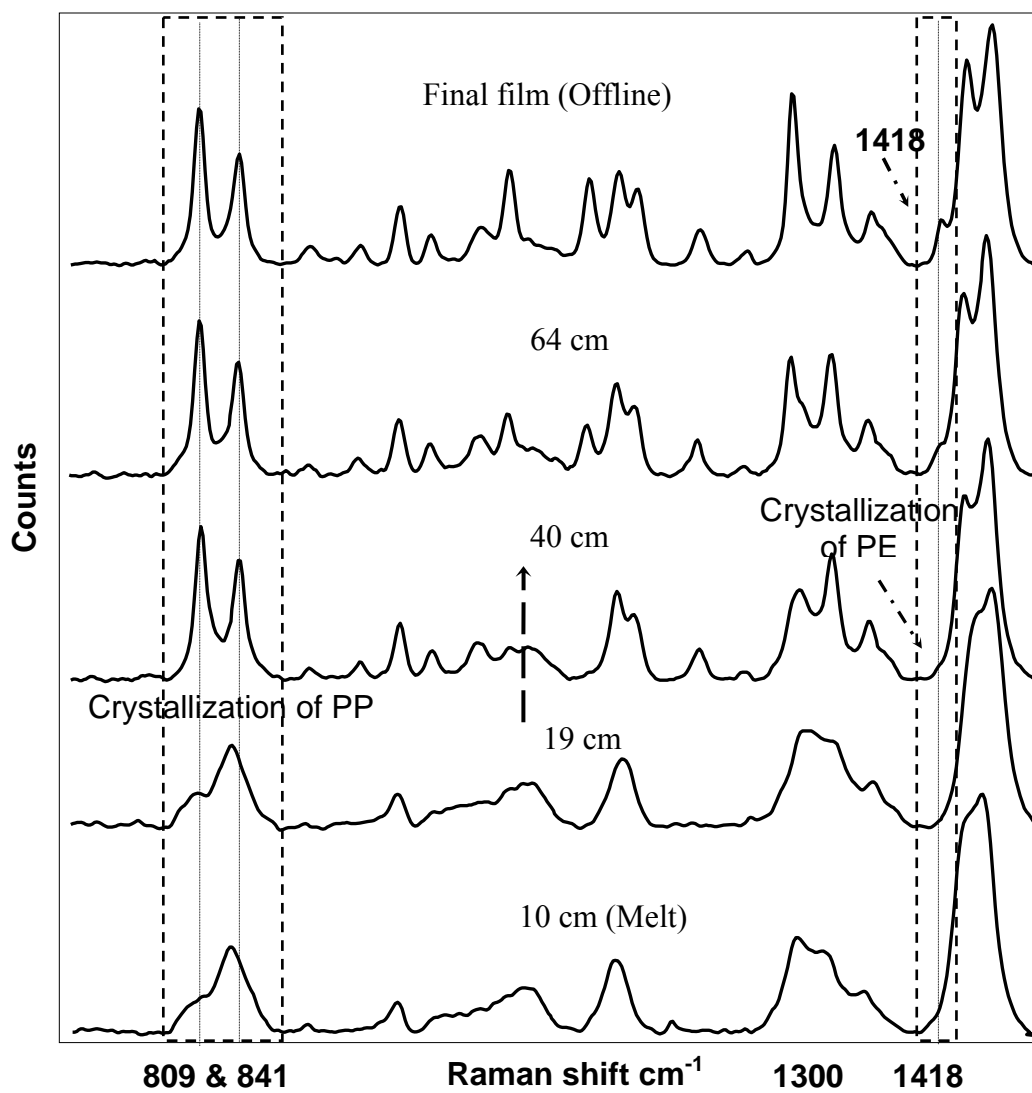
Figure 4.8 Real-time Raman spectra at different axial positions between die
exit and nip rolls during PP/LDPE bilayer blown film extrusion

Figure 4.9 displays the crystallinity of the components plotted as function of axial distance in the film line for TUR = 10 and BUR = 1.5. The profile for PP shows a steep increase initially and then equilibrates at some distance in the film line; a similar trend is also observed for PE but farther up in the line.
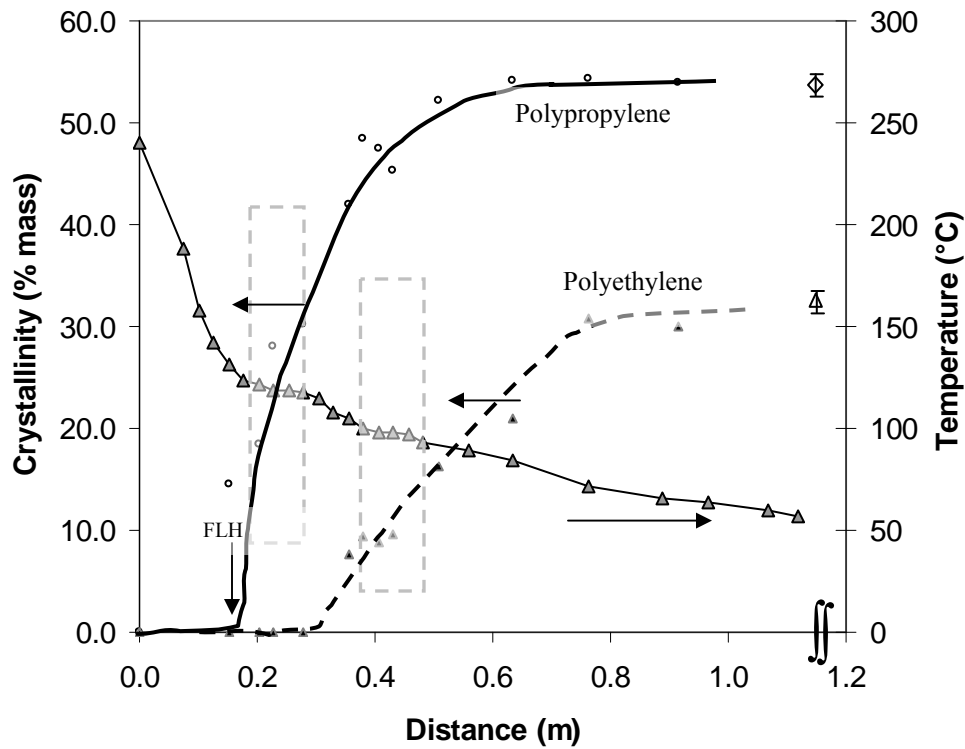
Figure 4.9 Crystallinity values obtained from real-time Raman spectra plotted as a function of axial distance for TUR = 10, BUR = 1.5 and moderate cooling condition during PP/LDPE blown film extrusion. Real-time temperature data presented on the right axis (Solid and dashed curves represent trends)

The temperature profile presented in **Figure 4.9** for PE/PP blown film coextrusion showed a peculiar behavior. The trend showed two plateaus due to the exothermic heat of crystallization, first due to PP ($\approx$ 122 °C) and second due to crystallization of PE ($\approx$ 99°C). The crystallinity profile plotted along with the temperature profile is consistent with this observation. As shown in **Figure 4.10** these double plateaus were more prominent for low and moderate cooling air flow and less so at high cooling. However, this trend was not observed during blown film coextrusion of HDPE and EVOH in the study reported by Morris et al.[12], which may be attributed to the processing conditions used during the studies.
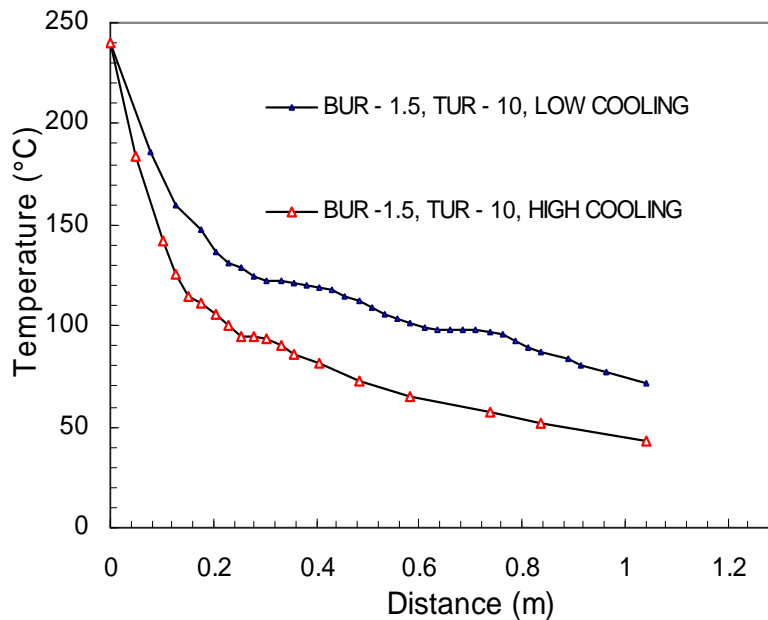
Figure 4.10 Temperature trends for low and high cooling conditions

(Curves represent trends)

Figure 4.11 shows the crystallinity values of the components, PP and PE plotted against process time [13, 14], defined as the time taken by a particle or a mark on the bubble to travel from the die exit to the nip-rolls (measured from video-tracer technique). Polypropylene crystallizes first showing a sharp increase initially and then plateaus, while polyethylene starts to crystallize later and shows a similar trend. The effect of the take-up speed can be seen for the bubble stretched equally in the transverse direction (TD), BUR = 1.5 and differently in the machine direction (MD), TUR of 3.3 and 10. The steepness of the curve for high TUR is more than the slope of the curve for the bubble, which was subjected to less TUR, indicating higher crystalline growth rate at high speed for the components, PP and PE. The increase in the crystallization growth rate of the components with an increase in TUR is an indication of stress-induced crystallization where the increase of oriented fibrils acts as nuclei to accelerate the crystal growth [15, 16]. The significance of crystallization growth rate of the components on its morphology and orientation will be discussed in the next chapter.
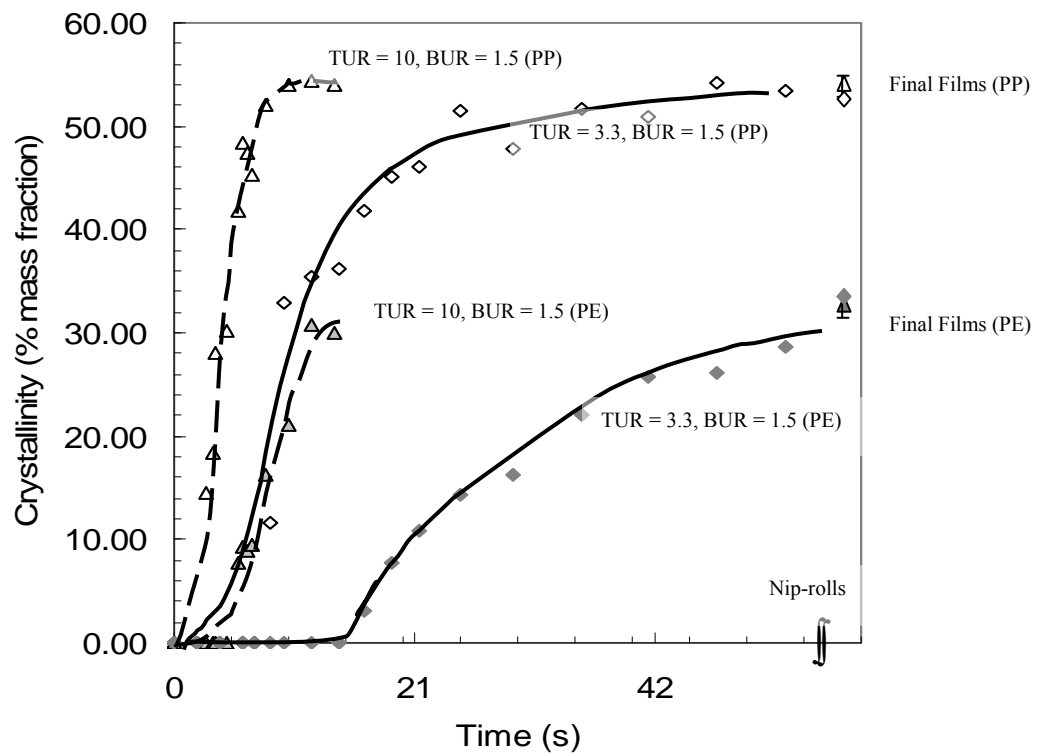
Figure 4.11 Crystallinity values of PP and PE plotted as a function of process time for two different take up ratios: 3.3 and 10 at constant BUR and cooling conditions (curves represent trends).

The effect of BUR on the crystallization growth rates of components PE and PP are presented in **Figure 4.12**. The crystalline growth of the component PP at a higher bubble pressure was faster initially compared to film blown at low pressure, but the crystalline growth rate were not significantly different at a later time for both the conditions. However, for the component PE, the increase in bubble pressure did not show a significant increase in the crystallization growth rate of the component. This may be attributed to the fact that the two bubble pressures were not widely different.
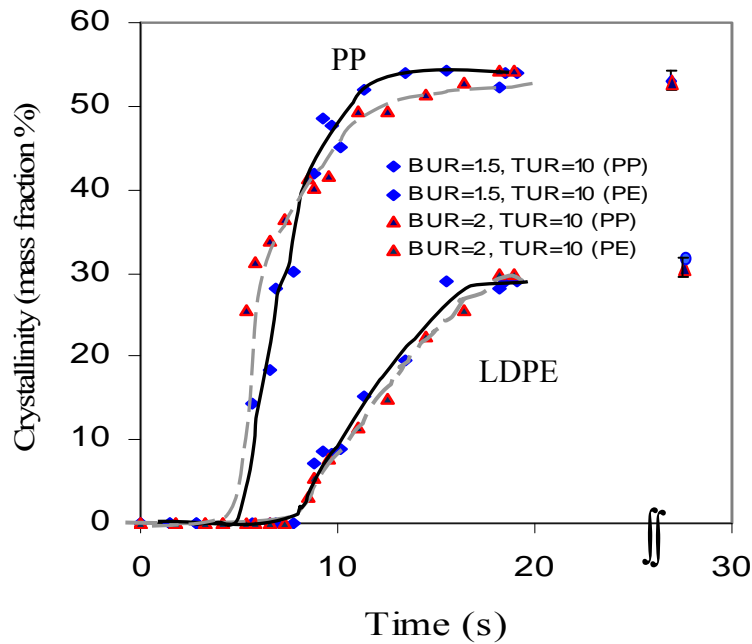
Figure 4.12 Crystallinity against process time: BUR varied from 1.5

to 2 and TUR constant at 10. (Solid curves represent trends)

4.3. Conclusions

Raman spectroscopy was shown to be a promising technique for real-time monitoring of crystalline growth of individual components in bicomponent LDPE/PP blown films. The technique using unpolarized and non-confocal probes was found to be valid for PE/PP bilayer films in which the components show good optical clarity and have layer thickness about 50-70 μm. The offline conventional and confocal Raman measurements indicated that the 809-841 cm^{-1} crystalline bands of PP are unaffected by the presence of PE and the use of 1296-1305 cm^{-1} for the calculation of crystallinity of PE as a good approximation in PP/PE film. The crystallinity profile was consistent with the observation of double plateau in PE/PP blown films. The crystalline growth of PP and PE components increased as the take-up speed was increased.

4.4. References

1. Yuksekkalayci C, Yilmazer U, and Orbey N. Polymer Engineering and Science 1999;39(7):1216-1222.

2. Paradkar RP, Sakhalkar SS, He X, and Ellison MS. Journal of Applied Polymer Science 2003;88(2):545-549.

3. Nielsen AS, Batchelder DN, and Pyrz R. Polymer 2002;43(9):2671-2676.

4. Strobl GR and Hagedorn W. Journal of Polymer Science Part B-Polymer Physics 1978;16(7):1181-1193.

5. Quintana SL, Schmidt P, Dybal J, Kratochvil J, Pastor JM, and Merino JC. Polymer 2002;43(19):5187-5195.

6. Markwort L, Kip B, Dasilva E, and Roussel B. Applied Spectroscopy 1995;49(10):1411-1430.

7. deBaez MA, Hendra PJ, and Judkins M. Spectrochimica Acta Part a-Molecular and Biomolecular Spectroscopy 1995;51(12):2117-2124.

8. Maxfield J, Stein RS, and Chen MC. Journal of Polymer Science Part B-Polymer Physics 1978;16(1):37-48.

9. Bheda JH and Spruiell JE. Polymer Engineering and Science 1986;26(11):736-745.

10. Stehling FC, Speed CS, and Westerman L. Macromolecules 1981;14(3):698-708.

11. MacDonald AM, Vaughan AS, and Wyeth P. Applied Spectroscopy 2003;57(12):1475-1481.

12. Morris BA. Journal of Plastic Film & Sheeting 1999;15(1):25-36.

13. Cherukupalli SS and Ogale AA. Polymer Engineering and Science 2004;44(8):1484-1490.

14. Dees JR and Spruiell JE. Journal of Applied Polymer Science 1974;18(4):1053-1078.

15.   Kolnaar JWH, Keller A, Seifert S, Zschunke C, and Zachmann HG. Polymer 1995;36(20):3969-3974.

16.   Mchugh AJ. Polymer Engineering and Science 1982;22(1):15-26.

CHAPTER FIVE

EFFECT OF COEXTRUSION ON THE MICROSTRUCTURE OF PP/LDPE

BICOMPONENT BLOWN FILMS

During the film blowing process, polymer molecular characteristics couple with

processing conditions to produce the film morphology that ultimately determines the end-

use properties. In Chapter 4, Raman spectroscopy was established as a powerful tool for

estimation of microstructure development during the production of multi-layer films that

are of paramount importance in industrial applications. In this chapter, the crystallinity in

individual components that was measured using Raman spectroscopy is utilized to

understand the complex multilayer blown film extrusion process. The objective of the

present work was to investigate the effect of blown film coextrusion process on the

molecular orientation and crystalline morphology of the components in LDPE/PP bilayer

blown films.

5.1. Experimental

Low density polyethylene (LDPE 640 I, Dow Chemical Co.) and isotactic

polypropylene (PP INSPiRE 112, Dow Chemical Co.) were used throughout this study.

The lab-scale bilayer blown film coextrusion unit consisted of a 25 mm and a 19 mm

extruder (Alex James Associates, Greenville, SC) connected to a 50 mm cross-head die

(Wayne Machine Die Co., Totowa, NJ) with a 0.635 mm die gap. LDPE (inner)/PP (outer) (50 wt% each) bilayer films were formed at a constant total mass flow rate of 36 gm/min maintained using a gear-pump. For LDPE, zone temperatures: 100°C, 140°C, 160°C and 195°C and for PP, zone temperatures: 120°C, 160°C, 195°C, 220°C were maintained. The die temperature was kept at 240°C. First, the take-up ratios were 3.5 and 10 while the blow-up ratio (BUR) was constant at 1.5. Second, the blow-up ratios were 1.5 and 2.0 while the take-up ratio was constant at 10. Third, the bubble was subjected to uniaxial stretching with a TUR of 17 and a BUR of 0.8. Cooling was carried out using a single-lip air ring with an ambient air at the rate of 20 m/s. Although, the two polymers are not compatible [1] (poor interfacial interaction), no efforts were made to improve interfacial adhesion through a tie layer resin since the objective of this fundamental study was to observe the effects of the coextrusion process on the individual layers. The conditions used for the components in the bilayer blown films were applied to produce LDPE/LDPE and PP/PP blown films. The procedure is as presented in **Appendix A.** The microstructure of single component and bicomponent films were analyzed using online and offline characterization techniques.

Online Raman measurements were carried out using an unpolarized Inphotonics probe coupled to a Renishaw Raman system 200. The probe delivered a 130 mW near-infrared laser beam on the film at 785 nm through a 90 μm diameter excitation cable and the Raman scattered light from the film were collected through a 200 μm diameter collection fiber. The device was mounted on a y-z micrometer stage and was moved axially (z-direction) to obtain spectra at 12 different z-positions along the film line,

starting from the melt upto the nip rolls. A minimum of 3 spectra were obtained from each location. The spectrum at each point was recorded using Renishaw WiRE 1.3 β data acquisition software covering a spectral range of 750-1500 cm^{-1} for an accumulation time of 300s in the static capture mode. Chapter 4 reported the use of real-time Raman spectroscopy to measure the crystallinity development of the components during the coextrusion of PP and LDPE. Though the online experiments were carried on PP (outer)/LDPE (inner) blown film extrusion, the study can also extended to PP (inner)/LDPE (outer) blown films.

The online temperature profile was obtained using an IRCON IR camera (3.43 μm) and velocity and radius profiles were measured using a video-tracer technique. The process-time (t_{proc}) is defined as the time it takes for a mark to travel from the die-exit to the nip-rolls.

Field emission scanning electron microscope (FESEM – Hitachi S 4800) was used to observe the morphology of the films. The LDPE and PP samples were chemically etched in accordance with literature procedure[2]. First the samples were etched for approximately 30 min in a solution containing 0.7 wt % $KMnO_4$ dissolved in 2:1 (v/v) of H_3PO_4 and H_2SO_4. The etched samples were then washed with hydrogen peroxide, distilled water, and acetone. The details are described in **Appendix C**.

Wide-angle X-ray diffraction patterns were measured using the Rigaku 2-D diffractometer in the transmission mode with the films stacked to obtain a constant thickness of approximately 150 μm. The exposure time per image was set to 30 mins. The collected patterns were analyzed for crystalline orientation using POLAR software

after careful background subtraction. The crystalline pole orientation parameter for different crystallographic axes was calculated using Herman's orientation factor: $f = 0.5$ $(3<\cos^2 \varphi > -1)$ defined for uniaxial orientation samples. For polyethylene, reflections from (200) and (020) were used to calculate herman's orientation factors, f_a and f_b, respectively [3]. The (110) of PE could not be used for calculating the orientation parameter in the bilayer films because the (111), (131), and (041) peaks of PP have some overlap with the (110) peak. Therefore, the (020) peak which appears at a higher 2θ was used for calculation of b-axis orientation. A comparison of orientation values obtained with the use of (110) and (020) on a control LDPE film was not significantly different. Using (110), the f_a =0.286, f_b =-0.35, f_c =0.063 and using the (020) arc for b-axis for the same sample gave f_a =0.286, f_b =-0.40, f_c =0.114. Reflections from planes (110) and (040) were used to obtain the crystalline orientation parameters for PP [4]. For the bilayer films, three repetitions of X-ray measurements were carried out. Since, the variability of orientation factors from multiple X-ray measurements was less than 10 %, only a single measurement was made on the single layer films of PP and LDPE.

Birefringence measurements were carried out on the components after peeling the bilayer films. The peeling did not result in stretching of the film since the failure was completely adhesive. In order to arrive at complete picture of orientation in the film, In-plane (Δn_{12}) and out-of-plane ($\Delta n_{13,}$ Δn_{23}) birefringence values were measured using an optical microscope BX-60F5 (Olympus Optical Co. Ltd., Japan) fitted with cross-polarizers and U-TCB Berek compensator (Olympus Optical Co. Ltd., Japan) using the method described by Stein[5] . The details are discussed in **Appendix D**. Rheological

measurements of the polymers were carried out using ARES rheometer for calculation of relaxation time. The procedure and analysis are as shown in **Appendix E**.

5.2.   Results and Discussion

5.2.1. *Real-Time Measurements*

Figure 5.1 shows the radius and velocity profiles for two different processing conditions where the BUR was changed. The profiles shows a general trend as in any blown film process starting with a steep increase in radius and velocity near the die and then leading to a plateau after solidification (frost-line height). The slope of the curves varied depending on the bubble pressure and the take-up speed. The increase in the slope of radius profile was noted with the increase in BUR from 1.5 to 2.0.
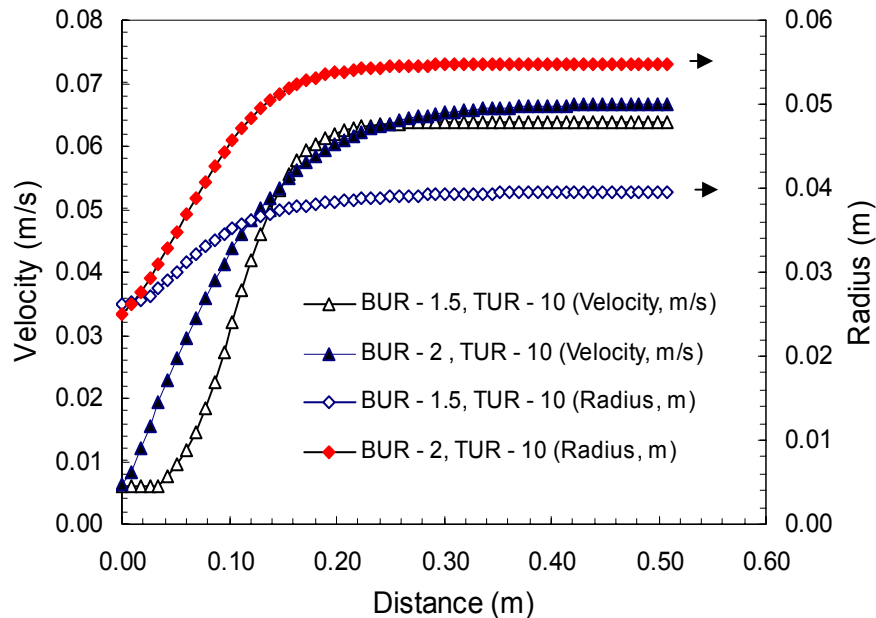
Figure 5.1 Velocity and Radius profiles for two different BURs during bilayer PP/LDPE blown film extrusion

The machine direction (MD) and transverse direction (TD) strain-rates obtained from the velocity and radius profiles are presented in **Figure 5.2**. At the same blow-up ratio of 1.5, an increase in the take-up speed causes an increase in the MD strain rates. However, the TD strain-rates did not change significantly. With increasing bubble pressure (at constant take-up speed), the TD strain rates increased whereas the MD strain rates decreased.
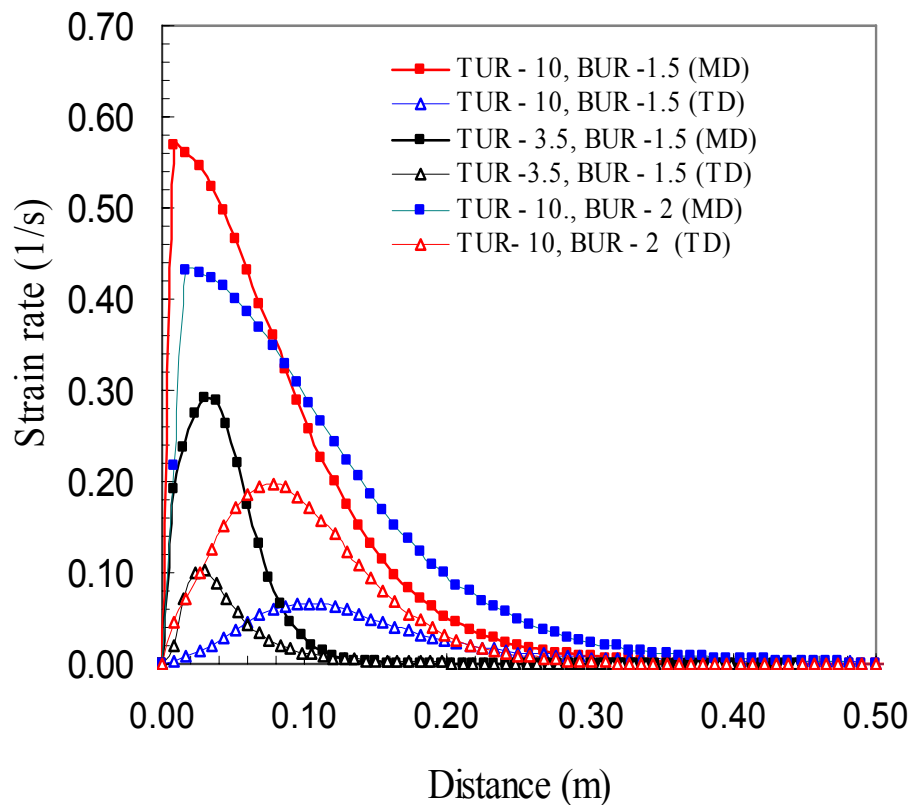
Figure 5.2 Machine direction (MD) and transverse direction (TD) strain rates for two different BURs and TURs during PP/LDPE blown film extrusion showing the effect of BUR and TUR.

Figure 5.3 displays a representative temperature profile along the film line for a TUR of 10 and BUR of 1.5. The temperature trend shows a steep decrease initially and then the first plateau at ≈122 °C, caused by the exothermic heat of crystallization of PP. Another plateau is observed at ≈99 °C, caused by the heat of crystallization of LDPE. When the radius profile is superimposed on the temperature profile (**Figure 5.3**), it becomes evident that the freeze-line height (FZH) in bicomponent blown film is controlled by the layer which solidifies first (PP in this case). This is consistent with observations reported in the literature for EVOH/HDPE blown films [6].
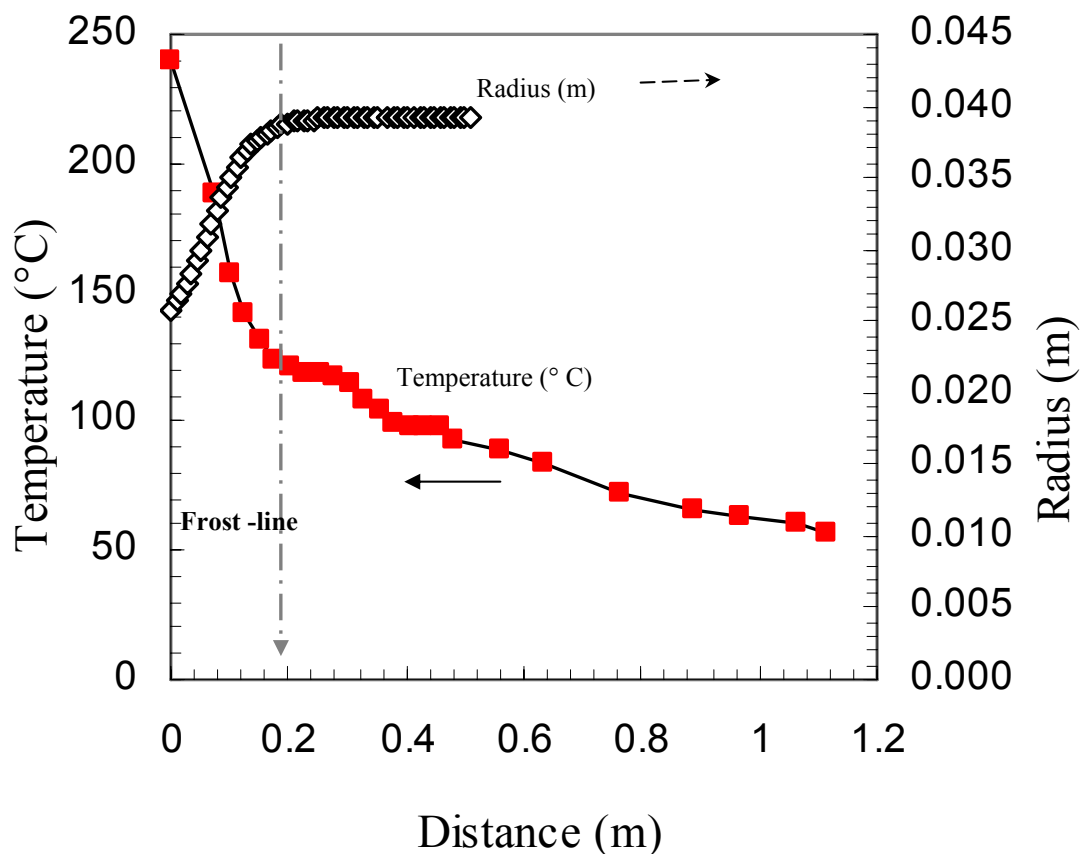
Figure 5.3 Radius profile superimposed with temperature profile for TUR of 10, BUR of 1.5 and moderate cooling (Temperature profile is a trend)

Real-time Raman spectroscopy enabled measurement of crystallinity profiles of the components during the process[7]. **Figure 5.4** displays the real-time crystallinity profiles as function of the process time. PP crystallizes first ($T_c \approx 122°C$) with a steep increase in crystallinity followed by a plateau along the film-line. PE displays a similar trend but at a later time. The temperature profile obtained from the film-line, also displayed in **Figure 5.4,** shows two intermediate plateaus. The first temperature plateau is clearly due to heat of crystallization of PP, whereas the second is due to crystallization of LDPE.
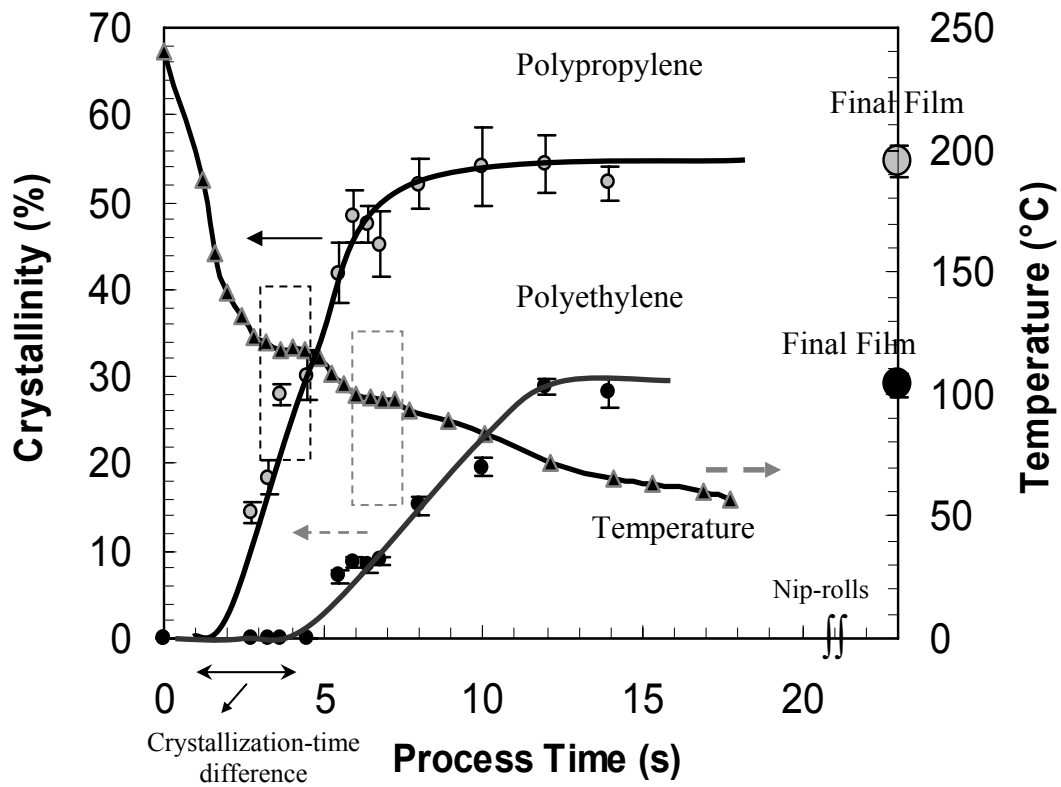
Figure 5.4 Real-time crystallinity profiles of PP and LDPE during PP/LDPE blown film extrusion as function of process time superposed with temperature profile for BUR = 1.5, TUR = 10 and moderate cooling (curves represent trends)

The process-time difference between the onset of crystallization of PP and LDPE components was measured and is presented in **Table 5.1** for various TURs at a constant BUR. The strain-rates obtained in the film-line are also presented in the **Table 5.1**. At a constant BUR, a three-fold increase of TUR resulted in two-fold increase of strain-rates in the machine direction while the TD strain rate remained constant.

Table 5.1. Processing characteristics for different processing conditions for PP/LDPE extrusion

BUR	TUR	Crystallization-time difference* (s)	MD strain rate (s^{-1})	TD strain rate (s^{-1})
1.5	3.5	11	0.29	0.11
1.5	10	3.9	0.57	0.07
0.8	17	3.2	0.58	-0.13

5.2.2. Orientation of the PP and LDPE

Figure 5.5 displays the out-of plane ($\Delta n_{13}, \Delta n_{23}$) and in-plane ($\Delta n_{12}$) birefringence values for single layer and coextruded PP and LDPE for two different TURs and a constant BUR. The out-of-plane birefringences: $\Delta n_{13}, \Delta n_{23}$ are indication of molecular orientation in machine and transverse direction respectively while the in-plane

birefringence (Δn_{12}) is indication of film anisotropy. It can be noted from Δn_{12} values that none of the films showed equibiaxiality ($\Delta n_{12} = 0$) as would be expected for the processing condition studied. Also, PP films showed high birefringence values (high anisotropy) as compared to LDPE films indicating the higher orientation of the molecular chains in the draw direction in PP.

With an increase in the TUR at a constant BUR, both PP and LDPE showed an increase in the machine direction orientation at the expense of that in the transverse direction. However, a comparison of the birefringence of PP from coextruded and single layer films did not show a significant difference. A similar trend was observed for LDPE. Thus, the birefringence values indicated that the overall molecular orientation of the films was not significantly affected during coextrusion of LDPE and PP.
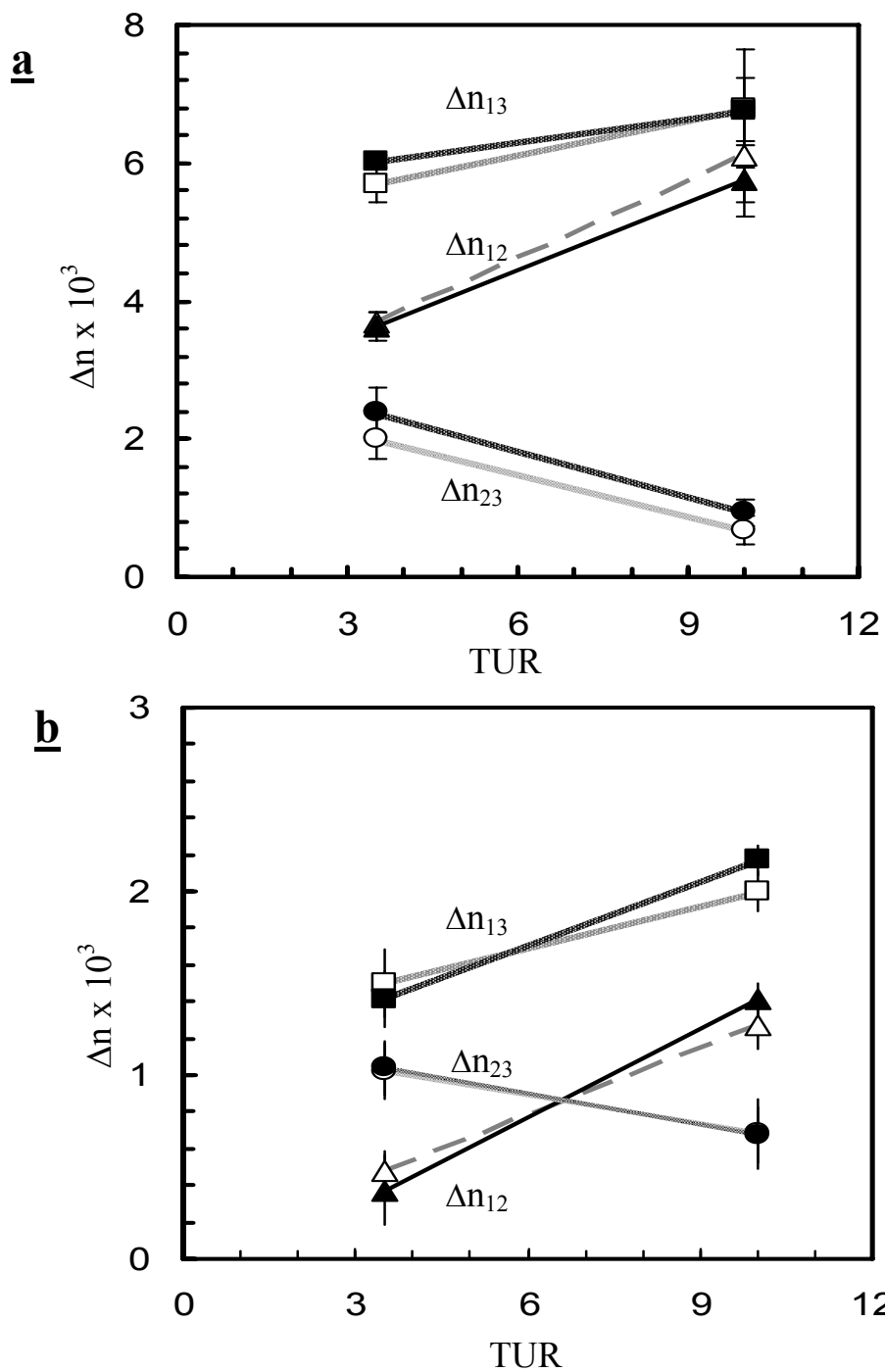
Figure 5.5 Out-of-plane (Δn_{13}, Δn_{23}) and in-plane (Δn_{12}) birefringence values for two different TURs and a BUR=1.5 for single (open symbols) and coextruded (solid symbols) for: (a) PP and (b) LDPE. Line represent trend.

Figures 5.6 a and b present a representative wide-angle X-ray diffractogram of bilayer film of PP/LDPE for two different TURs. The arcs (observed due to preferred crystalline orientation) of interest are (040) and (110) for PP and (020) and (200) for PE.
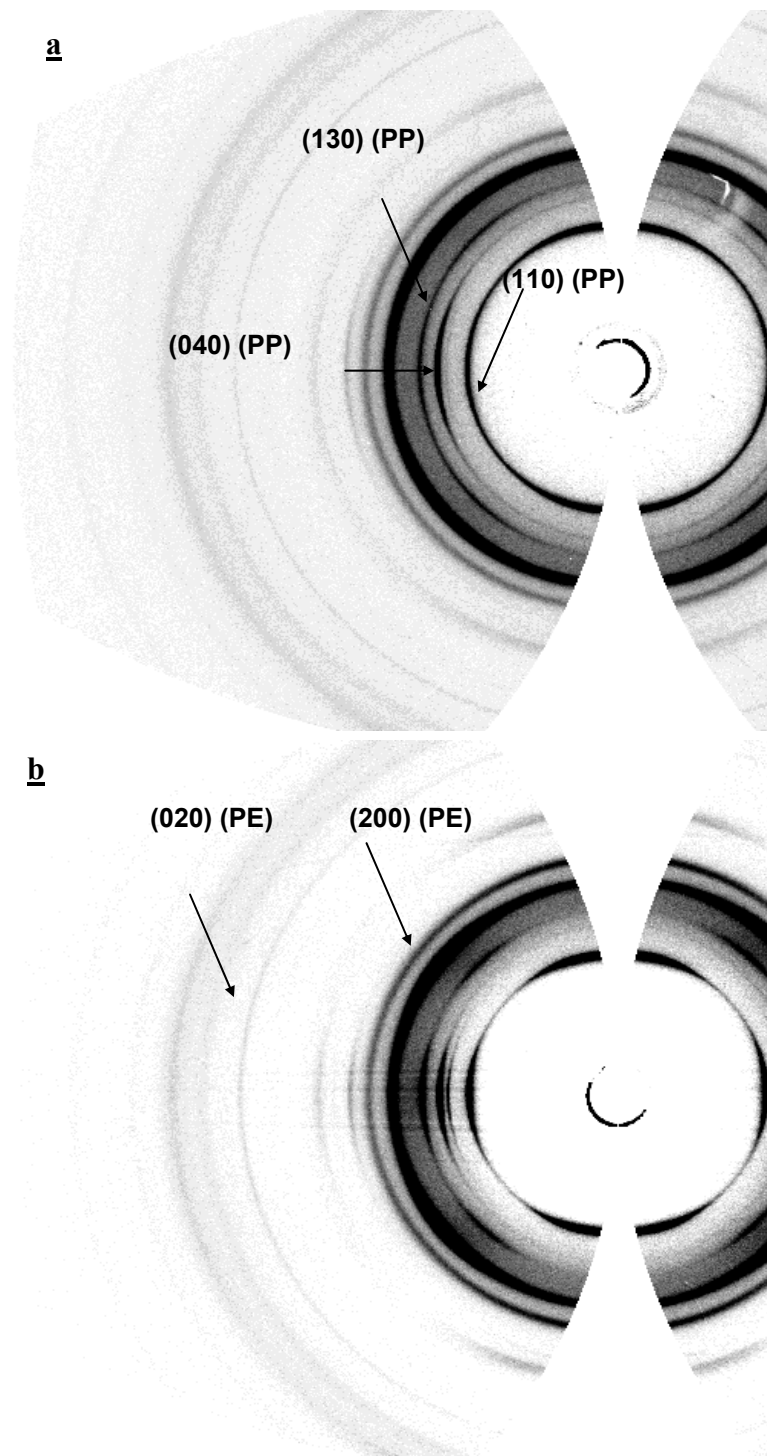
Figure 5.6. WAXD pattern for the PP/LDPE film processed at a BUR of 1.5

for (a) TUR = 3.5, and (b) TUR =10.

Table 5.2 presents a comparison of the Herman's orientation factor for PP and PE obtained by single-layer and coextrusion processes. It is noted that the Herman's orientation factor is zero for a random orientation, 1 for a perfectly machine orientation, and -0.5 for a perfectly transverse orientation. For PP, the c-axis (f_c) tends to orient towards the machine direction with the increase of take-up speed while b-axis (f_b) aligned slightly perpendicular to MD. A comparison of c-axis orientation of coextruded PP and single-layer PP did not show any significant difference.

Table 5.2 Comparison of crystalline orientation factors for single-layer and coextruded PP and LDPE.

TUR	Single PP		Coextruded PP		Single PE		Coextruded PE	
	f_c (c-axis)	f_b (b-axis)	f_c (c-axis)	f_b (b-axis)	f_a (a-axis)	f_b (b-axis)	f_a (a-axis)	f_b (b-axis)
3.5	0.11	-0.22	0.14± 0.02	-0.21± 0.01	0.12	-0.07	0.06± 0.02	-0.03± 0.02
10	0.21	-0.31	0.22 ± 0.02	-0.32± 0.01	0.27	-0.18	0.19± 0.02	-0.11± 0.01

For LDPE, the *a*-axis tends to align in the machine direction with an increase in the take-up speed, while *b*-axis aligns perpendicular to the machine direction following the Keller-Machin I type mechanism at low and intermediate stresses [8]. However, a comparison of *a*-axis orientation factor for LDPE indicates small but significant differences between single and coextruded LDPE. The differences were not very large in this case because the relaxation time of LDPE at the temperature gradient of interest (122°C-90°C) was large compared to that of the crystallization-time difference observed for the present conditions. This effect may be significant for other processing conditions and other polymers such as LLDPE, which relaxes much faster compared to LDPE [9]. Thus, x-ray measurements indicated that for LDPE, the coextruded films show partial relaxation compared to single-layer films processed under similar condition. This was reflected in a small, but definite, change in the *a*-axis orientation factor.

5.2.3. Morphology of LDPE

Figure 5.7 shows the SEM micrographs obtained from single-layer LDPE films in the MD-TD plane for the films subjected to different conditions. At low stress (TUR=3.5), the film showed random lamellar morphology (**Figure 5.7a**). However, at a high stress (TUR=10), the film showed some row-nucleated crystalline arrangement (**Figure 5.7b**).

167
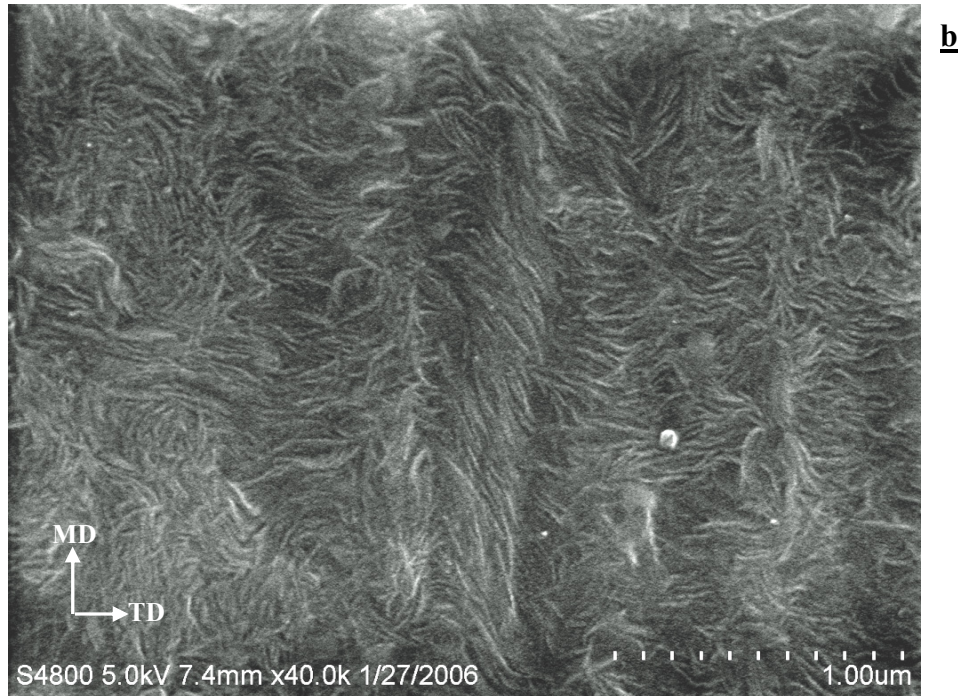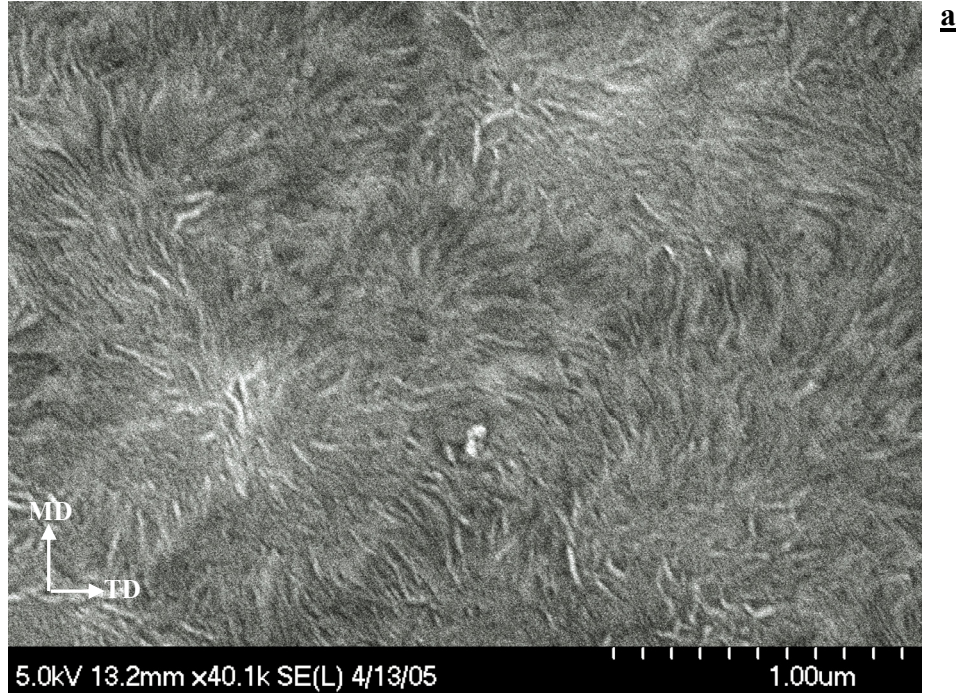
Figure 5.7 Morphology of LDPE single-layer films (a) Low stress (TUR=3.5)
and (b) High stress (TUR=10)

Figure 5.8 presents the morphology of the LDPE layer of coextruded films processed under identical conditions. The effect of coextrusion on the orientation can be noted from the morphology of the films in MD-TD plane. As seen in **Figures 5.8a and b**, for the coextruded films, there is a lack of preferred alignment of lamellae in the plane. **Figure 5.8a** shows the random lamellar arrangement for the film subjected to low stress. However, at high stress, we observe only a partial alignment of lamella with the *b*-axis of the lamellae tending to align perpendicular to MD, as shown in **Figure 5.8b**.
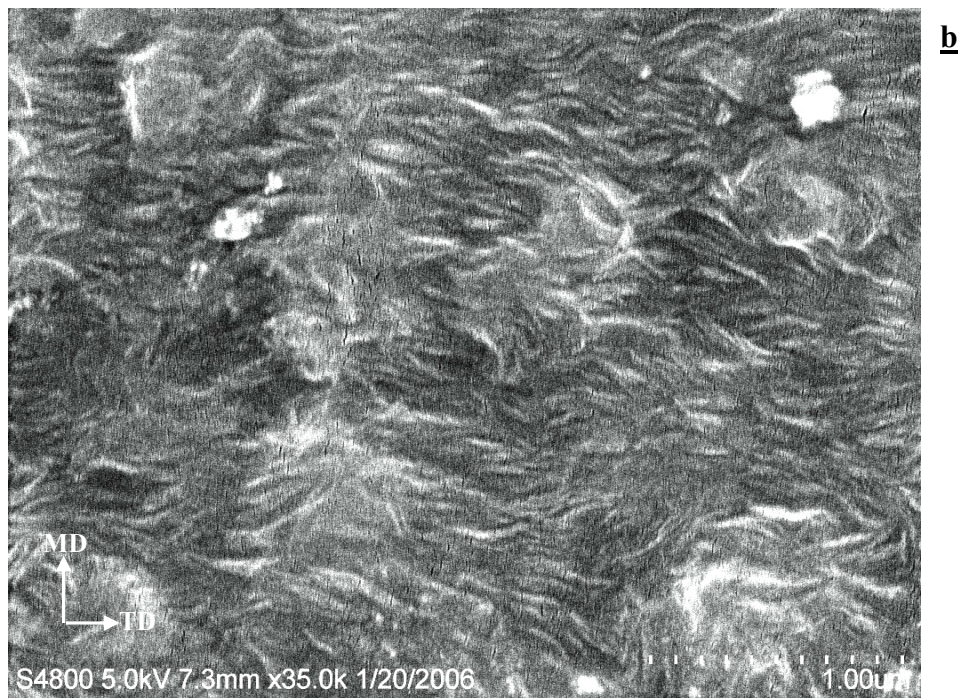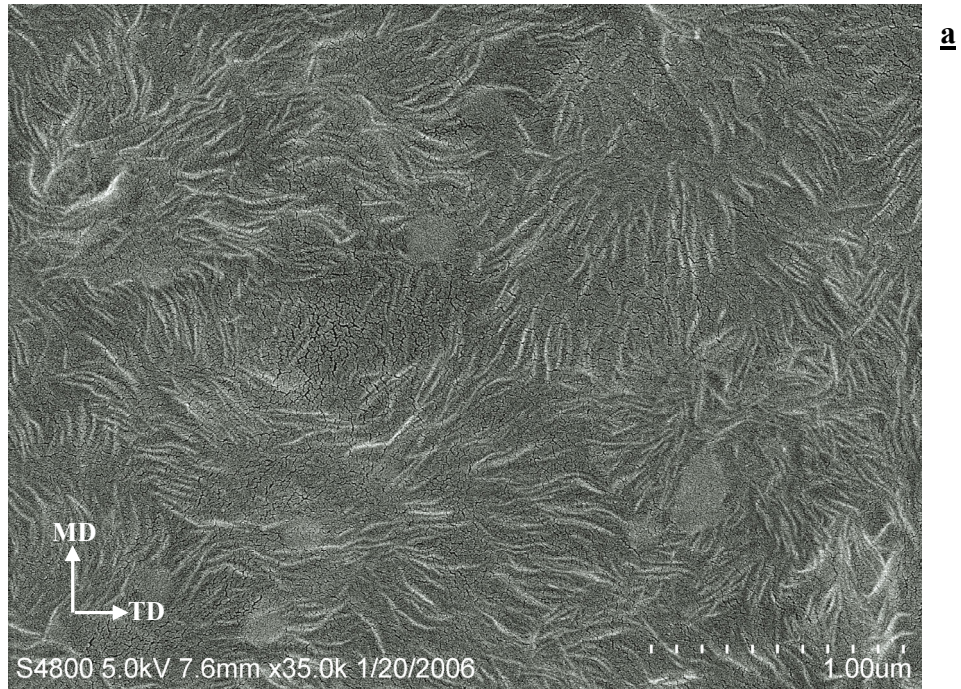
Figure 5.8 Morphology of LDPE coextruded film (a) Low stress (TUR=3.5)
and (b) High stress (TUR=10)

The kinematics of bicomponent blown film process are fairly complex[6]. After the first layer freezes, the stresses are borne by the solidified layer (PP in the present case), while LDPE is still in the molten state. The molecular chains in molten LDPE tend to relax, and the extent depends on the crystallization time-difference between the two components. The longest or terminal relaxation time of LDPE measured by stress-relaxation experiments are 9s, 23s and 43s for temperatures of 150°C, 125°C and 90°C, respectively. The relaxation time of LDPE was also verified by dynamic frequency sweep experiments (Cole-Cole plot)[9] were 0.55 s, 5 s and 11 s for temperatures 200 °C, 150 °C and 125 °C respectively.

Thus, the difference in microstructure can be a consequence of the low stress on molten LDPE layer after the freeze-line height (FLH), where the PP layer starts to crystallize (122 °C). Such low stress in LDPE layer could possibly cause the high molecular weight chains, which serve as fibrillar nuclei for row-nucleated structure, to relax during the process before the onset of LDPE crystallization. It is known that the maximum stress occurs near the frost-line and the extent of stress-induced crystallization is determined by the number of long chains that get extended during the onset of crystallization.

The difference in the morphology of LDPE observed for the single (**Figure 5.7b**) and coextruded (**Figure 5.8b**) films can be attributed to the crystallization-time difference between the onset of crystallization of PP and LDPE and the relaxation of LDPE. The crystallization-time difference at high stress was ~ 3.2 s. Although smaller than the relaxation times (23-43s) in the temperature range of interest (125°C-99°C), partial

relaxation of chains can still occur for long-chain fibrils, which will reduce the extent of row-nucleation. These results are consistent with observations reported in the literature[6] that an individual polymer can behave differently in a multi-component film versus that as a single-layer film. The differences in the morphology and orientation of the LDPE indicate that the simple rule of additivity cannot be used to predict properties in PP/LDPE blown film.

The effect of coextrusion on the microstructure of polypropylene (PP) and low-density polyethylene (LDPE) bilayer films (PP/LDPE) was investigated by the use of Raman spectroscopy. The onset crystallization-time difference for PP *vs* LDPE components is an important parameter that controls the orientation and morphology of the coextruded films. Although, the overall molecular orientation of PP and LDPE multiple layers was not affected, single-layer LDPE films displayed some row-nucleation of crystals, but not the LDPE layer in coextruded films. Also, there was a slight decrease of crystalline *a*-axis orientation for coextruded LDPE layer relative to that for single-layer LDPE films.

5.3. Conclusions

It was found that the crystallization-time difference for the onset of crystallization of PP and LDPE plays an important role in determining the orientation and morphology of the components during PP/LDPE bilayer blown film extrusion. Raman spectroscopy enabled measurement of this crystallization-time difference during PP/LDPE bilayer film

extrusion. WAXD and SEM results indicated that the LDPE layer is affected during PP/LDPE coextrusion and does not form significant row-structures even at high stresses relative to that observed for single-layer LDPE films. These changes can be attributed to the existence of crystallization-time difference between the components during coextrusion. Therefore, the rheological behavior and crystallization of the various components can have a profound effect on the microstructure and properties of the multilayer films relative to that observed for single layer films.

5.4. References

1.   Kimberly A, Jeffrey S, Patrick B, and Frank S. Science 2000;288.

2.   Olley RH and Bassett DC. Polymer 1982;23(12):1707-1710.

3.   Dees JR and Spruiell JE. Journal of Applied Polymer Science 1974;18(4):1053-1078.

4.   Nadella HP, Henson HM, Spruiell JE, and White JL. Journal of Applied Polymer Science 1977;21(11):3003-3022.

5.   Stein RS. Journal of Polymer Science 1957;24.

6.   Morris BA. Journal of Plastic Film & Sheeting 1999;15(1):25-36.

7.   Gururajan G and Ogale AA. Plastics Rubber and Composites 2005;34(5-6):271-275.

8.   Keller A and Kolnaar JWH. Orientational Phenomena in Polymers: Springer Berlin / Heidelberg, 1993.

9.   Zhang XM, Elkoun S, Ajji A, and Huneault MA. Polymer 2004;45(1):217-229.

CHAPTER SIX

CONCLUSIONS AND RECOMMENDATIONS

This chapter summarizes major conclusions drawn from this dissertation. First, conclusions are drawn based on research results presented in Chapters 2, 3, 4 and 5, and then recommendations are provided for future studies.

6.1. Conclusions

In Chapter 2, the use of real-time polarized Raman spectroscopy to measure molecular orientation development during blown film extrusion of a low-density polyethylene (LDPE) and polypropylene (PP) was established. Polarized and non-polarized Raman spectra along with temperature profiles were obtained at different locations along the blown film line, starting from the molten state near the die and extending up to the solidified state near nip-rolls. The experimental difficulties involved in the measurements were overcome by assuming invariant Raman tensor components during phase transformation and conducting measurements on the bubble subjected to uniaxial extension. The second and fourth coefficients of the orientation distribution function (P_2 and P_4, respectively) were quantitatively determined from the polarized scattering intensities of the band at 1130 cm^{-1}. The orientation parameters, P_2 and P_4 increased with the crystalline development. The difference in P_2 values measured from

Raman measurements and WAXD techniques was noted. The increase in orientation of the chains even after even after the bubble shape is locked into place indicated that reorganization of the chain orientation continues far above the frost line height. The potential of real-time Raman spectroscopy as a rapid microstructure monitoring tool for better process control during blown film extrusion was established.

Although Raman spectroscopy is a convenient technique, it is not a primary measurement technique to obtain crystallinity and orientation. Therefore, for the first time, real-time wide-angle X-ray diffraction (WAXD) was attempted during blown film extrusion. In Chapter 3, the feasibility of using wide-angle X-ray diffraction for real-time crystallinity measurements during the blown film extrusion of low-density polyethylene was established. From the evolution of (110) and (200) peaks, it was evident that the crystallization process starts near the frost-line height (FLH), shows a steep growth immediately past the FLH, and then plateaus at higher axial distances near the nip-rolls. From simultaneous Raman spectroscopy and WAXD measurements, it was concluded that the real-time crystallinity profiles obtained from the two independent techniques were consistent.

Multi-layer blown films are of significant industrial importance to make packaging films of superior properties. Therefore, real-time Raman measurements were extended from single-layer blown film extrusion to multi-layer blown film extrusion. In Chapter 4, real-time Raman spectroscopic measurement of crystallinity of the individual components, LDPE and *i*-PP, of a bilayer film (LDPE/PP) during blown-film extrusion was reported. The possibilities and limitations of real-time Raman spectroscopy during

LDPE/PP coextrusion are discussed. Raman spectroscopy was shown to be a promising technique for real-time monitoring of crystalline growth of individual components in bicomponent LDPE/PP blown films. The technique using unpolarized probes was found to be valid for PE/PP bilayer films in which the components show good optical clarity and have layer thicknesses of approximately 50-70 μm. The offline conventional and confocal Raman measurements indicated that the 809-841 cm^{-1} crystalline bands of PP are unaffected by the presence of PE and the use of 1296-1305 cm^{-1} does not significantly affect the calculation of crystallinity of PE in PP/PE films. The crystallinity profile was consistent with the observation of a double plateau in PE/PP blown films. The crystalline growth of PP and PE components increased as the take-up speed was increased.

Finally, in Chapter 5, the crystallinity development in individual components measured using Raman spectroscopy was utilized to understand the complex multilayer blown film extrusion process. The effect of the blown film coextrusion process on the molecular orientation and crystalline morphology of the components in LDPE/PP bilayer blown films was investigated. It was found that the crystallization-time difference for the onset of crystallization of PP and LDPE plays an important role in determining the orientation and morphology of the components during PP/LDPE bilayer blown film extrusion. Raman spectroscopy enabled measurement of this crystallization-time difference during PP/LDPE bilayer film extrusion. WAXD and SEM results indicated that the LDPE layer is affected during PP/LDPE coextrusion and does not form significant row-structures even at high stresses relative to that observed for single-layer LDPE films. These changes can be attributed to the existence of crystallization-time

difference between the components during coextrusion. It was concluded that the rheological behavior and crystallization of the various components can have a profound effect on the microstructure and properties of the multilayer films relative to that observed for single layer films.

Thus, the dissertation investigated real-time Raman spectroscopy and real-time wide-angle X-ray diffraction techniques for crystallinity and orientation measurements during blown film extrusion of polyolefins.

6.2. Recommendations for Future Work

In Chapter 2, the orientation measurements were obtained using polarized Raman spectroscopy. The Raman tensor ratios were assumed to be invariant, i.e., they do not change with crystallinity and orientation. Therefore, the tensor elements obtained on the processed film were used to obtain orientation parameters at other axial distances in this study. Although this simplified approach captured the important structural transformation occurring during the film blowing, a complete set of 12 spectra can be recorded in different polarization geometries to accurately estimate the tensor ratios at each position in the film line. The experimental difficulties for conducting right-angle scattering measurements, which occur due to motion of the bubble, can be addressed using (i) a state-of-the-art motion control system, and (ii) Raman probes attached with video camera arrangements that can be custom-built for the application.

In Chapter 3, real-time wide-angle X-ray diffraction measurements were successfully utilized to measure crystallinity during polyethylene blown film extrusion. This primary measurement technique validated crystallinity data from Raman spectroscopy. The diameter of the bubble during real-time X-ray diffraction measurements was limited to the gap in the platform that holds the X-ray gun and the image-plate. Consequently, only small diameter bubble could be investigated real-time. It was reported that the offline measurements can be conducted on bigger bubble diameters. However, to conduct such measurements on a high BUR bubble, the experimental setup needs to be changed. The orientation and crystallinity measurements can then be extended for biaxial orientation.

In Chapter 4, the real-time crystallinity evolution of the individual components, PP and LDPE, was reported. The unique characteristic crystalline peaks of PP and LDPE enabled such measurements without influence of one layer over the other. The significance of such measurements was reported in Chapter 5. The measurements can be extended to coextrusion of other polyolefins such as HDPE and LLDPE to understand the effect of coextruding different polymers. The technique can also be extended for three component blown films. The utilization of real-time Raman spectroscopy for polymers other than polyolefins would be great commercial because most multilayer blown film coextrusion involves using a tie-layer resin. It will be interesting to explore the effect of tie-layer resin on the microstructural changes during the multilayer film process.

One of the important objectives of conducting real-time measurements was to help in the development of process models. The experimental verification of single-layer

179

blown film extrusion process model has been carried out at the Center for Advanced Engineering Fibers and Films (CAEFF). In the future, the real-time data on multilayer blown film extrusion can be used to develop and validate a process-model for the complex multilayer blown film extrusion.

APPENDICES

Appendix A

Multilayer Blown Film Extrusion

The following information is the procedure for extrusion of single and bilayer films using the equipment in the Laboratory located in Rhodes, Room 302.

   I. Initial Setup
      a. Begin by turning on the power supply of the extruder.
         i. This can be done by turning on the circuit breakers.
      b. Turn on the water hoses to cool the extruder hoppers.
      c. From there, turn on the heaters in each of the extruder zones, pumps and die.
         i. There will be different temperature (^{o}C) requirements at various zones, depending on the material processed; these are approximate temperatures. See **Table** A.1 for details.
        ii. If extruding a mixture, set the process condition to those of the polymer with the highest required values.

Table A.1: Temperature at various zones of the extruder.

Material	Zone 1	Zone 2	Zone 3	Zone 4	Zone 5	Zone 6	Pump	Die
i-PP	161	195	240	240	240	240	240	240
LDPE	145	166	210	240	240	--	240	240

      d. Turn on the air blower, and keep the air influx at the ring
      e. Allow the heaters at the various zones to come to temperature.
  II. Procedure
      1. The polymer pellets are filled into the extruder hoppers.
      2. Turn on the pumps and set the flow rate to a value of 3. **NOTE: Anything above this may damage the pumps; Ensure that the amperage meter for the pumps is below 3 amps at all times.**
      3. Gradually bring up the pump speed to a higher flow rate.
         a. Each polymer will require a different flow rate due to their viscous nature. See **Table** A.2 for details.

Table A.2 : Material with Corresponding Metering Pump Reading

Material	Pump Values
Isotactic Polypropylene	44.4
Low Density Polyethylene	42.5

4. Set the automated controller to ensure that the extruder provides sufficient material to the pump to maintain a constant flow rate.
   a. If there is a substantial decrease in pump pressure, this may be caused by the polymer melting in the hopper.
   b. To overcome this problem, use a long brass blunt ended object to force the melted polymer into the extruder.
   c. If this continues to occur, turn down the temperature in the zones closest to the hopper, and increase the water flow rate.
5. As the pumps push the melted polymer through the die, clean off the die
6. Turn on the compressed air valve, and allow a stream of air to enter using the knob located below the die.
   a. It will be important to control and measure the amount of air entering, since this leads to bubble formation leading to the blow-up ratio (BUR), so record this values.
7. Take the polymer exiting the extruding die and pull up which should force it into the shape of a film.
8. Continue to pull on the film until it is of sufficient length to place in the nip roller.
   a. Before placing the film into the nip rollers, thread the film between two stationary bars that will maintain the film in place.
9. Turn on the nip roller.
   a. Set to a rotational speed of about 30 rpm. This will be used to calculate the take-up ratio (TUR).
10. Allow the film to be pulled up using the rollers.
    a. If notable creases are contained within the films, clean the inside of the die using a sharp thin brass tool.
    b. Be careful that the film does not stick to the rollers; if this occurs, stop the roller and cut the film. Remove the film caught in the roller, and repeat the process beginning with Step 7, but this time, pull in film as it leave the rollers to avoid the and sticking.
11. Collect the film at the tail end of the rollers.
12. Place in plastic container bags, and store for testing.

Appendix B

Real-Time Raman Spectroscopy

I.   Initial Set-up

1. Raman system:
    1. The real-time Raman system is custom-built Renishaw Raman system 100 with 200 mW near-infrared diode laser source.
    2. The spectrometer can be coupled to non-polarized Inphotonics Ramanprobe™ (Norwood, MA), polarized Renishaw® Raman probes (XY and XX)

II.   Operation and Data-processing

1. Switch ON, the spectrometer, laser source and the computer.
2. Connect the Raman probes to the Raman spectrometer.
3. Wait for at least 10 mins till the full-power of laser source is reached.
4. Check the laser power and wavelength using a laser power-meter
5. Click on the Renishaw Wire icon.
6. Do the x-calibration test by going to system check from collect menu.
7. Set appropriate tracks for the probes. Check 1 for external probe and check 3 for Renishaw probe.
8. Collect a spectrum of cyclohexane for calibration. Check for the peak at 800 cm^{-1}. If it doesn't center at 800 cm^{-1}, then go to experimental setup in collect menu and do offset correction for the difference ($\pm$). Collect the spectrum again and check the peak.
9. Set the experimental condition and stabilize the bubble at appropriate BUR and TUR.
10. Place the Raman probe on the XY micrometer stage that was on Z-platform. Turn OFF the light in the room. Focus the laser beam on the bubble. If the laser is focused is well, a bright sparkle on the sample can be noticed.
11. Set the accumulation time and click "collect "in the experimental set-up menu.
12. Click on "save" icon to store the spectrum in desired location in computer.
13. Collect at least three spectrum at each axial location.
14. Open the spectrum for analysis
15. First go to arithmetic and then smooth the spectrum using binomial function.
16. Second, fix the baseline for the spectrum. In the arithmetic menu, go to the baseline and check multipoint.

17. Save the processed spectrum with a new name.
18. Open the file and zoom on the peak and do curve fitting by clicking on arithmetic menu.
19. Right-click on the mouse to see the mix Gaussian-Lorentzian function.
20. After iteration is finished, note the center, area, height and % Lorentzian in the fit.

III.   Shut down

1. Exit the Renishaw WiRE program.
2. Switch the computer Off.
3. Turn off the spectrometer and the laser source.

IV.   Precautions during operation

1. Do not bend or step-up on the optic-fiber cables of the Raman probes.
2. Do not look at the laser with direct eye.

Appendix C

Scanning Electron Microscopy

I. Initial set-up:

1. Apparatus: The Hitachi S-4800 Field Emission Scanning Electron Microscope (CFE-SEM) is located at Electron Microscopy facility at Advanced Materials Research Laboratory, Clemson, SC
2. Collect the following items before experiment:

   A. Hot-plate and a stirrer.
   B. Glass beakers -500 ml
   C. Permanent marker
   D. Potassium permanganate ($KMnO_4$), Acetone, Orthophosphoric acid (H_3PO_4, 100 ml), Sulphuric acid (H_2SO_4, 100 ml), Hydrogen peroxide (H_2O_2, 100 ml), distilled water (300 ml), Acetone (200 ml)
   E. Liquid nitrogen in flask.
   F. Dry-ice.

II. Permanganic Etching

1. Blown film samples are marked with machine and transverse directions and cryogenically fractured.
2. First, dissolve 0.7 wt % $KMnO_4$ in 2:1 (vol. ratio) of H_2SO_4 and H_3PO_4 and stir the solution at room temperature for approximately 1 hr. (**Extreme Caution:** Do not pour H_2SO_4 and H_3PO_4 mixture over $KMnO_4$)
3. The cut film samples are treated with the solution for 30-40 mins.
4. The samples are taken out of the beaker.
5. The samples are washed with a mixture of 2 volume of H_2SO_4 and 7 volumes of water kept in a dry-ice bath for 10 minutes.
6. The solution is decanted and washed with H_2O_2, then using distilled water and finally with acetone. They are dried for 12 hrs.
7. The etched film samples are ready for microscopy.

III. Scanning electron microscopy

1. First, the films are mounted on the sample-holder in the appropriate direction for SEM and coated with platinum using Hummer® 6.2 Sputtering system in the Electron Microscopy lab. Follow the step-by-step instructions provided beside the machine.
2. The sample-holder is tightened to the arm and the chamber is closed. Wait for the chamber to reach vacuum (the light flash stops).

3. The arm can now be taken inside the instrument chamber by opening the chamber door. Then it is placed on the instrument mount.
4. The sample movement can be controlled using the joy-stick provided in the system.
5. Start with low magnification to locate the appropriate directions and collect images at the desired magnification.

IV.   Precautions

1. Do not pour H_2SO_4 and H_3PO_4 mixture over $KMnO_4$.
2. Wait for the chamber to reach the required vacuum. Do not move the arm inside instrument before vacuum is reached.
3. Do not sputter coat the films for more than 90 secs minutes. The coating could mask the morphological features of the sample.

Appendix D

Birefringence (Berek-Compensator Method)

1. Theory

Deformation during the film blowing process produces biaxial orientation. For biaxial films, the three principal refractive indices (α, β, γ) are different in each direction (1,2 and 3) because of the anisotropy caused by the orientation of the polymer chains in the film. Birefringence is a measure of optical retardation of light passing through different planes of the film. This is dependent on the difference in the refractive indices in the plane of the film and its thickness. In order to arrive at complete picture of molecular orientation in the film, In-plane (Δn_{12}) and out-of-plane (Δn_{13}, Δn_{23}) birefringence values are measured using an optical microscope BX-60F5 (Olympus Optical Co. Ltd., Japan) fitted with cross-polarizers and U-TCB Berek compensator (Olympus Optical Co. Ltd., Japan) using the method described by Stein[1].
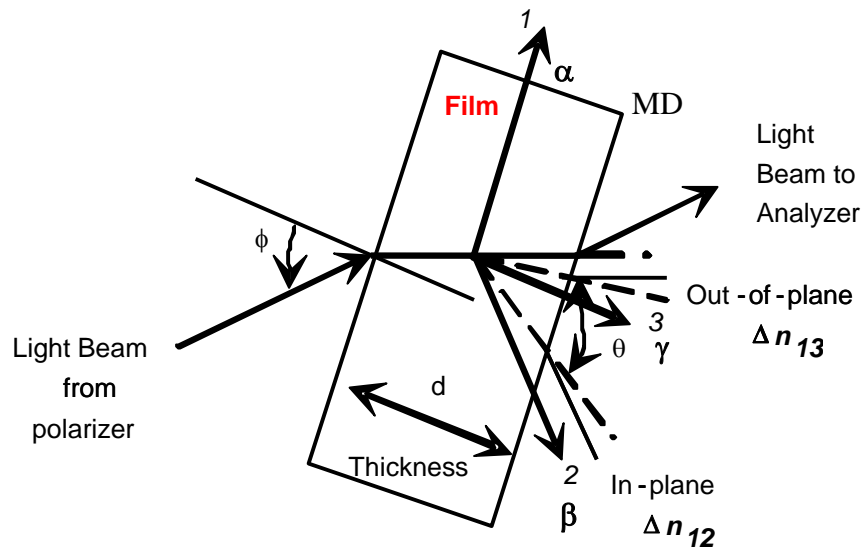

Figure D.1. Incident light beam with respect to principal axes and optic axes of film [1]

Figure D.1 presents the birefringence through the film. The out-of-plane birefringences: Δn_{13}, Δn_{23} are indication of molecular orientation in machine and transverse direction respectively while the in-plane birefringence (Δn_{12}) is indication of film anisotropy. Inplane ($\Delta n_{12} = \beta - \alpha$) birefringence can be obtained directly by measuring retardation through the film.

For the case of out-of-plane birefringences, R.S.Stein derived the following equation that relates birefringence with the retardation of the film with out-of-plane birefringence:

$$\Delta n_{13} = \gamma - \alpha = \frac{\lambda_0}{d_0} \left[\frac{R_0 - R_\phi (1 - \frac{\sin^2 \phi}{n^2})^{1/2}}{\sin^2 \phi / n^2} \right]$$

Also, $\Delta n_{23} = \Delta n_{13} - \Delta n_{12}$

where λ_0 is the wavelength of the light used in vacuum, d_0 is the thickness of the film, n is the average index of refraction for the film obtained from a refractometer or literature. R_0 is the retardation of the film for normal incidence, expressed in units of number of waves, and R_ϕ is the retardation of the film tilted through the angle Φ. The retardation is measured using a UTB compensator. The film should be placed on a tilting stage to rotate the sample to incline with respect to the incident beam.

2. Procedure

2.1. The arrangement of the compensator is as shown in Figure D.2a. The crystal inside the compensator is mounted on a frame in the way shown in Figure D.2b. At 0° of the compensator, the optic axis of the crystal is aligned with the light coming from the polarizer.
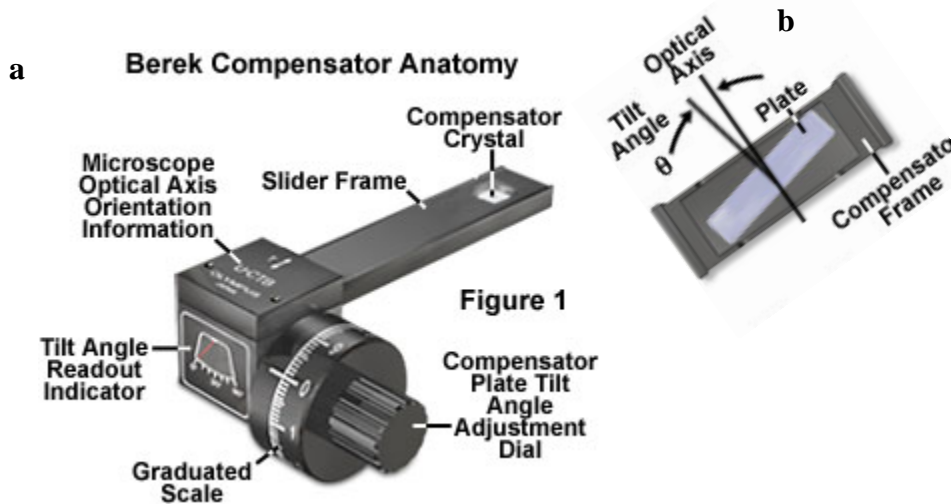

Figure D.2 a. Berek Compensator b. Crystal inside compensator (Reproduced with permission from Prof. Michael W. Davidson, The Florida State University)

2.2. Mount the compensator at 45° position relative to the polarizer and analyzer in the mounting tube of the microscope.

2.3. The adjustment in the compensator rotates the birefringent plate with respect to the optic axis of the microscope. As the plate is tilted, the retardation value is increased

2.4. The film sample is mounted on the glass slide and placed on the stage and rotated till there is extinction (dark)

2.5. Next, the microscope stage is rotated 45°and fixed at the position by turning the stage-screw. This position is the brightest spot.

2.6. Adjust the compensator knob, so that the black fringe intersect the center of view. If it does not intersect, the stage should be rotated by 90°
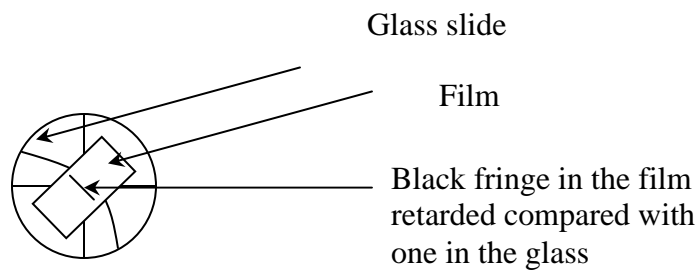
Glass slide

Film

Black fringe in the film retarded compared with one in the glass

Figure D.3 Black fringe on the film

2.7. An interference green filter is used to get clear sight of the fringes and to improve the accuracy of measurements.

2.8. First rotate clockwise and note the angle θ_1 from the compensator scale and then rotate anticlockwise to note θ2 of the black fringe positioned at the center of the field of view as shown in Figure D.3. Obtain 3 or 4 different repetition and calculate the average of $\theta = (\theta_1 - \theta_2)/2$

2.9. The e-line reference table is used to get the retardation value based on the tilt angle differences.

3. Precaution

The compensator drum knob is set to a position of 30-degrees and inserted into the microscope intermediate tube.

4. Reference:

(1)   Stein, R. S. *Journal of Polymer Science* **1957**, *24*.

Appendix E

Rheometry

Rheological experiments were performed to measure the relaxation-time of low-density polyethylene. TA-Rheometrics "Advanced Rheometric Expansion System" (ARES) was used for this purpose.

E.1 Stress-Relaxation Experiment

The stress-relaxation experiments were performed using parallel-plate geometry. A constant shear rate of 0.1 s^{-1} was applied for a particular time period till the stress reaches a constant value and then the shearing was stopped to note the decay of the stress over time. The stress decreases monotonically over time.

The following procedure should be used to conduct stress-relaxation experiment in ARES rheometer.

1. Make sure the air-pressure to the instrument is at the recommended level, if not adjust the valve to get the desired pressure.
2. Then switch ON the rheometer using a switch located on the backside.
3. Open the TA Orchestrator® software on the computer.
4. First the motor mode was changed to "steady" by clicking on the Control-Motor mode in the software and then parallel plates are brought closer after loading the sample.
5. Wait till the normal force value reach close to zero and then click on control-edit/start test. In the Edit/Start Instrument, click on the predefined geometry as parallel plate. In the edit geometry section, enter the dimensions of the fixture and the gap.
6. In the "Test Setup" select "predefined test setups and select measurement type as "Transient". Then the setup as "Step-rate test" Click the "Edit Test tab.
7. In the "Step-Rate Test" window options such as temperature, sampling mode, shear rates, shearing time and the direction of measurement can be entered. Enter desired value and click OK.
8. Start the test by clicking "Begin Test" tab in the Edit/Start Instrument Test menu.
9. Once the test was completed, the file is saved automatically and can be used for analysis.
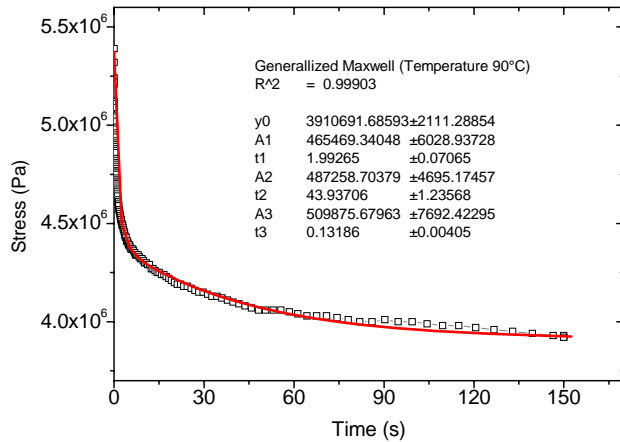10. Carefully remove the fixtures and clean with acetone and brass-tools.

Figure E.1 Maxwell model using three parallel Maxwell dashpot-spring

elements

Inorder to estimate the relaxation time, three Maxwell elements were used to fit to the data shown in Figure E.1 and the longest relaxation time among the three elements was reported.

E.2 Dynamic Frequency Sweep Experiment

Dynamic frequency sweep experiments were also performed to investigate the relaxation behavior of LDPE. The experiments were peformed using ARES rheometer with a cone and plate geometry. The frequency range was 0.05-100 s^{-1}. To determine the linear viscoelastic region of LDPE, strain-sweep experiments were performed initially.

1. First the motor mode was changed to "dynamic" by clicking on the Control-Motor mode in the software and then cone-plate were brought closer after loading the sample.

2. Choose the measurement type as "Dynamic and test setup as dynamic strain sweep test.

3. Set the frequency, temperature, the sweep mode, initial and final strain and the number of points per decade values and click OK.

4. Start the test by clicking "Begin Test" tab in the Edit/Start Instrument Test menu.

After linear viscoelastic region is determined, particular strain value within linear viscoelastic region was selected for dynamic frequency sweep experiments. Then following procedure was used to conduct the experiment.

1. Choose the measurement type as "Dynamic and test setup as dynamic strain sweep

test.

2. Enter the % strain, temperature, sweep-mode, initial frequency, final frequency,

and the number of points per decade of interest and then click OK.

3. Start the test by clicking "Begin Test" tab in the Edit/Start Instrument Test menu.

4. Once the test is completed, the file is saved automatically and can be used for

analysis.

5. Carefully remove the fixtures and clean with acetone and brass-tools.

Data-Analysis
The complex viscosity $\eta^*(\omega)$ is defined by
$\eta^*(\omega)=G^*(\omega)/i(\omega)=\eta'(\omega)-i\eta''(\omega)$

where $\eta'(\omega)=G''(\omega)/\omega$ and $\eta''(\omega)=G'(\omega)/\omega$.

The term, $G'(\omega)$, is in phase with the strain and is called the storage modulus. $G''(\omega)$ is out of phase with the strain, and is called the loss modulus. The ratio of the storage and loss modulus is the loss tangent or tanδ. During frequency sweep experiments, the rheometer measures the torque and the phase-angle difference, δ, which were used to obtain $G'(\omega)$ and $G''(\omega)$

Inorder to calculate relaxation time, Cole-Cole plot which is a log plot of $\eta'(\omega)$ vs. η'' (ω) were drawn. The Cole-Cole plot is shown in Figure E.2 and can be viewed as a distribution of relaxation time from the dynamic sweep experiment. The characteristic relaxation time which is $\tau=1/\omega_c$, where ω_c is the frequency corresponding to η'' as explained in the literature [1,2].
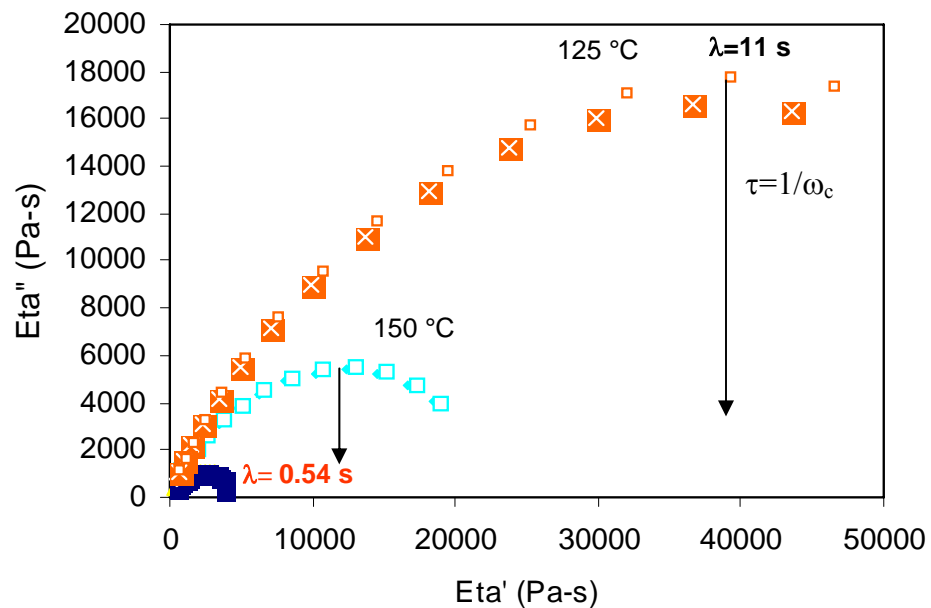
Figure E.2 Cole-Cole plot representation for temperatures: 125°C, 150°C

and 200°C for LDPE

References:

(1)   Zhang, X. M.; Elkoun, S.; Ajji, A.; Huneault, M. A. *Polymer* **2004**, *45*, 217-229.

(2)   Labaig, *Polymer* **1973**, *14*.